EPITAXIAL GRAPHENE AND NITRIDES: NEW PROCESSES FOR IMPROVED ELECTRONICS AND OPTOELECTRONICS

A Dissertation
Presented to
The Academic Faculty

By

Renaud Puybaret

In Partial Fulfillment
of the Requirements for the Degree
Doctor of Philosophy
in
Electrical and Computer Engineering

School of Electrical and Computer Engineering
Georgia Institute of Technology
August 2015

Copyright © 2015 by Renaud Puybaret

EPITAXIAL GRAPHENE AND NITRIDES: NEW PROCESSES FOR IMPROVED ELECTRONICS AND OPTOELECTRONICS

Approved by:

Dr. Abdallah Ougazzaden, Advisor
Professor, School of ECE
Georgia Institute of Technology

Dr. Paul L Voss, Advisor, Committee Chair
Associate Professor, School of ECE
Georgia Institute of Technology

Dr. Azad Naeemi
Associate Professor, School of ECE
Georgia Institute of Technology

Dr. Claire Berger
Directeur de Recherches CNRS
Research Scientist, School of Physics
Georgia Institute of Technology

Dr. Walt A de Heer
Regents' Professor, School of Physics
Georgia Institute of Technology

Dr. Jean-Paul Salvestrini
Professeur des Universités
Université de Lorraine & CentraleSupélec
Adjunct Professor, Georgia Tech ECE

Date Approved: May the 29^{th}, 2015

à Maman et Papa, Florent, Mamiryse et Papi Riton, Tonton Pierre, Carla et Martin.

à Mamone, j'aurais aimé que tu restes un peu plus longtemps, que tu vois l'homme que je suis devenu.

à Papi Jean, j'ai toujours imaginé que tu serais présent aujourd'hui, ainsi d'une certaine façon tu l'es.

ACKNOWLEDGMENTS

To Pascal Windels, thank you for everything. I probably would never have become a scientist without you *(see Vita)*. Thank you for all your support during my long studies, for your mentoring, for your friendship.

To my elementary school teacher Jean-François Elissalde, when I was then 8 to 10 years old, at Ecole Jules Ferry (Biarritz, France), well thank you for starting all of this. You are simply the best teacher I have had in my entire education, and I cherish the two school years spent with you, still remembering the mix of good-heartedness, laughters, and old-school severity and discipline (Rosalie...) you imposed on us. You also got us a computer for the classroom and took us on trips to the Futuroscope amusement park, Paris and Versailles, as I now finish my studies as a world-traveling electrical engineer and physicist. I would also like to thank here Sylvie Libaros, my high-school teacher of French and literature at Lycée André Malraux (Biarritz, France), for her patience, strictness, and all the after-school pro bono hours spent in transforming my main weakness into a strength.

I would like to thank the Lorraine Region of France, the W. M. Keck Foundation, the National Science Foundation (DMR-0820382), the Air Force Office of Scientific Research for financial support, the Partner University Fund for a travel grant, the French National Research Agency (ANR), under the GANEX LABEX program and NOVAGAINS project (ANR-12-PRGE-0014-02), and CNRS INCEPT PEPS project. This research used resources of the Advanced Photon Source, a U.S. Department of Energy (DOE) Office of Science User Facility operated for the DOE Office of Science by Argonne National Laboratory under Contract No. DE-AC02-06CH11357.

I also give grateful thanks to J. Palmer, A. Savu, Y. Hu, F. Zaman, R. Dong, T. Guo, M. Ruan, B. Zhang, M. Sprinkle, J. Hicks, J.P. Turmaud, C. Bouvier, X. Yang, Y. El Gmili, M. Jordan, C. Bishop, S. Sundaram, J. Streque, J. Dickerson, M. Abid, K. Pantzas, V. Ravindran, P. McKeon, X. Li, T. Walters, K. Martin, G. Spinner, N. Devlin, C. Chapin

and D. Brown, and the whole staff of the IEN (formerly MiRC and NRC) of the Georgia Institute of Technology for training, technical support and fruitful discussions.

To Dr Azad Naeemi, many thanks for chairing the committee for my PhD proposal in October 2014, for teaching me a lot about carbon electronics, for your interest in my research, for your reactivity.

To Dr Jean-Paul Salvestrini, thank you for accepting to be part of my committee, and may our future collaborations be as fruitful as this PhD.

To Dr Paul L Voss and Dr Abdallah Ougazzaden, my advisors, thank you a lot for this wonderful opportunity and for all your support. Thanks to the both of you I have had the chance to pursue this scientific and human transatlantic adventure. Thank you for putting all of Georgia Tech, on two different continents and cultures, at my disposal, and sorry for the large lab and cleanroom bills ;)

To Dr Claire Berger and Dr Walt A. de Heer, for the use of their lab, their advice, and the immense resources they have put at my disposal. Walt, thank you for giving me a 15-minute speech on stoichiometry two years ago. This speech turned a couple of funny samples into the first chapter of this PhD thesis. Claire for always being there for me, for believing in me, for being an amazing and disciplined problem-tackling-and-solving boss, and for being such a good friend.

Last but certainly not least, I thank John Hankinson, my main coworker at the graphene lab who taught me most of the epitaxial graphene technology I know today, for his skills, patience, dedication, sharpness of mind. Not only do you make our relationship a professional success, but also a great human experience. I am glad to be friends with you, your family and your friends, and wish for other many Vortex lunches, Lake-a-paloozas, trivia nights, baseball, football (specially against the Saints), basketball games (hopefully Hawks will keep on killing it for a while), Movie-Taverns, Joystick, Hallowe'en, Thanksgivings, beerfests, beerpongs, to list only a few.

TABLE OF CONTENTS

LIST OF TABLES

LIST OF FIGURES

CHAPTER 1

INTRODUCTION

1947, in Murray Hill, New Jersey, John Bardeen and Walter Brattain of Bell Labs give birth to the point-contact transistor [32, 33], using germanium as the semiconducting medium, thus signaling the end of the over-heating and hardly miniaturizable vacuum tubes. These men also identified the effect on silicon [32], propelling mankind into the age of semiconductors and information technology, cf. Fig.1. For their discovery they were awarded the Nobel prize in Physics 1956, along with their manager William Shockley.

The same year, 500 miles north from there, Philip R. Wallace, at the time working at Chalk River Laboratory in Ontario, Canada, published his pioneering band theory of a single hexagonal layer of graphite: graphene [10], see Fig.2. Then, almost 50 years later, theoretical physicists derived the band theory of graphene ribbons [34, 35, 36]. In this work, the four physicists described the role of edge states for zigzag (always metallic) and armchair (one third metallic and two thirds semiconducting) ribbons, while outlining the crucial impact of nanometric width on the relative importance of these states.

In the meantime, the semiconductor industry blossomed to the $300 billion market it is today. Starting in 1957, the "traitorous eight," including Robert Noyce, Gordon Moore and Jean Hoerni, leave the newly Nobel laureate William Shockley to create Fairchild Semiconductor in Palo Alto, California. Their first goal was to replace the then-dominant germanium in transistors with silicon. The turning point happened one year later, when Jean Hoerni patented the planar process he developed in 1958 [37]. Performant transistors could finally be made easily and be massively produced, leading to the historic introduction of the first planar silicon transistor, Fairchild's 2N1613, in 1960. Two other major turning points were in 1959 with Noyce's first silicon integrated circuit [38], and the metal-oxide semiconductor field effect transistor (MOSFET), invented at Bell Labs by Dawon Kahng and Martin Atalla [39]. These milestones became the founding scientific breakthroughs

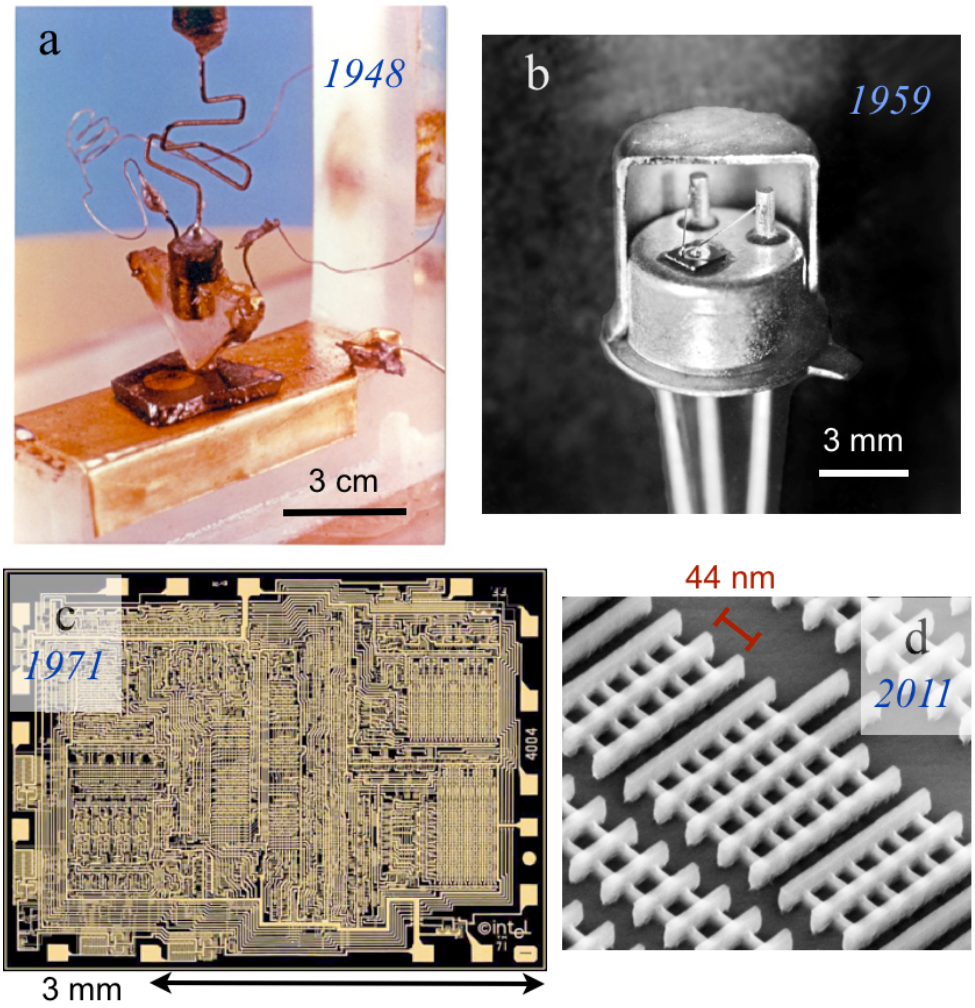

Figure 1. A brief history of silicon technology. (a) Bardeen and Brattain's first point-contact transistor (© 2006-2007 Alcatel-Lucent. All rights reserved); (b) Early Fairchild planar transistor, which led to the 2N1613 (Credit: Fairchild Camera and Instrument Corporation); (c) Intel 4004 CPU, containing 2300 transistors (Courtesy of Intel Corporation); (d) 22 nm (half-pitch) 3D transistor used on Intel i5 and i7 cores; a chip the size of 4004 now packs over one billion of these devices (Image by scanning electron microscope - courtesy of Intel Corporation).

that led to the Silicon Valley. The complimentary MOS structure (CMOS) was patented by Fairchild Semiconductor's Frank Wanlass in 1963 [40], and is still in use today.

Later, in 1968, Noyce and Moore left Fairchild to create Intel in Mountain View, California. Three years later, in 1971, Intel's Federico Faggin, Ted Hoff and Stanley Mazor, along with Busicom's Masatoshi Shima, introduced Intel 4004, the first microprocessor in the world. For more than 40 years, the semiconductor industry has kept with its founder's

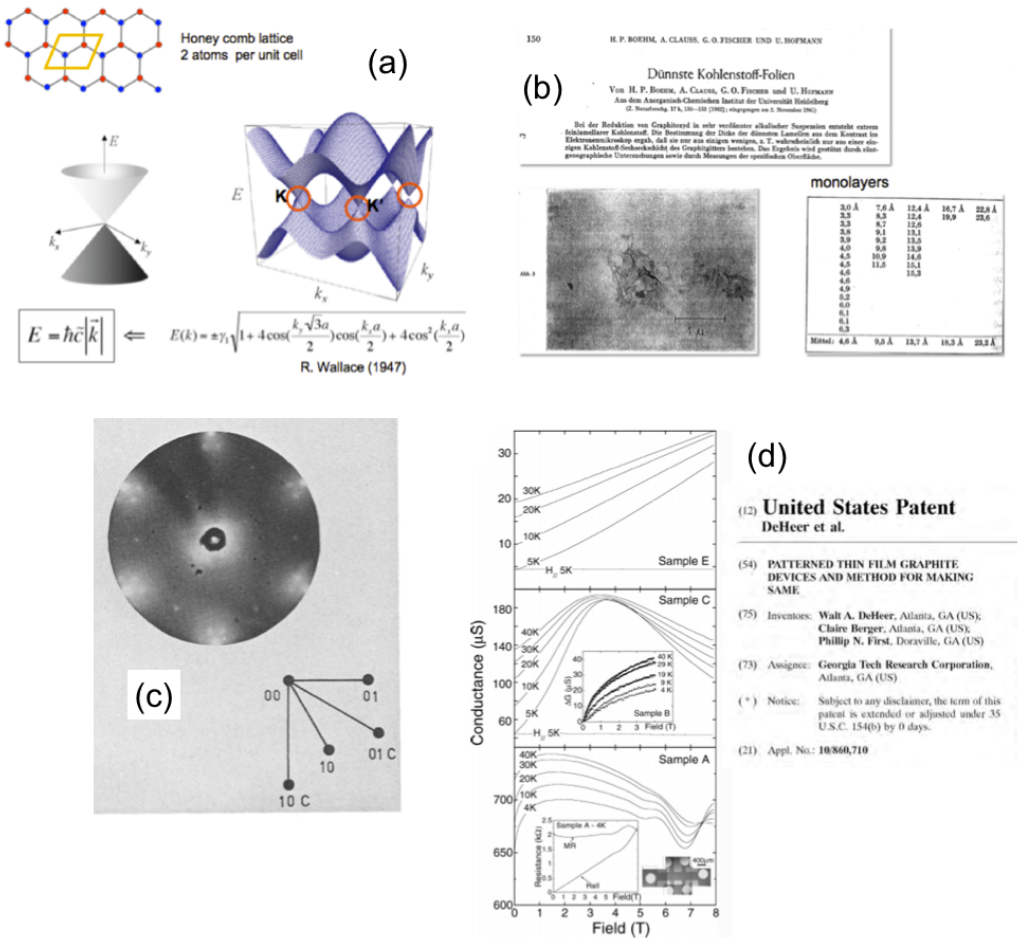

Figure 2. A short history of graphene. (a) 1947, Wallace publishes the band theory of single-layer graphene [10]. The singular intersection of the cones is now called the Dirac Point; (b) Boehm's groundbreaking observation of single-layer graphene by transmission electron microscopy in 1962. The graphene was obtained by reduction of graphite oxide [11]; (c) Van Bommel, Crombeen and Van Tooren graphitize SiC in 1975 [12]; (d) De Heer, Berger and First invent graphene electronics at the Epitaxial Graphene Lab, Georgia Tech, in 2001 [13, 14, 15].

directive, Moore's law, which is that the number of transistors on integrated circuits doubles every other year [41]. With the introduction of the 3D tri-gate transistor in 2011, Intel took an historical step forward from the planar approach to scale transistor size down to 22 nm, and even 14 nm now, with 10 and 7 nm arriving soon. Power densities now reach incredible values, on the order of magnitude of nuclear reactors, and they head toward rocket nozzles and the surface of the Sun (cf. Fig.3). Following Moore's trend via miniaturization will call for tremendous efforts to further minimize size and dissipate all of the consequent Joules.

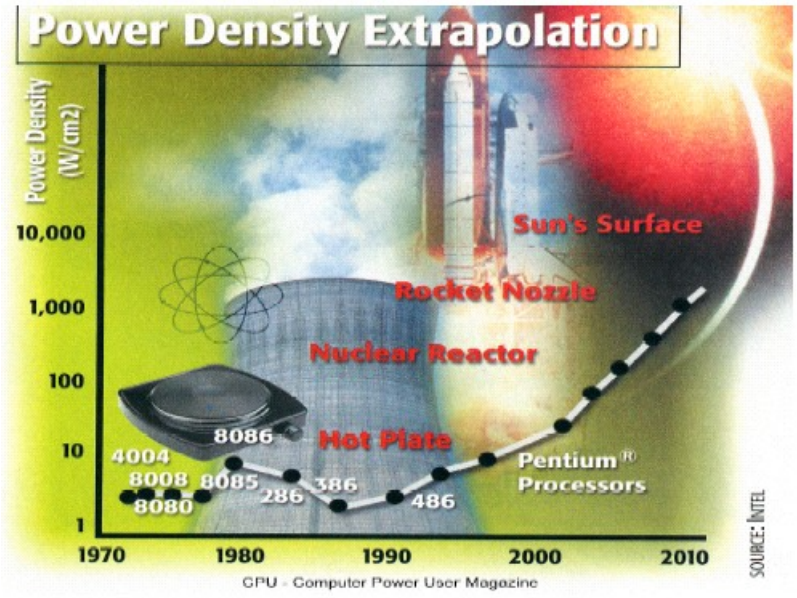

Figure 3. Evolution of power density in microprocessors over the past 40 years. (Source: Intel)

During these decades, graphene, a two-dimensional layer of sp^2-bonded carbon atoms organized into a hexagonal lattice, has been studied in many forms [10, 11, 12, 35]. A notable landmark by Hanns-Peter Boehm and his team was the first large-scale production of freestanding graphene [11], which he produced by reduction of graphite oxide. To measure and see those one-atom thick layers of carbon atoms, he used transmission electron microscopy (TEM), cf. Fig.2(a).

The band structure of graphene is described by Weyl's equation, later known as Dirac's massless relationship, where charge carriers have null rest mass and move ballistically [10, 15, 42, 43, 44, 17]. Interesting consequences are high mobilities and heatless conduction of electricity. Its potential for electronics is identified at the Georgia Institute of Technology in 2001 [13, 14] by Walt A. de Heer and Claire Berger. They, along with coworker Philip First, filed for the first patent application on graphene-based electronics in January 2003. The first electronic transport and field-effect measurements made on graphene were presented by De Heer's team in Montreal, Quebec, Canada at the March 2004 American Physical Society conference under the title "Evidence for 2D electron-gas behavior in ultra-thin epitaxial graphite on a SiC substrate" [45], 67 years after the discovery of the transistor

and the publication of the band theory of graphene. This paper, later published in 2004 in Journal of Chemistry B [15], is based on data extensively documented since 2003 [14]. It triggered a worldwide interest for the chicken-wire carbon material [46], more than 40 years after Boehm's measurements. The band structure of graphene was also first measured on epitaxial graphene (EG) [47]. De Heer's team pioneering discoveries also include electrostatic gating [15] that was contemporarily accomplished by Konstantin Novoselov and Andre Geim (the two Nobel prize laureates in Physics in 2010 [46]) on mechanically exfoliated graphene [48]; coherence and confinement effects [49]; chemical modification [50]; and exceptional ballistic transport [17], cf Fig.4.

Moreover, high-mobility graphene can be grown epitaxially by sublimation of 4H- or 6H-SiC wafers [15, 49], a well known material already massively used in the semiconductor industry. Wide-scale production of silicon carbide (also known as carborundum) was achieved 125 years ago by Edward Goodrich Acheson [51]. Starting in 1893, Henri Moissan also made groundbreaking contributions towards the identification and production of SiC, with early uses as an abrasive due its large Si-C bonding making it a chemical-proof and radiation-proof material. It is used for its semiconducting properties for the first time in 1904 by Henry H. C. Dunwoody as diode detectors for the very first radio receivers [52]. The first observation of electroluminescence also happened on SiC, three years later in 1907, as Henry Joseph Round reports emission of yellow, green, orange and blue light as he applies 10 to 110 volts on SiC crystals, mistakenly interpreted as of thermoelectric nature [53], marking the birth of optoelectronics. Nowadays SiC is a material of choice for low- and high-power transistors and diodes, wide band-gap applications (e.g., ultraviolet photodetectors, short-wave light-emitting diodes), power microwave devices [54, 55, 56], and even micro-electro-mechanical systems (MEMS) [57]. By comparison, graphene has no band gap due to its semi-metal nature; however a mobility gap can be opened, up to hundreds of meV, by lateral confinement of charge carriers via the patterning of nanoribbons [35, 58, 59].

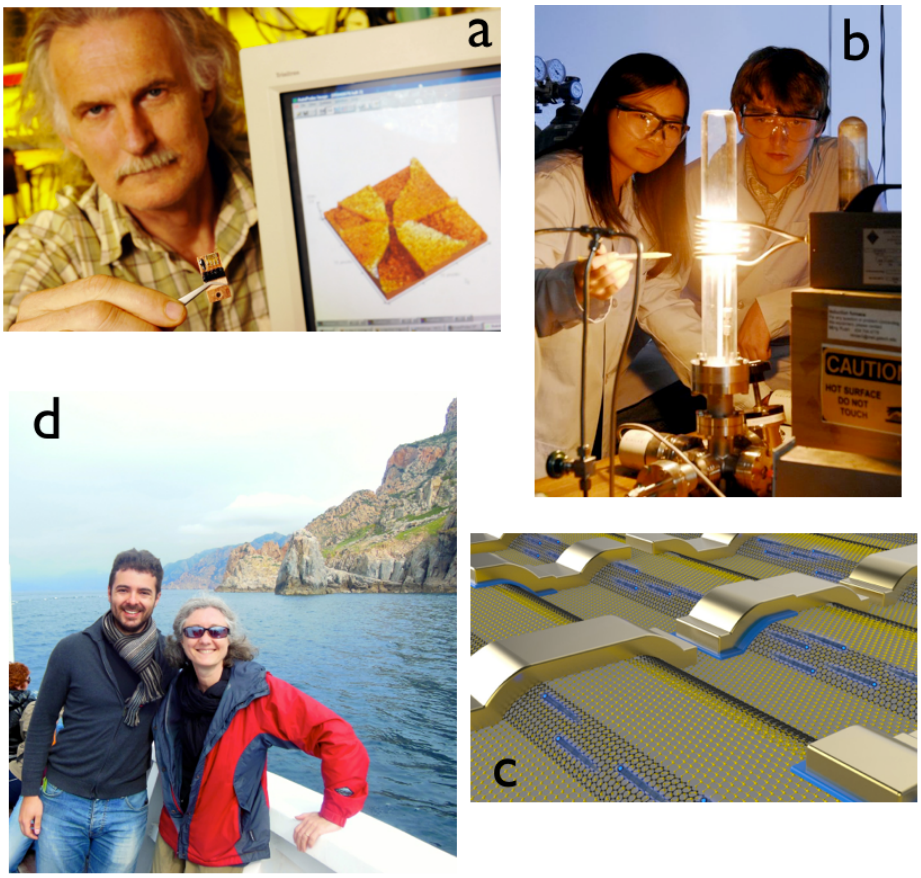

Figure 4. A short history of epitaxial graphene (Courtesy of Claire Berger and Walt de Heer). (a) Walt de Heer holding a proof-of-principle device made of epitaxial graphene in 2006 (Photo: Georgia Institute of Technology - Gary Meek); (b) 2011: Yike Hu and John Hankinson produce graphene by confinement-controlled sublimation (CCS) of silicon carbide [16] (Photo: Georgia Institute of Technology - Gary Meek) - I miss you Furnace... (c) 2013: Artistic illustration of graphene nanoribbons (black atoms) on SiC (yellow atoms) displaying exceptional ballistic transport on graphene's π electrons at room temperature in between metal electrodes [17]. Current is modulated by electrostatic gates. (© John Hankinson, Georgia Institute of Technology); (d) Claire Berger taking us to the Cargèse International Graphene School, near the Calanche of Piana, Corsica, France, in May 2014. It is a UNESCO world heritage natural site on the west coast of the island. These colorful cliffs, mostly made of granite and porphyry, were formed around 250 million years ago, making them twice older than the Atlantic ocean itself!

The ability of SiC (wide band gap at 3.23 eV for wurtzite 4H-SiC) to produce epitaxial graphene, a band-gap-free material, makes this extraordinary carbon-silicon system an ideal base for post-silicon-CMOS electronics and optoelectronics. Recent findings have propelled epitaxial graphene on SiC into the optimal candidate for future large-scale industrial electronics. These breakthroughs include large-scale integration of epitaxial graphene

devices [60], half a century after Noyce's first silicon integrated circuit; also highly-efficient spin transport [61]; and the creation of nanometric metal-semiconductor-metal junctions entirely made of graphene, exhibiting half-eV energy gaps [62]. Last and certainly not least among these recent discoveries are graphene sidewall nanoribbons [63]. They turned out to be single-channel ballistic conductors [17], and not semiconductors, with room-temperature mobilities over one million and sheet resistance below 1 Ω, breaking the theoretical limit for perfect graphene by over a factor of ten [64]. This limit has been originally set by the temperature-dependant scattering of charge carriers by longitudinal acoustic phonons in the 2D crystal lattice. Furthermore because SiC is a monocrystalline semiconducting industrial substrate, epitaxial graphene on SiC is directly compatible with established scalable device fabrication techniques, making it attractive for advanced electronic devices [15, 65], for example high-frequency transistors [66, 67]. To summarize, epitaxial graphene is a riveting medium for its conductive π electrons: maximum achievable mobility, without scattering and its thermal consequences. And this ballistic transport is achieved on a relatively low-cost material [68], compatible with large-scale semiconductor industrial processes: silicon carbide. All these properties make epitaxial graphene on SiC a possible successor (and not replacement!) for silicon, and a brand new player in the electronics industry.

Now let's go back to the beginning of the twentieth century: in 1907 H. J. Round observes spontaneous emission of the full spectrum of visible light from SiC crystals, as mentioned earlier [53]. Will follow Russian scientist Oleg Vladimirovitch Losev in 1920 when he also identifies light emission from point-contact rectifier diodes made from the very same material [69, 70]. Since the end of the 19th century SiC had been produced using Acheson process [51], to be replaced by Jan Anthony Lely's technology in the 1950s [71]. Lely's recipe still inspires production of SiC nowadays, with for example Cree Inc. (our supplier of 4H-SiC at the epitaxial graphene lab) using a technique known as the seeded-sublimation process, a.k.a. modified Lely's technology, involving induction heating

in graphite crucibles [72]. Losev was also the first to identify the non-thermal nature of the emitted photons [73] and he consequently fully characterized this new type of light emission [70].

But we will have to wait until the early 1960s for spontaneous emission to become a potential commercial success. In 1961 James R. Biard and Gary E. Pittman invent the first practical light-emitting diode at Texas Instruments, based on infrared light emission originating from an injection of current into a GaAs crystal. The next year they filed the patent [74] and Texas Instruments announces the first commercial LED, the SNX-100, emitting at 900 nm (near-infrared). This also marks the arrival of direct-band-gap semiconductors at the forefront of optoelectronics technology, way more efficient at emitting light thanks to their faster radiative recombination of electron-hole pairs.

The same year, in December 1962, General Electric's Nick Holonyak Jr. invents a red LED, the first one emitting in the visible spectrum, by including phosphorus into GaAs to create $GaAs_{1-x}P_x$ crystals [75] (Fig.5a). Ten years later, in 1972, M. George Craford (previously graduate student under Dr Holonyak's supervision), invents the first yellow LED with nitrogen-doped $GaAs_{1-x}P_x$ alloys [76] (Fig.5b). Craford, Holonyak, along with a former student of the latter and current Yellow Jacket Russell D. Dupuis, were awarded the 2002 U.S. National Medal of Technology for their "contributions to the development and commercialization of light-emitting diode (LED) technology". In parallel, Herbert Paul Maruska is at the forefront of nitride technology: in 1969 he and J. J. Tietjen, then at RCA Laboratories in Princeton, New Jersey, USA, grow GaN on c-sapphire [77], and they even study the potential of magnesium as a p-type dopant for this naturally n-type material. And in 1972, still using Mg for p-doping, Maruska, Rhines (then graduate students at Stanford), and their advisor Stevenson, build the first actual blue-violet emitting diode, hence completing the visible spectrum [78] (Fig.5c-c'). This technological breakthrough, also made possible thanks to Jacques Pankove's contributions [79, 80], is quickly secured by a publication in Materials Research Bulletin [81] and a U.S. patent [82].

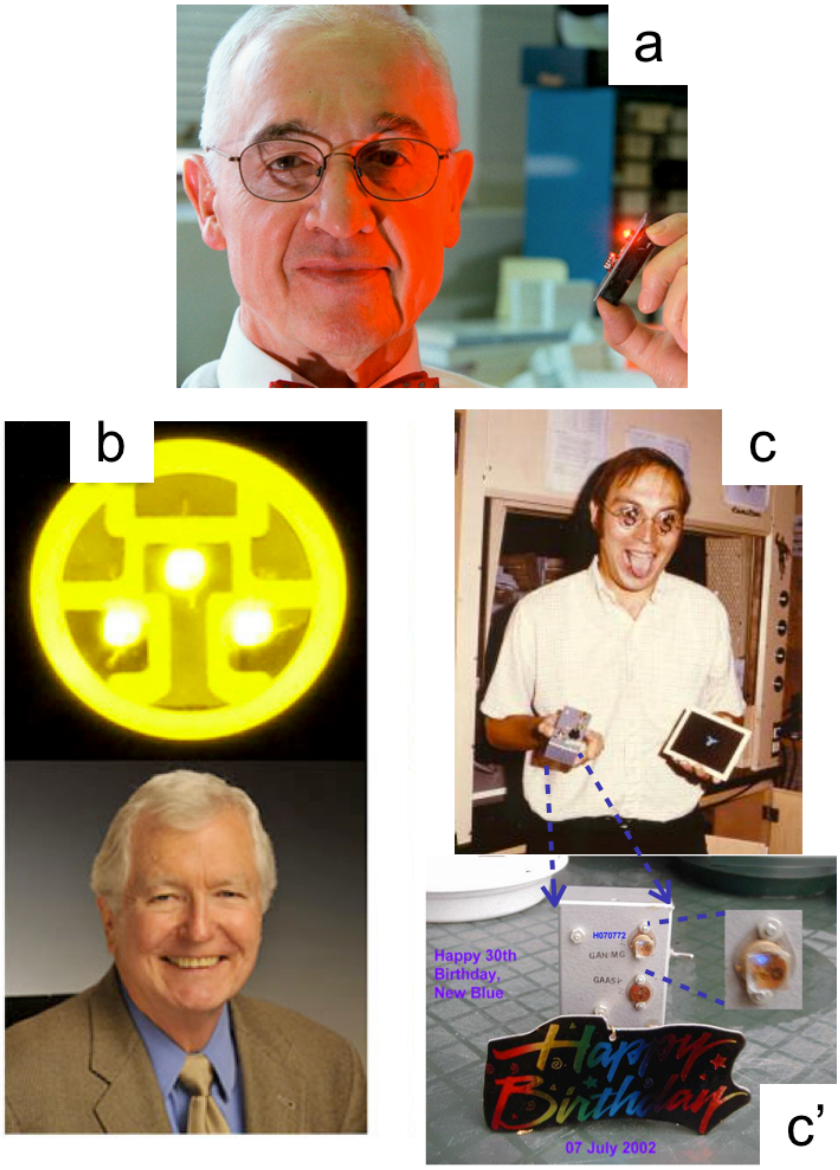

Figure 5. Chromatic history of the spontaneous emission of light. (a) Holonyak holding a red LED as invented in 1962 (Photo by Tom Roberts, News-Gazette, courtesy of University of Illinois at Urbana-Champaign, news.illinois.edu); (b) Craford and his yellow LED invented 1972 (Photo: Semicon West 2012); (c) Maruska holding the first blue-violet LED the very same year, 1972; (c') The very same device is still working 30 years later in 2002! (c-c' are photos by Herb Maruska, cf. Ref. [18]).

However Mg p-type doping still remained an issue for GaN, as it could not be concentrated enough to make the GaN conductive. Isamu Akasaki and Hiroshi Amano solved this issue in 1989 using electron-beam annealing to create a conductive Mg-strongly-doped p-type GaN layer, opening the possibility of an efficient blue LED [83]. Shuji Nakamura, then

at Nichia corporation, followed in 1994-95 by building quantum-well heterostructures of InGaN and AlGaN. This research led to high-brightness blue LEDs with quantum efficiencies exceeding 10% and made the whole process easily compatible with optoelectronics manufacturing technologies [84, 85, 86]: affordable white LED bulbs were within reach. For their contributions Akasaki, Amano and Nakamura were awarded the 2014 Nobel prize in physics.

Silicon carbide and III-nitrides have been intensively used in the industry for the production of high-frequency electronics, power electronics, and optoelectronics, both separately and grown on each other [87]. On the other side, silicon has been dominating the semiconductor market, but we are reaching its physical limits. Hence could epitaxial graphene on SiC be considered a possible successor for Si, and could it open new roads towards the fabrication of novel and more performant high-frequency, power-, and optoelectronics?

CHAPTER 2

TAILORING GRAPHENE GROWTH USING VANISHING PATTERNS OF SILICON NITRIDE [1, 2, 3]

Epitaxial graphene (EG) on SiC shows compelling physical characteristics such as ballistic transport in nanoribbons [17], half-eV band-gap structures [62], metrology standard quantum-Hall effect [88] and high frequency transistors [66, 67]. Epitaxial graphene on the 4H-SiC $(000\bar{1})$ C-face shows high electronic mobility [89], up to $10^6\ cm^2/Vs$ at room temperature for the inner layers [90], a record-high maximum oscillation frequency transistor operation [67] and spin diffusion length two orders of magnitude longer than any other material [61]. Because SiC is a monocrystalline semiconducting industrial substrate, epitaxial graphene on SiC is directly compatible with established scalable device fabrication techniques, making it interesting for advanced electronic devices as well [15, 65]. Patterning of clean graphene devices is key for both the study of physical properties and technological improvement. In most cases, 2D graphene is first grown then patterned by oxygen plasma. However resist residues, that can cause unintentional doping or scattering, are difficult to eliminate. It is also well established that etching increases structure edge roughness and degrades transport properties [58]. Selective area graphene growth is a more straightforward approach, as it could in principle provide patterned structures directly during epitaxy. Local control of graphene growth has been previously achieved by AlN capping [91], ion implantation of Au or Si [92], or on side-wall nanoribbons [63]. However, in these cases the foreign atoms remain in the system or the graphene is limited to very narrow structures.

The first topic of this PhD thesis concerns the discovery of a new method for controlling graphene growth down to the sub-micron level, by using vanishing silicon nitride

masks. Deposition of a 120 nm- to 150 nm-thick silicon nitride (SiN) mask on the carbon-terminated face $(000\bar{1})$ of silicon carbide (SiC) prior to graphitization modifies the relative number of multi-layer epitaxial graphene (MEG) sheets [19] grown by confinement-controlled sublimation (CCS) of SiC [16]. The silicon nitride mask decomposes and vanishes before graphitization is complete. Importantly, the off-stoichiometry of the $Si_{3+x}N_4$ coating controls whether the silicon nitride layer enhances or suppresses graphene growth relative to uncovered areas. We find that N-rich $Si_{3+x}N_4$ masks decrease the average number of layers by three compared to uncovered regions while Si-rich silicon $Si_{3+x}N_4$ increase thickness by two to four layers. The graphene layers of samples prepared with nearly stoichiometric Si_3N_4 show good mobilities up to 7100 $cm^2.V^{-1}.s^{-1}$, with electron concentrations in the 10^{12} cm^{-2} range. Raman spectroscopy and AFM measurements confirm that the graphene grown in areas initially covered by the mask has good structural quality. Interpretations for the observed phenomena are proposed, as well as a thermodynamical study of the SiN / SiC system.

2.1 Silicon nitride deposition and graphene growth

After preparation of the surface of 3.5 x 4.5 mm^2 4H-SiC wafer dies by a high temperature hydrogen etch [16], silicon nitride is deposited by low-power plasma-enhanced chemical vapor deposition (PECVD) using SiH_4 and NH_3 as precursor gases. We have confirmed by AFM measurements after removing SiN with hydrofluoric acid (HF) that the plasma does not result in detectable damage to the SiC surface.

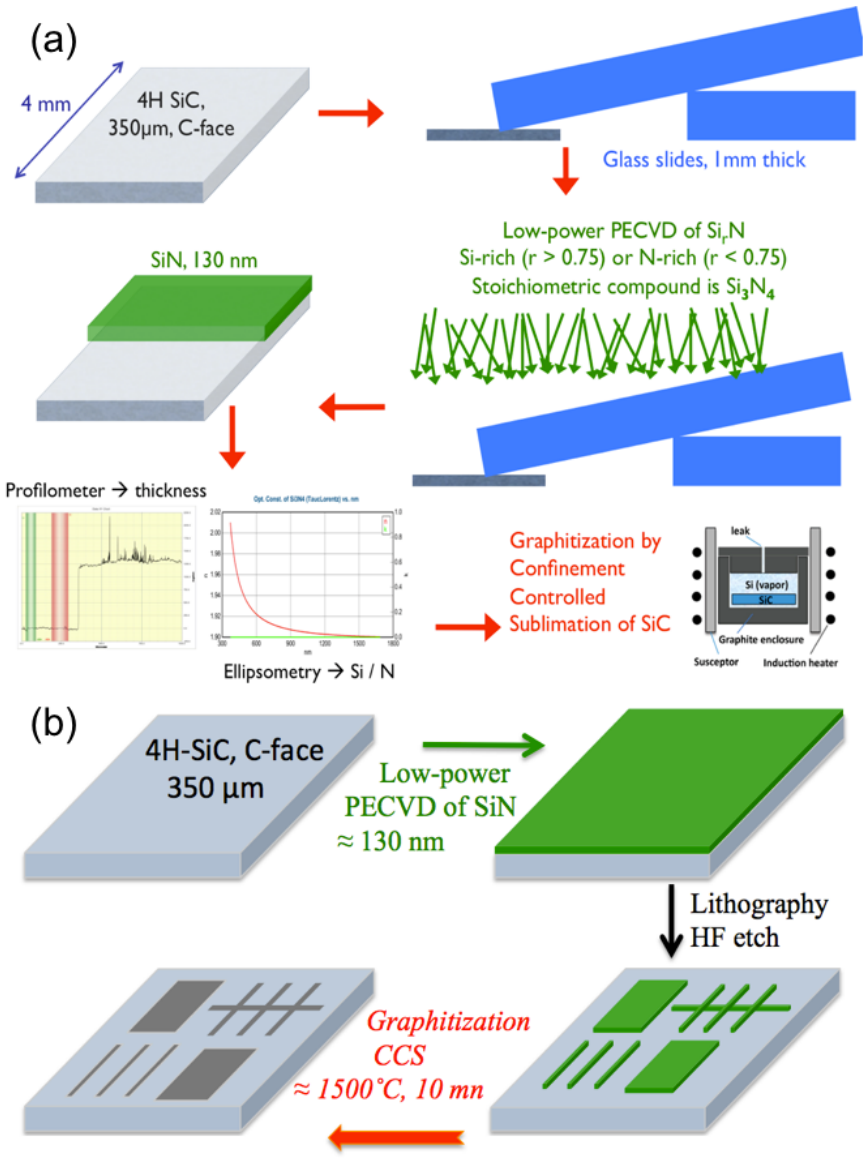

Figure 6. Two different approaches for SiN deposition: (a) on half the sample using a glass slide as a mask; (b) using standard lithography and buffered oxide etch (hydrofluoric acid).

SiN has been deposited using two different processes. For most of the study of silicon nitride composition and its impact on graphene growth, SiN was deposited only on one half of each 3.5 x 4.5 mm^2 using a glass microscope slide as a mask, cf Fig.6(a). Once the technology proved controllable and repeatable, we switched to processing patterns of SiN, which were achieved by standard lithography, using PMMA as the resist, and HF as the etchant (harmless to SiC), as schematized in Fig.6(b).

We estimated the stoichiometry of the SiN films as a function of the precursor ratio (SiH_4 / NH_3) by measuring the refractive index at 632.8 nm ($n_{632.8}$) of the SiN films with an ellipsometer. Following Refs. [93, 94], $n_{632.8}$ is approximately linearly dependent on the atomic ratio Si/N in the deposited film:

$$\frac{Si}{N} = \frac{n_{632.8} - 1.35}{0.74} \tag{1}$$

Fig.7 gives a calibration of the SiN composition as a function of the precursor ratio (SiH_4 / NH_3) in the PECVD process. The straight line is a linear fit of the data.

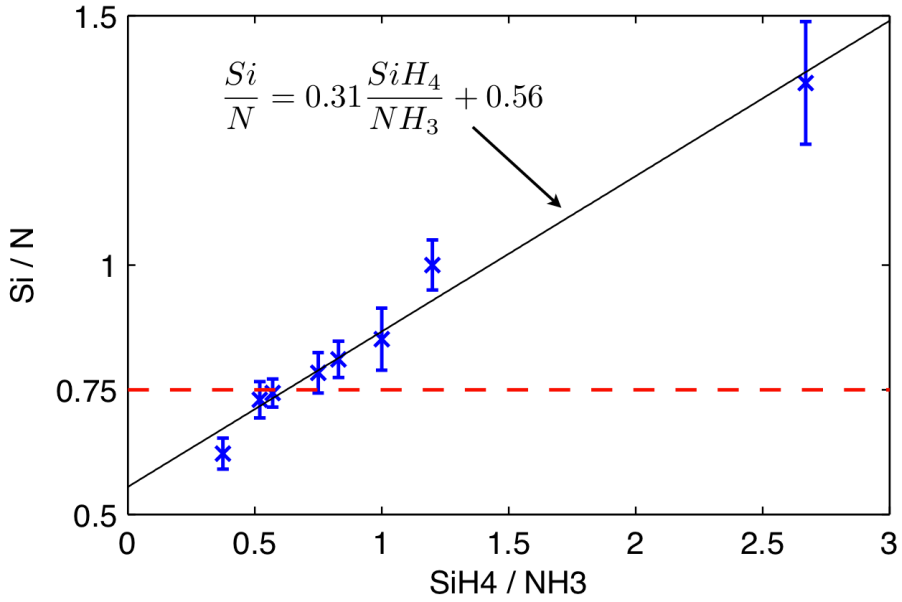

Figure 7. Calculated atomic ratio of Si over N in the grown SiN film as a function of SiH_4 / NH_3 precursor ratio. This fraction divides the flow of silane by the flow of ammonia, flows typically expressed in standard cubic centimeters per minute (sccm) in the PECVD reactor. Atomic ratio Si / N of 0.75 (dashed red line) corresponds to stoichiometric Si_3N_4.

Confinement-controlled sublimation (CCS) of SiC is used for graphene epitaxy [16], cf. Fig.8. This technique consists in heating a SiC chip in a graphite enclosure connected to a vacuum chamber (about 10^{-5} mbar) by a calibrated hole. This increases the built-in Si partial pressure, which controls the rate of silicon sublimation from the SiC surface, bringing the graphene growth process close to equilibrium.

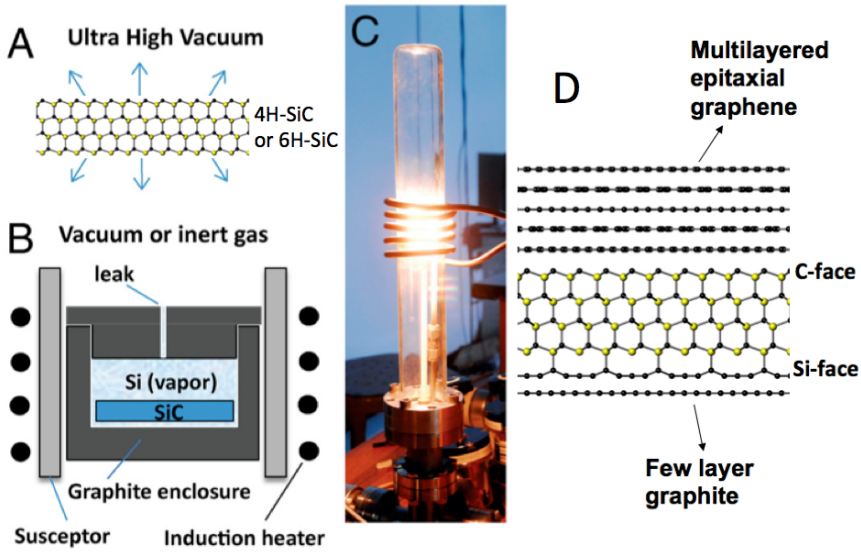

Figure 8. The confinement controlled sublimation (CCS) method. (A) Without confinement of the sublimed Si, growth happens far from equilibrium, causing rapid graphitization; (B) In CCS technology, growth rate is controlled by the length and section of the aperture (leak), and the background gas pressure; (C) Photograph of the induction furnace; (D) Illustration of the difference in graphitization under CCS conditions: on the carbon terminated face $(000\bar{1})$ of SiC, 1 to 50 layers of multi-layer epitaxial graphene (MEG) grow [19], while the Si-face (0001) gives 1 to 5 layers of few layer graphite (FLG). (Courtesy of W. A. de Heer and Claire Berger)

A key component in the control of C-face (and even Si-face) sublimation of SiC and graphene formation is the initial stage of the crucible. Fig.9 illustrates the necessary "Si-loading" necessary for full control of growth, leading to a whiter inside wall of the crucible, probably composed of SiC and Si-infused graphite (still to be precisely studied and identified). Here the right-hand crucible, named HP1, has been re-initialized using a dummy SiC sample (typically a piece on the border of the wafer) at very high temperature (1600°C instead of 1420-1500°C for standard C-face growth). The left-hand crucible, HP2, has just

been made exactly similar to HP1 (and cleaned of course); it is used here as a control crucible for contrast comparison. More interestingly, a darker area right above the arrow of the right-hand crucible HP1 can be seen: this corresponds to the area of contact with the cap. This surface is not exposed to Si sublimation, hence exhibiting the pristine black color of bare graphite.

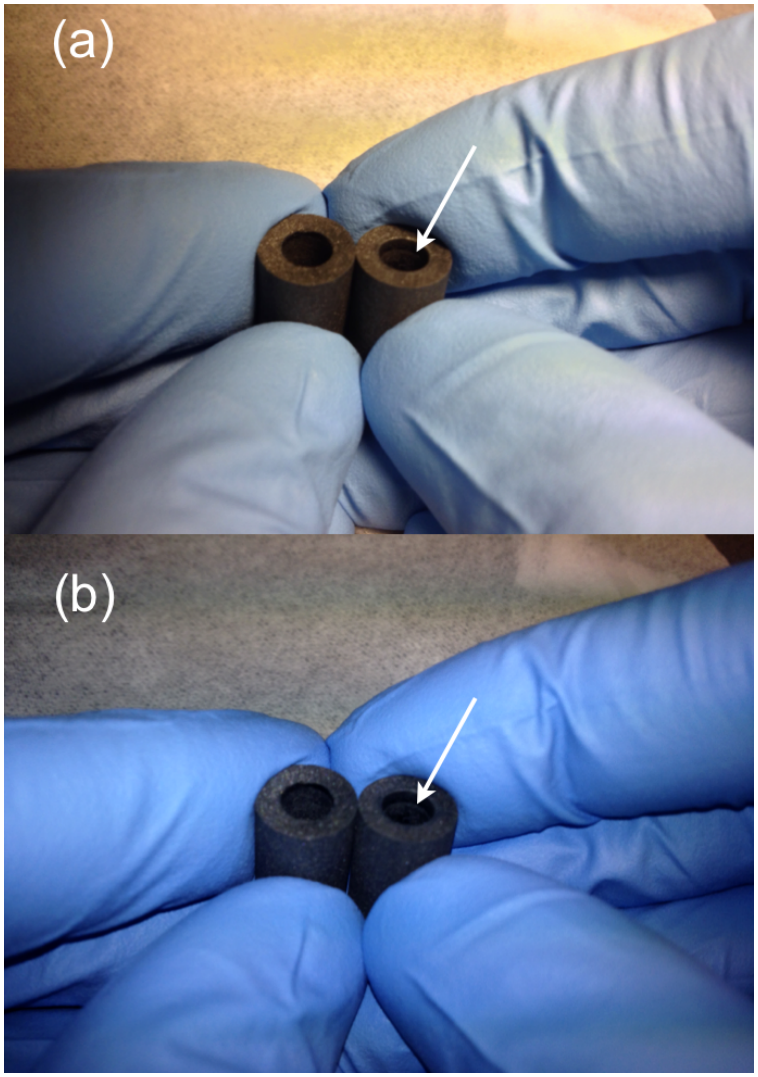

Figure 9. Pictures of 2 different crucibles (with help from James Palmer): (a) taken without flash, (b) with flash. The left-hand crucible has never been used for graphitization, used here as a control for contrast comparison. The right-hand crucible has been used for a vast majority of growths, with and without SiN masks, in the thesis. The white arrow points at the naked-eye visible white "Si-loading" of the crucible, probably made of SiC and Si.

The growth process consists of 10 minutes at 800°C, followed by graphene growth

between 1420 to 1550 °C for 8 to 20 minutes. One exception in Fig.10 is sample Si4, which after the 800°C annealing, was held at 1150 °C for 20 minutes, and then graphitized.

After graphitization the SiN mask has vanished. The Raman spectra show neither the Si-H nor the N-H stretching modes [95], respectively at 2190 and 3360 cm^{-1}, that were observed before growth (discussed later in Section 2.5). AFM images (cf Figs.11 and 12) show the typical SiC terraces and pleat structure of epitaxial graphene with no AFM nor Raman evidence for left-over SiN in both Si-rich and N-rich cases. The SiN layer is expected to decompose into solid Si and gaseous N2 during the 1150°C plateau [21, 20, 22]. The remaining Si sublimates during graphitization around 1500°C, consistent with CCS growth [16].

Ellipsometry measurements (Horriba Jobin-Yvon AutoSE) on half-masked samples are reported in Fig.10. We used a spot size is 250 x 250 μm^2, and analyzed response in the range 440 nm to 850 nm, with a three-term Cauchy model optimized for 4H-SiC and graphene layers [96]. Each thickness reported in Fig.10 is the average of 12 measurements, spread on the whole analysed surface. We observe 2 to 3 additional layers of graphene under the Si-rich initially masked (IM) areas, and consistently 3 fewer layers under the N-rich IM areas, compared to the initially bare (IB) half on each sample. Sample Si4 (Si-rich $Si_{3+x}N_4$ mask), which had an additional higher temperature annealing step at 1150°C, shows 4 to 5 additional graphene layers. The increased (reduced) number of graphene layers depending if the mask is over- (under-) stoichiometric was observed in a total of 20 samples, of which 8 have a precise composition measured as reported in Fig.10. Note that the excess number of layers doesn't seem to depend on the over-stoichiometry; however, the over-stoichiometry impacts the quality of the graphene films. For the same growth conditions graphene is more disordered for Si-rich SiN, as shown by a higher Raman D peak.

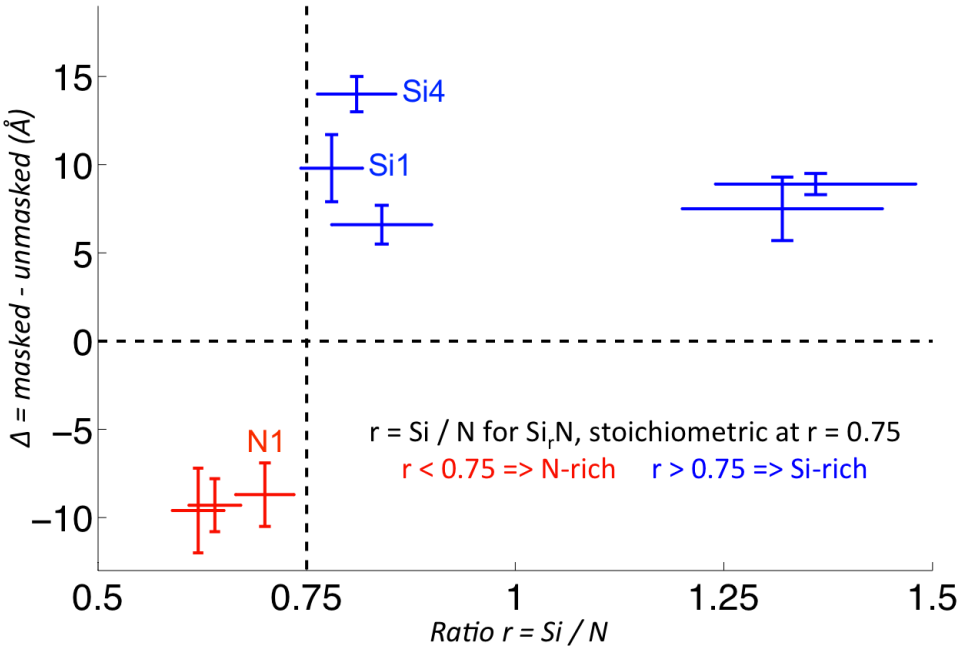

Figure 10. Local control of thickness as a function of the composition of the silicon nitride film, of stoichiometric formula Si_3N_4. In red, the Si_rN mask was N-rich; in blue, Si-rich Si_rN.

2.2 Raman spectroscopy, AFM, and transport measurements

Raman spectra (wavelength is 532 nm) and atomic force microscopy (AFM) topographic images of samples N1 and Si1 are shown in Figs. 11 and 12, respectively. Of all the samples studied, the silicon nitride films deposited on N1 and Si1 were the closest to stoichiometric Si_3N_4, cf Fig.10. These samples had the lowest Raman D peaks, sharpest 2D peaks, and smoothest AFM images, and hence were patterned for electronic measurements. More specifically sample N1 was grown for 10 minutes at 1450°C and sample S1 for 9 min at 1480°C; the mask composition for S1 is Si/N = 0.78, and 0.70 for N1; the thickness is 130 nm.

The Raman spectra of the IM and IB areas of N1 and the IM area of Si1, reveal the characteristic graphene peaks, see Figs. 11 and 12. The graphene 2D and G Raman peaks are clearly identified (the SiC Raman contribution was subtracted). The 2D peak can be fitted by a single Cauchy-Lorentz distribution [97] centered at 2699 cm^{-1} for the IM area of N1 (2700 cm^{-1} and 2689 cm^{-1}, respectively for the IB part of N1 and the IM half of Si1)

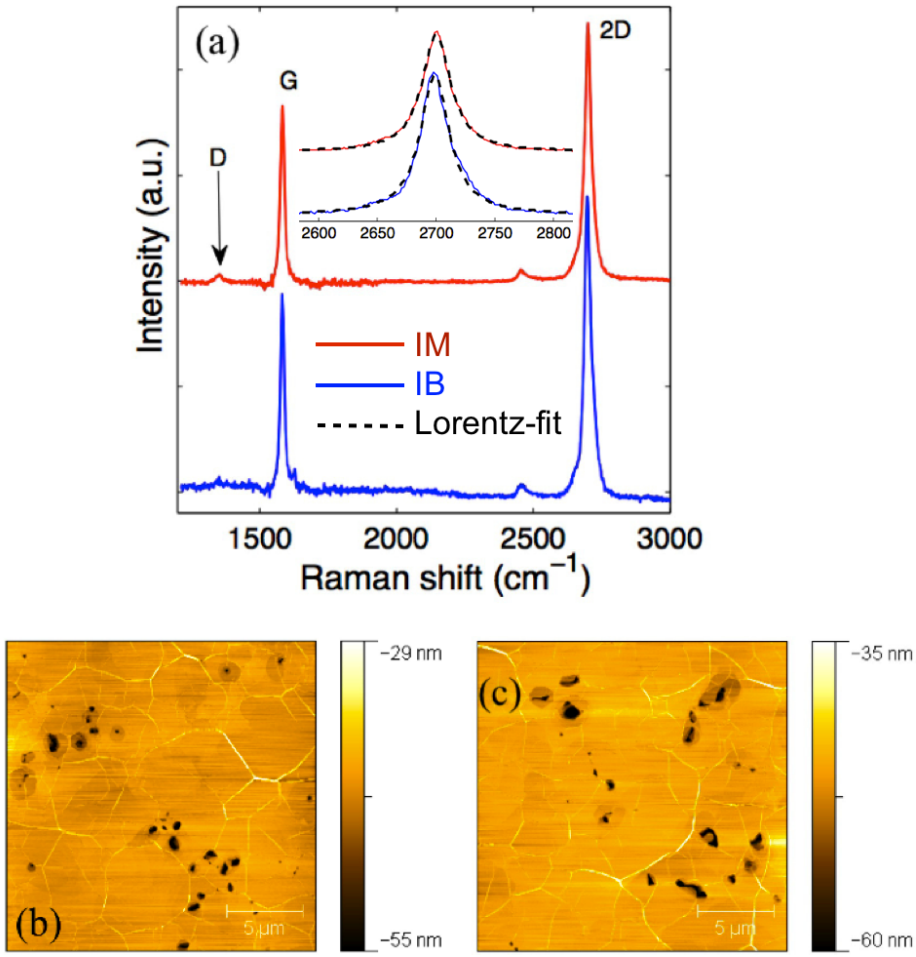

Figure 11. Sample N1, N-rich $Si_{3+x}N_4$ mask. (a): Raman spectra (SiC contribution subtracted) of IM and IB areas. (b)-(c): AFM images of (b) IM area and (c) IB area (scale 20x20 µm^2) showing the typical graphene pleat structure observed in MEG samples.

with FWHM= 29 cm^{-1} (36 cm^{-1} and 29 cm^{-1}, respectively). The D peak at 1350 cm^{-1} is very small, and even undetectable for Si1 and N1. This indicates low defect density in the graphene lattice. For the other samples of Fig.10, the 2D peak is centered from 2706 to 2726 cm^{-1}, with FWHM from 52 to 70 cm^{-1}, consistent with 2D MEG [97]. The higher D peaks and the broader blue-shifted 2D peaks (at FWHM 52-70 cm^{-1}) for the other samples referenced in Table 1 reveal respectively smaller domain sizes and compressive strain in the graphene [98]. Specifically, we do not observed the characteristic shouldered 2D peak of highly ordered pyrolitic graphite (HOPG), as already reported for multilayered epitaxial

graphene on the C-face [97]. The slight asymmetry of the IB 2D peak in Fig.11(a) may be due to a variation of strain in the graphene stack or a small fraction of Bernal stacking fault [97, 98]. MEG and FLG on SiC with a 2D-FWHM of 58 cm^{-1} (Ref.[91]), 68 cm^{-1} (Ref.[99]) and even 71 cm^{-1} (Ref.[98]) have already been reported.

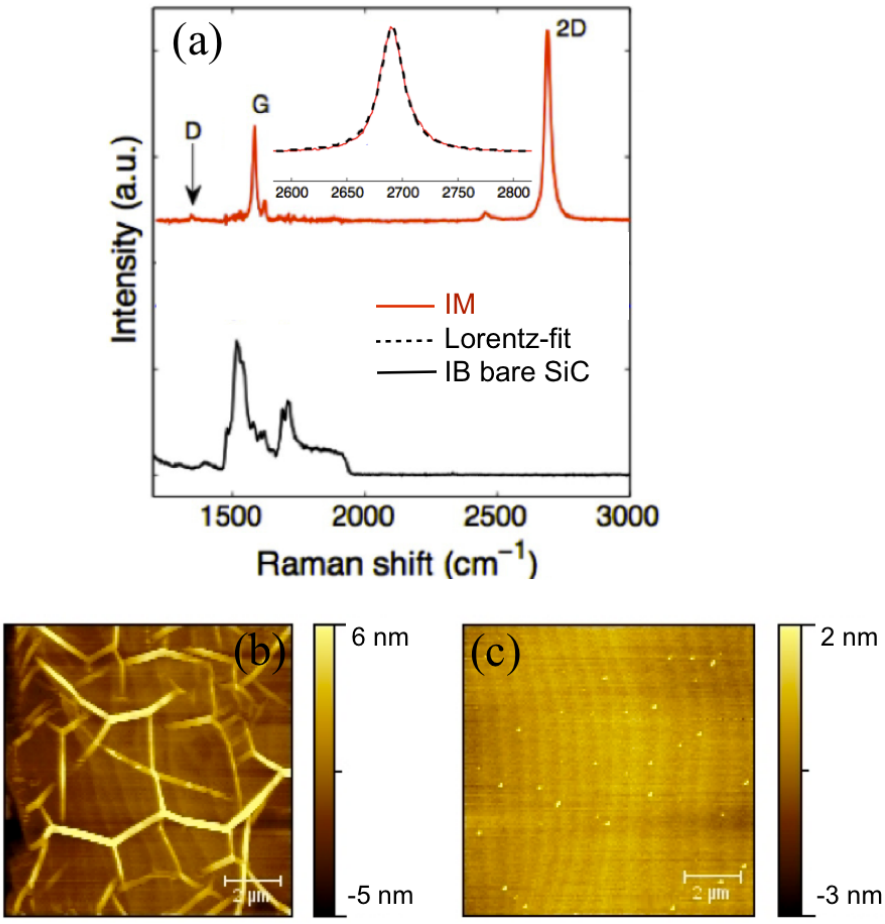

Figure 12. Sample Si1, Si-rich SiN mask. (a): Raman spectra (SiC contribution subtracted), showing the typical MEG spectrum. For the Raman spectrum the intensity is normalized to the SiC plateau at 1900 cm^{-1}. Note the quasi absence of D-peak. (b)-(c): AFM image of (b) IM area (scale 10x10 μm^2), and (c) IB area (scale 10x10 μm^2).

The AFM images of Figs. 11 and 12 confirm the presence of graphene, as shown by the MEG characteristic pleat structure [16]. In the graphitized areas, the AFM images in Fig.11(b)-(c) and Fig.12(b) have a comparable characteristics in terms of pleat structure, including pleat height (1.5-2.4 nm), pleat surface density and semi-hexagonal orientation.

Sample Si1 is particularly interesting in that while the IM area is fully coated with graphene with an average of 3 layers, the IB area is essentially not graphitized, as seen in the Raman spectra, ellipsometry and AFM images. On the AFM image of Fig.12(c), a bare SiC step structure can be observed, which is confirmed by Raman spectroscopy, cf Fig.12(a). MEG growth is observed in some spots, most probably initiated at screw dislocations in SiC, as already observed [89, 100]. This indicates selective growth, with graphene where the mask was, and almost no graphene elsewhere.

Hall bars (5 µm long, 3.5 µm wide) were patterned in sample Si1 and N1 using electron beam lithography, oxygen plasma etching and Ti/Pd/Au contacts (thickness 0.5/20/40 nm). From room temperature Hall and magnetoresistance measurements, electronic mobilities are found between 3200 and 7100 $cm^2.V^{-1}.s^{-1}$, and carrier concentrations are in the 10^{12} cm^{-2} range, showing excellent graphene quality, as seen in Fig.13.

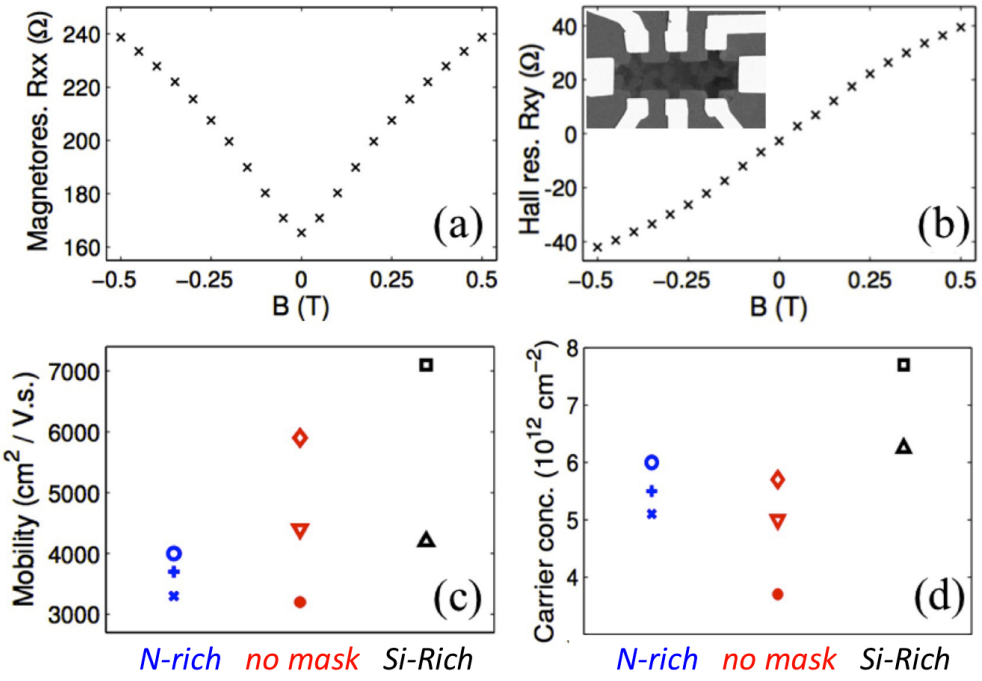

Figure 13. (a) (b): Magneto- and Hall resistances at room temperature of IM area of Si1, in the tables represented by the little black square: n=7.7 e^{12} cm^{-2} and µ = 7100 $cm^2.V^{-1}.s^{-1}$. *Hall bar (SEM picture in the inset) is 3 µm wide.* (c) (d): Mobility and carrier concentrations at room temperature measured on the IM area of N1 (N-rich SiN), IB area of N1 (no mask), and IM area of Si1 (Si-rich SiN).

2.3 Patterning capabilities of the technology

As a demonstration of the capability of the method, graphene has been selectively grown in various shapes. Fig.14, representing Buzz, the mascot of Georgia Tech, demonstrates that the sub-micrometer resolution of the SiN mask pattern (Fig.14a) is directly transferred to the selectively grown graphene, as shown by optical contrast (Fig.14b) and Raman spectroscopy maps of the characteristic 2D and G graphene peaks. The optical image correlates nicely with the Raman maps, as expected for graphene on SiC [101]. The absence of 2D peak in the dark areas of Fig.14c-d demonstrates selectivity.

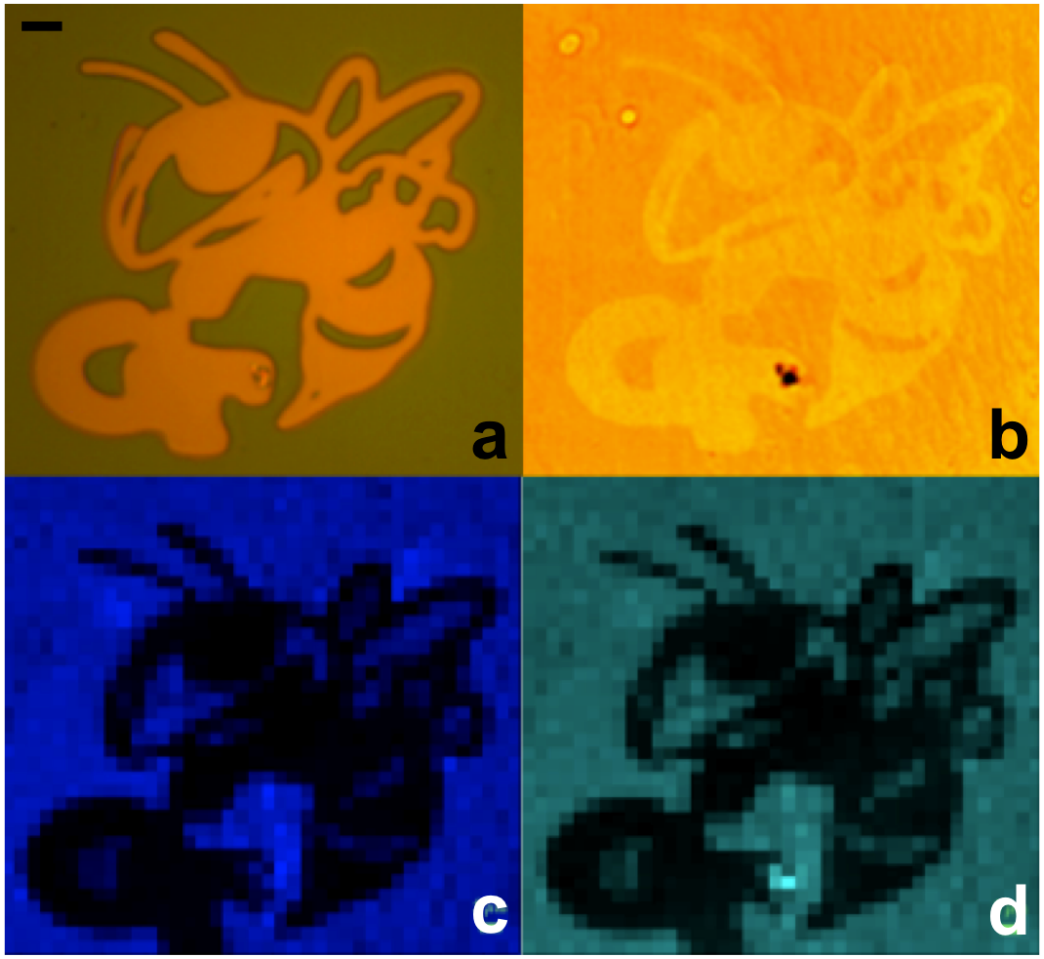

Figure 14. Buzz-of-principle, MEG on SiC using Si-rich SiN mask, demonstrating sub-micron resolution. a: SiN pattern, optical view. b: Subsequent MEG growth on SiC, contrast-enhanced optical image. c: Raman 2D map. d: Raman 2D/G map. Scale bar is 10 μm.

Repeatability has been demonstrated on many samples and various patterns. Fig.15 shows a Hall bar pattern. Unfortunately it could not be measured for the Hall effect, as the SiC substrate was partially graphitized, and hence was short-circuiting the graphene pads. Fig.16 illustrates again the sub-micron capability of this technology.

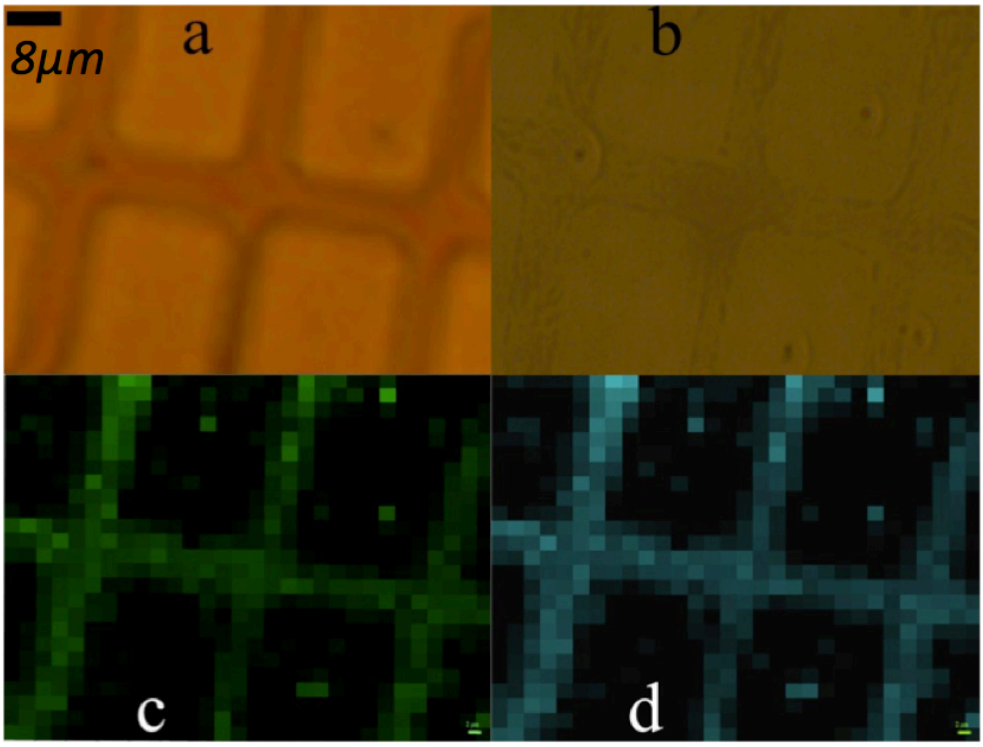

Figure 15. Selectively grown bilayer C-face graphene Hall bar, with (a) SiN mask, (b) subsequent graphene growth, (c) Raman 2D peak mapping and (d) Raman 2D/G map.

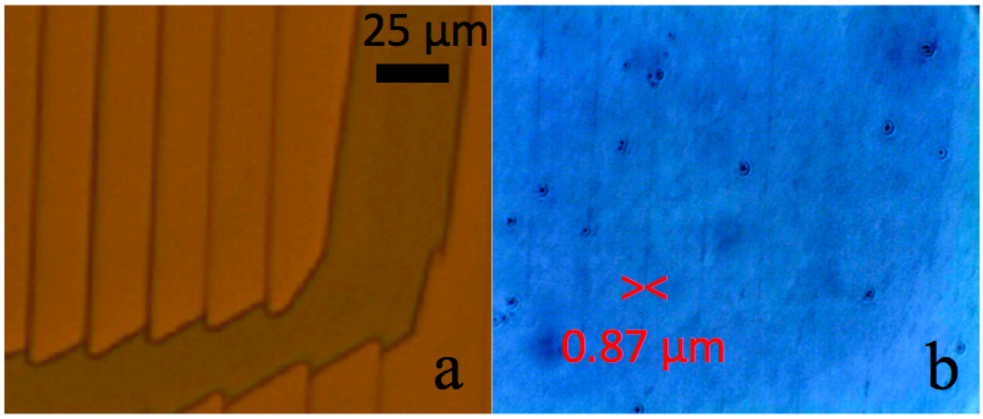

Figure 16. Array of sub micron lines of 3-4 layer C-face graphene on monolayer graphene.

The main result of this study is that the presence of a silicon nitride mask evaporated

on silicon carbide prior to graphitization enhances (Si-rich $Si_{3+x}N_4$ mask) or reduces (N-rich $Si_{3+x}N_4$) the number of layers grown compared to uncovered areas. Control samples, grown in the same condition but with no mask, have the same number of layers (within one layer) as the IB areas.

A simple explanation for the reduction of the number of layers under the N-rich masks would be that graphitization is delayed under the mask, starting only after SiN decomposition. It is known that capping SiC with an AlN mask, that doesn't evaporate, prevents graphene formation [91]. More surprising is the enhanced number of layers under the Si-rich mask. An example of enhanced graphene growth is Si-implanted SiC surfaces, which form graphene at lower temperature than pristine SiC; however this enhancement in Si sublimation has been attributed to the break of Si-C bonds and the resulting damaging of the SiC surface [92]. A possibility is that Si dangling bonds present in the Si-rich-SiN mask [102, 103, 104, 105] react with SiC. Si dangling bonds at SiN_3 sites have already been proposed as the dominant defects in Si-rich and stoichiometric PECVD silicon nitride, acting as amphoteric traps [104]. Moreover, in N-rich films, electron spin resonance (ESR) studies have shown that the density of these defects is greatly reduced or even suppressed [106], making N-rich $Si_{3+x}N_4$ a better dielectric than Si-rich $Si_{3+x}N_4$ films. However the exact mechanism per which the growth is enhanced will require far more study. The decomposition of SiC and graphene growth is not well understood even in the simple case of a bare SiC surface. For instance the growth rate is extremely slow on the Si-face but is much faster on the C-face. Out-diffusion of silicon is clearly the key, pointing to the role of Si in the capping SiN mask.

2.4 Thermodynamics

Such an interpretation needs to be consistent with thermodynamics. SiN decomposes into condensed Si and gaseous nitrogen [21, 20], at around 1000°C in the pressure range existing during CCS. An analogy can be observed with SiC decomposition at higher temperature, except for Si_3N_4 Si is the left-over product, while volatile N_2 is evacuated from the graphite Knudsen cell.

2.4.1 Phase diagram

Fig.17 displays the phase diagrams for SiC, Si_3N_4, and Si.

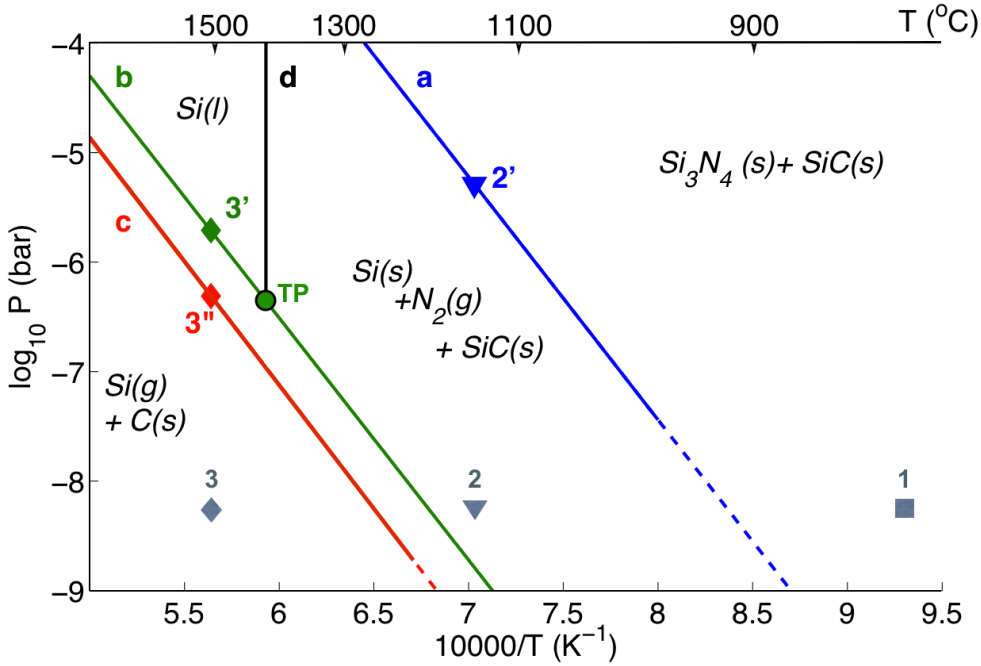

Figure 17. Phase diagram of the Si_3N_4 / SiC system. For curve (a), y-axis is the N_2 partial pressure. For (b) and (c), y-axis is the Si partial pressure. Plain lines are the referenced data, dashed are extrapolated, using Clausius-Clapeyron equation $ln(P) = \alpha/T + \beta$.
(a) Dissociation pressure of N_2 over Si_3N_4(s) [20, 21, 22]: $Si_3N_4(s) \Longleftrightarrow 3Si(s) + 2N_2(g)$.
(b) Saturation vapor pressure of silicon over its melt/solid for silicided graphite effusion cells [23, 24, 25]: $Si(s,l) \Longleftrightarrow Si(g)$. Although not noticeable, a slight change of slope occurs at the triple point (TP), due to the enthalpy of fusion of Si.
(c) Pressure of the saturated vapors of silicon over SiC [26, 27]: $SiC(s) \Longleftrightarrow Si(g) + C(s)$.
(d) Melting point of Si, at 1685K = 1412°C [20, 23, 24]: $Si(s) \Longleftrightarrow Si(l)$.
(TP) Triple point of Si. (1) Set-point for 800°C anneal at $\simeq 5e^{-9}$ bar. (2) Set-point for 1150°C anneal at $\simeq 5e^{-9}$ bar. (2') Equilibrium point for Si_3N_4 decomposition at 1150°C. (3) Set-point for 1450-1550°C graphitization at $\simeq 5e^{-9}$ bar. (3') Equilibrium point for Si vaporization at 1500°C. (3") Equilibrium point for SiC decomposition at 1500°C.

2.4.2 Literature and initial conditions

For this discussion, I will use the following terminology: for a variable X, the notation $\dot{X}$ stands for its first-order partial derivative over time, and $\ddot{X}$ for its second-order time derivative:

$$\dot{X} = \frac{\partial X}{\partial t} \; and \; \ddot{X} = \frac{\partial^2 X}{\partial t^2} \tag{2}$$

Now let's quantify the initial amount of silicon nitride. For stoichiometric Si_3N_4, an average 130 nm deposited on half of a 3.5×4.5 mm^2 sample represents an initial amount of *(mlc for molecules)*:

$$N_0 \; = \; \rho \mathcal{N}_A V/\mu \; = \; 1.4 \times 10^{16} \; mlc \tag{3}$$

where, for stoichiometric Si_3N_4, ρ is the density, μ the molar mass, $\mathcal{N}_A$ Avogadro number, and V is the PECVD-deposited volume, giving a count of $2N_0$ molecules of N_2 and $3N_0$ Si atoms.

Then we calculate the rates of escape. Every processed sample is placed in CCS growth conditions with a leak of diameter 1 mm and length 7 mm. The inside diameter of the crucible is 4.6 mm, and its length 10 mm. The rate at which gaseous species escape, in our case N_2 and Si, is [16]:

$$\dot{N}_{esc} = C \; \nu_{ave} \; \rho_{eq} \quad in \; mlc.s^{-1} \tag{4}$$

where $C \; = \; D^3/3L \; = \; 5 \times 10^{-8} m^2$ is the effective area of the leak, $\nu_{ave} \; = \; \sqrt{8k_BT/\pi m}$ the average thermal speed of a silicon atom or N_2 molecule in the vapor (k_B is the Boltzmann constant), and ρ_{eq} is the vapor density at equilibrium. Notice that a silicon atom and a nitrogen molecule have the same mass $m = 28u = 4.6 \times 10^{-26} kg$.

Assuming ideal gas behavior, ρ_{eq} can be written as a function of temperature and pressure at equilibrium:

$$\rho_{eq}(P,T) = \frac{N_{eq}}{V} = \frac{P_{eq}}{k_B.T} \quad for \; N_{eq} \; in \; mlc \tag{5}$$

The calculated temperature-pressure-dependent rate of escape of nitrogen molecules during the early decomposition of SiN, and then gaseous Si from decomposed SiN and sublimating

SiC (still assuming ideal gas):

$$\dot{N}_{esc}(P,T) = C\sqrt{\frac{8}{\pi\, m\, k_B}}\frac{P_{eq}}{T^{1/2}} = \frac{P_{eq}(Pa)}{T(K)^{1/2}}.10^{17}\ mlc.s^{-1} \tag{6}$$

Notice that this rate is identical for both Si(g) and N_2(g) because the masses of these molecules are equal.

2.4.3 Decomposition of silicon nitride

Now we focus on the temperature-pressure map Fig.17. The first step is the raising of the temperature from 810°C, cf Fig.17(1), to the annealing step at 1150°C, cf Fig.17(2). We start usually with P = 5-7 $\times$ 10^{-9} bar = 5-7 $\times$ 10^{-4} Pa. Decomposition of silicon nitride starts as we cross phase boundary Fig.17(a), cf Refs.[20, 21, 22]. As the pressure is imposed right before it happens, and 80% of that pressure is hence partially set by nitrogen, we will just choose a partial pressure of nitrogen P_{N_2} = 5$\times$ 10^{-4} Pa to start with. The corresponding temperature from the Clausius-Clapeyron equation is 1190K = 917°C.

We can assume that as the temperature rises we always stay right at equilibrium, infinitesimally below the curve, thanks to the Knudsen cell. The PID-controller parameters used for every annealing in this thesis have been set with no overshoot and a response time $t_{5\%} \approx 50$ s. An infrared temperature sensor closes the feedback loop. The typical temperature profile can be seen on Fig.18.

Then starting from Ref.[16], James Palmer has calculated that the time constant t_0 for the partial pressure of Si to settle in the graphite Knudsen cell is on the order of a few microseconds, cf Appendix C of his PhD thesis [107]:

$$t_0 = \frac{4V_{tot}}{\nu_{RMS}(A_{tot} - C)} \tag{7}$$

where V_{tot} is the internal volume of the crucible (4.6 mm diameter, 10 mm length), $\nu_{RMS} = \sqrt{3k_bT/m}$ the root mean square speed of a Si or N_2 molecule in the vapor, A_{tot} the internal surface area of the crucible, C the effective area of the leak. Hence, we obtain $t_{5\%} \gg t_0$, *the necessary and sufficient condition for equilibrium.*

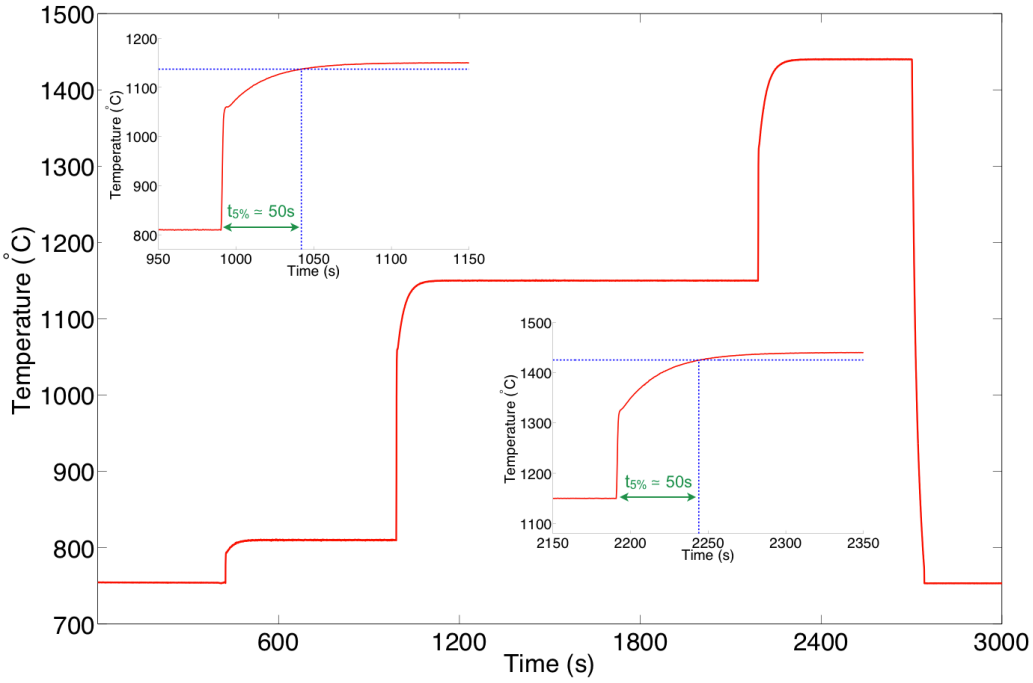

Figure 18. Temperature versus time during growth. Insets zoom on the transitions from 810°C to 1150°C and from 1150°C to 1440°C

Now, while we impose a raise of temperature from 800°C to 1150°C, we touch phase boundary Fig.17(a) at point (1190K, 5×10^{-4} Pa). Injecting this in Equation 12 gives $\dot{N}_{esc}(1190K) = 1.45 \times 10^{12}\ mlc.s^{-1}$. And over the course of approximately 50 seconds, temperature reaches 1150°C = 1423K. At this temperature, nitrogen outgases inside the Knudsen cell at an equilibrium partial pressure of 5×10^{-6} bar = 5×10^{-1} Pa, corresponding to point (2') on Fig.17. At these coordinates, the rate of escape of gaseous N_2 gains three orders of magnitude at $\dot{N}_{esc}(1423K) = 1.3 \times 10^{15}\ mlc.s^{-1}$.

At this point of the reasoning and as a remark, we can double-check James Palmer's calculation of the equilibrium condition. Using the ideal gas law, at point (1190K, 5×10^{-4} Pa), the amount of N_2 gas necessary to fill up the Knudsen graphite crucible is $N_{eq}(1190K) = P.V/k_b.T = 2.4 \times 10^{10}\ mlc$. This yields $t_{eq}(1190K) = N_{eq}(1190K)/\dot{N}_{esc}(1190K) \approx 10^{-2}s \ll 1s$. Similarly, at point (2') = (1423K, 5×10^{-1} Pa), $N_{eq}(1423K) = P.V/k_b.T = 2.0 \times 10^{13}\ mlc$, giving $t_{eq}(1423K) = N_{eq}(1423K)/\dot{N}_{esc}(1423K) \approx 10^{-2}s \ll 1s$. So again, in the case of Si_3N_4 decomposition as well as SiC, the establishment of pressure inside the

crucible is orders-of-magnitude faster than the PID-controlled temperature: *equilibrium is reached instantaneously*.

Now we would like to estimate the duration of the decomposition of the silicon nitride, named t_{max}, given its initial amount and the escape rates of nitrogen. We also have to take into account that, in the manner of rust protecting from rust, the solid Si produced from Si_3N_4 decomposition inhibits the reaction [108]. We will assume a fractional decomposition $\alpha = 10\%$ before the reaction stops [108]. This leaves us with an approximate maximum number of volatile Si atoms of:

$$N_{esc}^{max} = \alpha N_0^{Si} = 3\alpha N_0 \simeq 4.7 \times 10^{15}\ mlc \tag{8}$$

In this exercise, we will systematically assume first-order approximations. We already know that it takes the PID controller approximately 50 seconds to raise the temperature from 917°C (1190K), where $\dot{N}_{esc}(1190K) = 1.45 \times 10^{12}\ mlc.s^{-1}$ to 1150°C (1423K), where $\dot{N}_{esc}(1423K) = 1.3 \times 10^{15}\ mlc.s^{-1}$, cf Fig.18, linearly giving the time-independent $\ddot{N}_{esc}$:

$$\ddot{N}_{esc}(t) = \ddot{N}_{esc} = 2.6 \times 10^{13}\ mlc.s^{-2} \tag{9}$$

Before solving for t_{max}, we need to express a first-order approximation of $\dot{N}_{esc}$ as a function of time. We easily obtain, considering t = 0 at T = 1190K:

$$\dot{N}_{esc}(t) = \ddot{N}_{esc} \times t + \dot{N}_{esc}(1190K) \tag{10}$$

Now we can solve for t_{max}:

$$\int_0^{t_{max}} \dot{N}_{esc}(t)\, dt = N_{esc}^{max} \tag{11}$$

We obtain the following positive solution; the final approximation is possible because $\ddot{N}_{esc} N_{esc}^{max} \gg \dot{N}_{esc}^2(1190K)$:

$$t_{max} = \frac{-\dot{N}_{esc}(1190K) + \sqrt{\dot{N}_{esc}^2(1190K) + 2\ddot{N}_{esc} N_{esc}^{max}}}{\ddot{N}_{esc}} \simeq \sqrt{\frac{2N_{esc}^{max}}{\ddot{N}_{esc}}} \simeq 19s \tag{12}$$

This calculation provides quantitative estimations of escape rates of silicon vapor during the decomposition of silicon nitride as we raise the temperature to 1150°C. A similar methodology could be applied to silicon carbide during graphitization [107].

2.5 Main results and possible explanations

The main result of this study is that the presence of a silicon nitride mask evaporated on silicon carbide prior to graphitization enhances (Si-rich SiN mask) or reduces (N-rich) the number of layers grown compared to uncovered areas. Control samples, with no mask, have the same number of layers (within one layer) as the initially bare (IB) areas under the same growth conditions. Here we focus on the empiric understanding of the observed phenomena, using tools like X-ray photoelectron spectroscopy (XPS) and Raman to understand the mechanisms occurring at the interface between SiN and SiC in both Si-rich and N-rich cases. Now we investigate a little bit more, based on two spectroscopy experiments.

A possible explanation of Si-rich enhancement of the number of layers is that Si-rich SiN interacts with SiC at CCS temperatures and pressures. The XPS measurements of carbon-enrichment at the surface of sample Si7 is evidence for the formation of a modified SiC surface, as seen on Fig.19. In XPS, the probability to detect a photo-excited electron decays exponentially as we go deeper in the material. The inelastic mean free path (IMPF), named λ, is defined as the depth from which the probability of detection P(x) is $1/e \simeq 37\%$:

$$P(x) = \frac{I(x)}{I_0} = e^{-x/\lambda} \tag{13}$$

This interaction modifies the surface such that graphitization occurs more quickly in the initially masked (IM) regions after the Si-rich SiN mask has decomposed and remaining condensed Si has evaporated. It has already been shown that silicon-ion implantation modifies the SiC surface by damaging it (breaking of Si-C bonds), resulting in graphene formation at a lower temperature than pristine SiC [92]. Hence surface-modified SiC should graphitize at a higher rate at the same temperature. Modification of the surface could be due to the Si dangling bonds [109, 102, 103, 105] present in Si-rich silicon nitride. Si dangling bonds at SiN_3 sites have already been proposed as the dominant defects in Si-rich and stoichiometric PECVD silicon nitride, acting as amphoteric traps [104]. Moreover, in N-rich films, electron spin resonance (ESR) studies have shown that the density of these defects

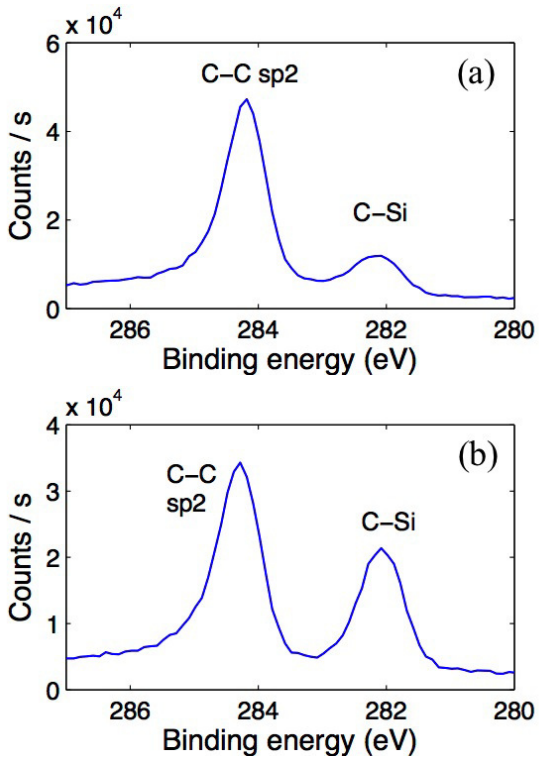

Figure 19. XPS of Si7, (a): IM part, C(1s) detection rate of 77%, (b): IB part, C(1s) at 66%.

is greatly reduced or even suppressed [106], making N-rich SiN a better dielectric than its Si-rich counterpart, as already mentioned in Section 2.3. Given an average of 2.8 extra layers of graphene for samples Si1-Si3 and Si5, one may estimate that the surface layer is modified to a depth of approximately 2 nm. Sample Si4, which was annealed at 1150°C for 20 extra minutes before graphitization, resulted in 4.5 extra layers, and an estimated depth of 3.5 nm for the surface-modified layer. These estimations are made assuming that 3 layers of SiC are required for growing 1 layer of epitaxial graphene [12], and for 4H-SiC one lattice constant c ≃ 10 Å contains 4 layers of SiC.

A possible interpretation of the reduction of the number of layers in the case of N-rich masks is simply that graphitization is delayed on the IM parts, starting only after SiN decomposition and evaporation of remaining condensed Si. This is consistent with XPS measurements of partially and fully processed N-rich samples, which had the same amount of surface nitrogen as control samples. In addition, when graphitization was stopped after

five minutes on sample N4, cf. Fig.20, Raman measurements matched pristine SiC in IM areas where the silicon from SiN decomposition had evaporated. Raman and ellipsometry measurements of N4 gave no evidence of graphene formation. So nitrogen might not react with the SiC surface at the temperatures and pressures present in the CSS chamber and delay of graphitization is the result.

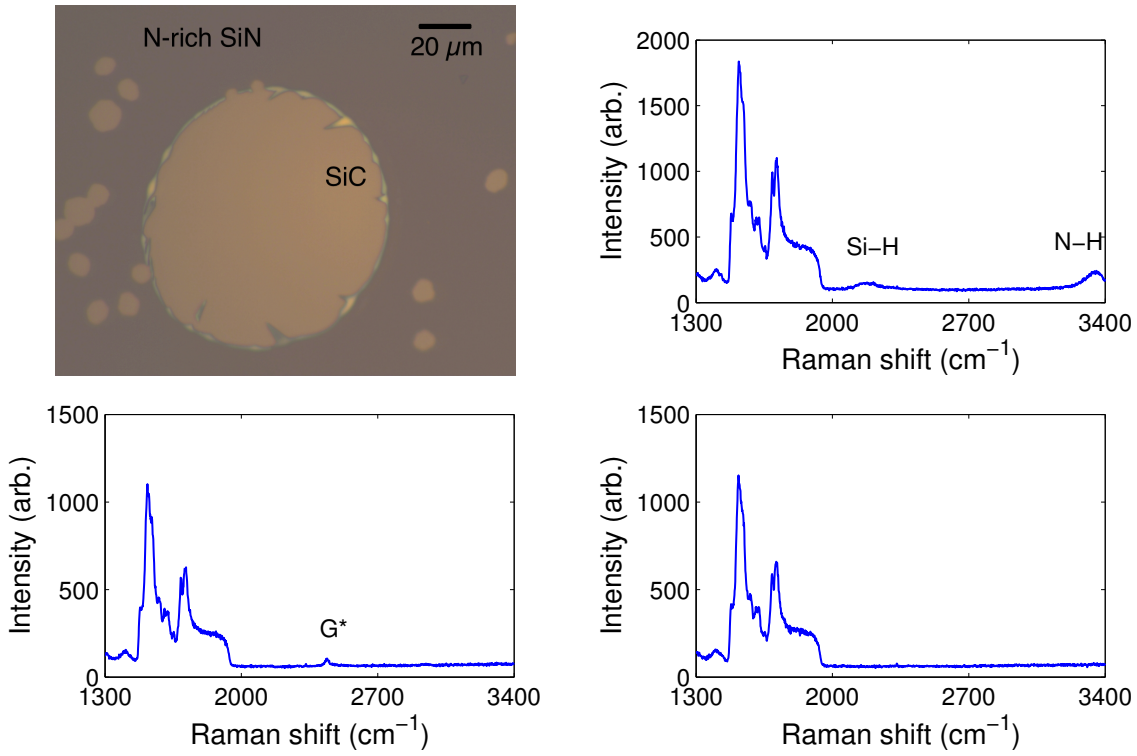

Figure 20. Micrograph and Raman spectra of N4. *(top left)* 50x optical micrograph of the covered part of N4 after one run at 1450°C for 5 minutes, showing areas where the N-rich SiN is entirely gone. *(top right)* Raman spectrum on the N-rich SiN, showing the Si-H / SiH_2 stretching modes and N-H stretching modes, respectively at 2200 and 3360 cm^{-1}. *(bottom left)* Raman spectrum on the SiC part of the covered half (cf. optical micrograph), showing the G* peak at 2450 cm^{-1}. *(bottom right)* Raman spectrum on the uncovered part, displaying pristine SiC.

As a remark, a very small G* peak at 2440 cm^{-1} appears, consistent with its identified presence in HOPG, as well as in single-wall and double-wall carbon nanotubes. It is attributed to a non-dispersive double-resonance Raman scattering mode [110]. However both D and 2d peaks are totally absent. It is not known why G* is present while no D, 2D or G peak can be observed, and except for this very slight difference the Raman spectra in the supposedly SiN-free circular areas are identical to the measurements made on the IB

half (bare SiC).

For the N-rich case it was first believed that the mechanisms involved were analogous to the Si-rich case depicted above. Nitrogen implanted silicon carbide exhibits an enhanced surface hardness [111], which would be consistent with its graphitization at higher temperatures, as more energy has to be brought to the system to break the bonds of the newly formed Si-C-N compounds. However Raman evidence (Fig.20) shows that the process involves this mechanism only slightly, or even not at all. Indeed sample N4 has been deposited N-rich SiN (Si / N = 0.70) on the top half. After one run at 1450°C for 5 minutes, it exhibits partial evaporation of the SiN, with circular areas where the SiN is even completely gone. On the Raman spectra Fig.20, no peak appears around 2200 cm^{-1}, characteristic of Si-H / SiH_2 stretching modes [95], and/or C-N sp^1 triple bonds [112, 113]. These peaks arise on the Raman spectra done on the SiN before graphitization, where in this case the wide peak around 2200 cm^{-1} is attributed to Si-H / SiH_2 stretching modes. Also N-H stretching modes [95] at 3360 cm^{-1} do not appear at all in these circular SiN-free areas of the IM surface, but can also be observed when the laser is focused on the N-rich SiN film covering the top half before graphitization. Hence, we believe that graphitization is just delayed on the IM part in this case. SiC sublimation starts on the IB half while SiN is still evaporating from the covered part. Once it is entirely gone, the IM part starts graphitizing, while the other half has already started. However, one unusual N-rich sample has shown less growth, 2-3 layers, under the IM part, but only after a second run in the CCS furnace. The first run reported no graphene growth, but still was hot and long enough for the entire N-rich SiN to be gone. Hence, a possible chemical interaction between the N-rich SiN and the SiC, leading to Si-C-N compounds forming at the SiN / SiC interface, might still be possible.

So far any definitive explanation concerning these processes is still premature, as further experimental evidence would be necessary to close the case on this curious romance between SiN and SiC.

2.6 Chapter conclusion

It has been shown that, by using a SiN vanishing mask evaporated onto SiC prior to graphitization, the number of graphene layers varies between masked and non-masked areas. Depending on its chemical composition (Si-rich or N-rich) the $Si_{3+x}N_4$ mask acts as an enhancer or inhibitor of graphene growth (of the order of +/- 3 graphene layers with the present growth conditions). Areas with and without few layer graphene can therefore be produced side by side during the heating process. The mask evaporates during graphene growth so that patterned, mask-free graphene layers are obtained directly in a single heating step.

This is a very simple yet potentially quite powerful method to obtain clean resist-free patterned graphene structures. In a further development, the process can in principle be integrated with carbon contacts deposited prior to graphitization [114] ; in a one step process graphene is grown where desired contacts are provided by the pre-deposited (thermally stable) carbon pads. This provides clean graphene, ready for transport measurements, with no further processing. Moreover the pre-defined growth location may help solve a long-standing problem of patchy growth for single layer areas on the C-face. For instance, using adjacent Si-rich and N-rich masked areas could allow to reach growth selectivity at the monolayer level. This is particularly important for quantum Hall effect metrology applications, which could benefit from large clean single layers on the C-face that has a much higher mobility [89] than the Si-face generally used.

CHAPTER 3

NANO SELECTIVE AREA GROWTH OF III-NITRIDES ON SAPPHIRE BY MOVPE FOR HIGH-QUALITY OPTOELECTRONICS [4, 5]

The doctorate program at Georgia Institute of Technology, halfway between Europe and the United States, has brought me into several labs and I have learned to use many pieces of equipment. At Georgia Tech Lorraine (GTL) in Metz, France, I have learned scanning electron microscopy (SEM), atomic force microscope (AFM), setting-up a Hall and electrical measurements lab, and even a few runs on Dr. Ougazzaden's T-shaped metal organic vapor phase epitaxy (MOVPE) reactor.

In Drs. Berger and de Heer's Epitaxial Graphene Laboratory, at the School of Physics in Atlanta, CCS graphene growth [16] and hydrogen etch furnaces, Raman spectroscopy, AFM, ellipsometry, magneto- and Hall resistance characterizations, or also the Physics NanoFab facility equipped with a JEOL JSM 5900 SEM for electron beam patterning to cite only a few. In parallel I have been using many tools at Georgia Institute of Technology's Institute of Electronics and Nanotechnology (IEN) cleanrooms, in particular the Oxford plasma-enhanced chemical vapor deposition (PECVD) for the SiN films, along with the Woollam M2000 ellipsometer to measure their composition. To finish this list the JEOL JBX 9300 FS electron-beam lithography (EBL) system (pictured in Fig.21) was actually one of the very first tools I have been trained on, back in 2010. It is capable of nanometric resolution, working at 50 to 100 kV, 0.05 to 100 nA (typically 100 kV and 1.8 nA) and providing 4 nm diameter Gaussian spot electron beam.

The main goal with the EBL machine is to produce nanometric patterns of 100-nanometer-thick glass (SiO_2) on III-nitride (III-N) wafers, with critical dimension from 80 to 120 nm which are then sent to GTL to perform growth of III-N in Dr Ougazzaden's T-shaped MOVPE reactor [115]. Typical growth temperatures range from 800 to 1000°C and the

Figure 21. The JEOL JBX-9300FS electron-beam lithography system in the Pettit cleanroom of Georgia Tech's IEN. I miss you so much... (photo: courtesy of Devin Brown, Georgia Tech IEN, formerly MiRC).

pressure is regulated at 100 Torr $\approx$ 13 000 Pa $\approx$ 0.13 bar. Nano selective area growth (nanoSAG) has been successfully completed on three different kinds of substrates:

- 3 μm gallium nitride on c-axis sapphire (430 μm), GaN / c-Al_2O_3, or simply referred to as GaN wafers.
- 200 nm thick aluminum nitride on 430 μm thick silicon (111), AlN / Si, or simply referred to as AlN wafers.
- 200 nm thick zinc oxide on c-axis sapphire (430 μm), ZnO / Al_2O_3, on top of which we grew 100 nm of GaN by MOVPE at GTL before e-beam lithography. The ZnO, of thickness 200 nm, was grown by Nanovation SARL using pulsed laser deposition (PLD) [116]. Simply referred as ZnO wafers.

Acting as the masking material, glass does not provide nucleation sites to the adsorpting atoms, and hence the crystal grows only in the apertures leading to the crystalline substrate. Two different processes are being studied right now. A key element is the method for producing patterned SiO_2. In the past our lab used to deposit glass on the whole substrate

by chemical vapor deposition, then patterned a mask with e-beam lithography, etch down the glass after development, and finish by removing the mask (a classical approach of processing). This had one disadvantage: the plasma etching is not perfectly selective to the substrate, and the whole glass needs to be removed in patterned areas. Hence, some of the nitride substrate is exposed to the plasma, and gets slightly damaged. I, along with Nicole Devlin and Devin Brown of Georgia Institute of Technology's then Microelectronics Research Center (MiRC), had a nice surprise with one of the e-beam resists: hydrogen silsesquioxane (HSQ, formula $H_8Si_8O_{12}$). This negative-tone resist cross-links into glass via exposure to electron beams (and even extreme UV), and its developer is tetramethylammonium hydroxide (TMAH), a harmless base for our substrates (and it even cleans the material). Moreover, it drastically reduces the amount of solvents used with conventional resists, making the process more environment-friendly. And cherry on top, this resist offers an excellent resolution of $\simeq 6$ nm (the best as far as I know). A crucial part of electron-beam lithography is proximity effect correction, whose role is to compensate for the scatterings of the electrons: detailed methodology for quantification of forward scattering and backscattering is available online [117]. Hence the whole conventional process has been replaced by a single-step recipe to obtain high-resolution patterns of glass, and leave GaN substrates unharmed, leading to higher quality grown crystals on this substrate.

Now concerning III-N materials, the Indium gallium nitride alloy (InGaN) has a tunable direct band gap ranging from 0.64 eV (InN) to 3.4 eV (GaN), illustrated on Fig.22 and has a high absorption coefficient making it ideal candidate for use in multijunction solar cells [118, 119, 120, 121, 122]. Although InGaN-based light emitting diodes have reached commercial maturity [86] and InGaN/GaN photovoltaic devices have been recently extensively developed, device performance tends to degrade when In content is high or the InGaN layer thickness increases [123, 124]. This has been attributed to the immiscibility gap of InGaN [125], the difficulty of incorporating In under compressive strain [126], and the large internal polarization field which significantly hinders carrier collection in PIN Ga-face devices

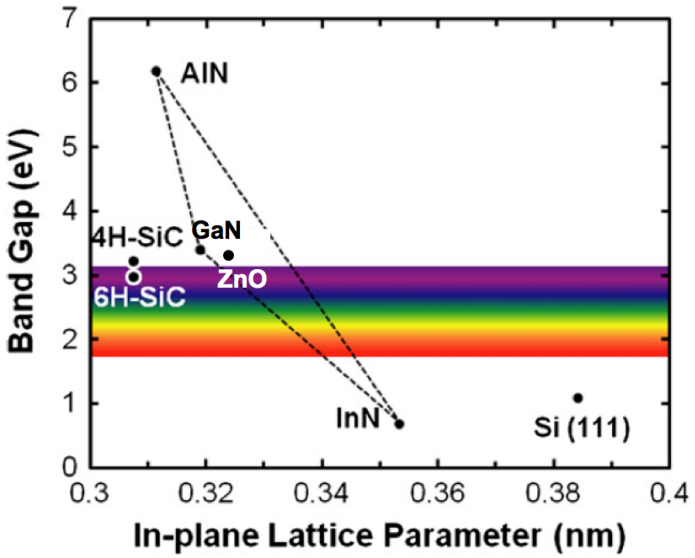

Figure 22. Bandgap versus in-plane lattice parameter for the materials studied in this thesis. *Made with data from Refs.[28, 29].*

[127]. Thus, planar heteroepitaxy of thick InGaN layers leads to poor morphology and inhomogeneous In content. The use of multi-quantum well architecture on free standing GaN substrates leads also to V-pits which emerge from threading dislocations at the surface of underlying GaN layers and extend to the surface of the InGaN layer. V-pits usually act as non-radiative recombination centers and leakage-current paths in III-nitride thin films, reducing solar cell performance [128]. It has been shown recently that these issues can be mitigated by periodically turning off the indium precursor flow, to insert thin GaN interlayers during InGaN growth [129, 130].

Another approach consists of the growth of InGaN nanostructures for the achievement of high-indium-content thick InGaN layers and InGaN/GaN PIN solar cells. This approach allows elimination of the preexisting dislocations in the underlying template [131, 132]. It also allows strain relaxation of InGaN layers, leading to higher In incorporation and reduced piezoelectric effect. Significant work has been reported on InGaN nanostructure fabrication. Among the different fabrication techniques that have been used, selective area growth (SAG) via patterned substrates enables precise control of the spacing and position of nanofeatures. For instance, Wang et al. [133] have developed a patterning technique

based on a self-organization process, while more recently, Song et al. [134] have used patterned SiO_2 masks on GaN/sapphire templates. Both authors have then used SAG into their patterned substrates to obtain InGaN nanostructures.

The first study concerns the creation of high quality thick indium gallium nitride (InGaN) nanostructures using nano selective area growth (nanoSAG) on gallium nitride (GaN) templates on c-axis sapphire. InGaN epilayers for solar cells must be of high quality. They should ideally be free of V-pits that originate from threading dislocations, but it is challenging to grow high quality thick InGaN epilayers. NanoSAG has resulted in nearly dislocation-free GaN nanostructures and is compatible with device growth on non-polar or semipolar GaN facets, which would also reduce polarization effects [135, 136]. Both of these advantages potentially result in high quality InGaN nanostructures. In the present study, 100 nm thick InGaN nanostructures were grown by nanoSAG on GaN templates using metal organic chemical vapor deposition (MOCVD).

3.1 Experiment details

Nano-patterned substrates were fabricated on n-doped 2 μm thick c-oriented GaN-on-sapphire template following a procedure described in Fig.23. First, a 100nm thick negative-tone resist (hydrogen silsesquioxane, HSQ) is spin-coated on the template. The resist is then patterned using a state-of-the-art JEOL JBX-9300FS electron-beam lithography system providing a 4nm Gaussian beam, that we used at 100 kV accelerating voltage, under a 1.9 nA current. The part of the resist exposed to electron beam cross-links into SiO_2. At last, TMAH 25% etching treatment is used to open the nano-patterns (nano-holes and nano-stripes). The diameter of the circular opening is 75-to-90 nm and the size of the stripe openings is 10 x 0.1 μm^2, cf Fig.24 with an orientation along the (110) direction.

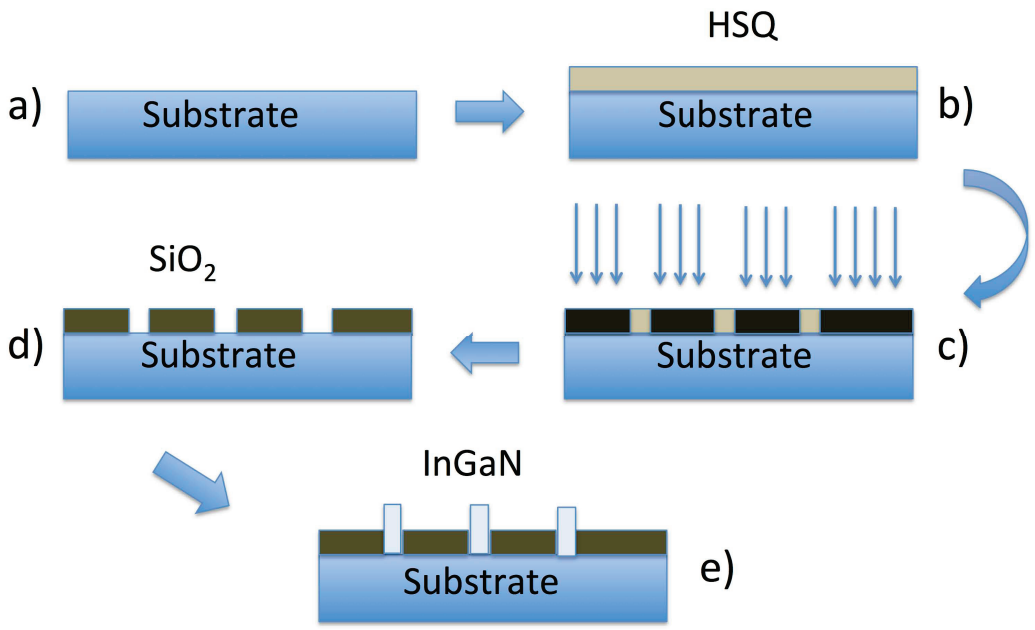

Figure 23. Scheme of the nano-patterning process used for the growth of InGaN nanostructures: a) n-GaN/c-sapphire substrate, b) HSQ resist spin coating, c) electron beam lithography allowing cross-linking of the resist into SiO_2, d) Development in TMAH 25% (base) to open the nano-patterns, e) MOVPE InGaN nano selective area growth.

This single-step process, compared to the standard deposit-pattern-etch method, allows better preservation of the quality of the substrate, first by not exposing the underlying GaN surface to a plasma etch, and then overall by simplifying the process and

hence limiting the number of chemicals used on the wafer. In particular it eliminates the need for environmentally-harmful solvents. At last, HSQ offers excellent resolution (≃ 6 nm, the smallest, to my knowledge). However, e-beam lithography is very expensive. Thick InGaN epilayers were then grown on these patterned templates using a T-shaped

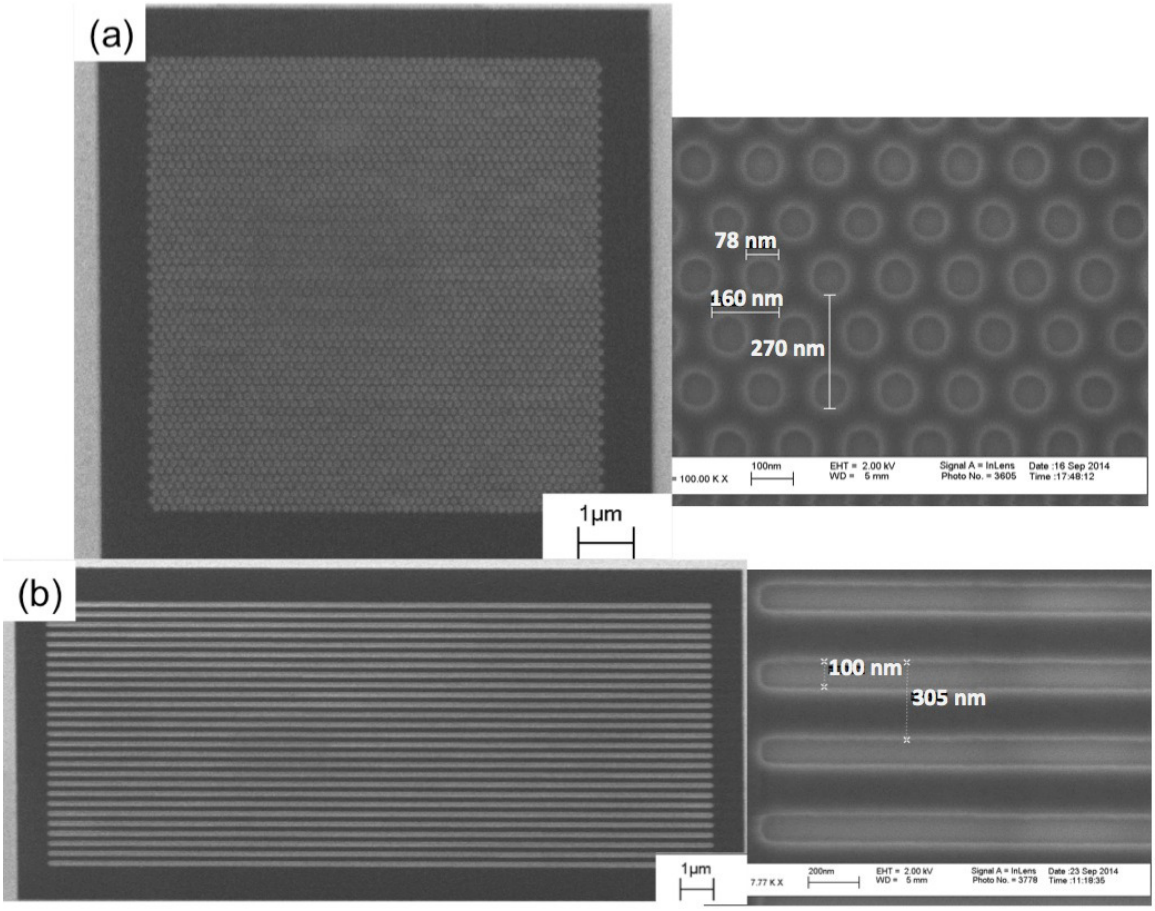

Figure 24. Scanning electron microscope images of nanopatterns of exposed HSQ on seed-GaN / c-Sapphire with (a) circular holes and (b) rectangular openings.

MOVPE reactor [115]. Trimethylindium (TMIn), trimethylgallium (TMG) and ammonia were used as the precursors for epitaxy. Growth temperature was 800°C under full nitrogen environment. The structural properties of the InGaN nanostructures were characterized using high-resolution and submicron-beam x-ray diffraction, and transmission

electron microscopy (TEM) along the (100) and (110) zone axes. Scanning electron microscope (SEM), cathodoluminescence (CL) and energy-dispersive X-ray spectroscopy mapping (EDX) were employed to assess the morphological properties and In composition of the nanostructures. After a calibration procedure using GaAs, InP, GaN, AlN, GaP and GaSb, as well as their ternary alloys (lattice-matched to InP, allowing the composition to be precisely determined through XRD), quantitative measurements of the indium composition from EDX were obtained from the intensity ratio of the Lα line of indium (3.290 keV) to the Kα line of gallium (9.770 keV). The K line of elementary nitrogen (0.392 keV) was also taken into account and revealed that the InGaN alloy is stoichiometric. The acquisition time for each EDX spectrum was 60 s, during which no drift in the position of the electron beam was observed. The error in the In composition determination is estimated to $\pm 1\%$ [137].

3.2 Structural and morphological characterizations

Fig.25 shows SEM images of perfectly selective InGaN nanostructures grown on circular and stripe-shaped openings in the patterned substrate, respectively. As a result of optimized growth conditions, InGaN growth on the patterned area is perfectively selective, without any polycrystalline deposits on the masks. The pattern with circular openings contains InGaN nanorods which display the shape of hexagonal pyramids. More than 3000 consecutive nanorods have been grown without any visible defect or polycrystalline deposit. It is clear that InGaN nanostripes show an elongated hexagonal pyramid shape. InGaN nanostructures exhibit well defined shape and size uniformity, exposing the six (1-102) triangular r-plane facets.

The InGaN nanorods have smooth facets whereas nanostripes show irregular triangular r-plane facet formation on the two elongated sidewalls. The other four small triangular planes are smooth as observed in the nanorods. This indicates that there is competition between InGaN growing in different orientations, which has different growth rates, and In incorporations. Even though there is some inhomogeneity in the sidewall morphology of InGaN stripes, both nanostructures are smooth which means that a 3D stress relief mechanism is in place. This mechanism mitigates strain-induced degradation, usually present in planar InGaN, which induces inclusions, V-pits, trench pits, In clustering and 3D growth as shown either in the unmasked area of the sample or control sample grown along with the patterned sample as revealed by the SEM image in the inset of Fig.26.

Fig.26 also shows the measured high resolution X-ray diffraction (HR-XRD) $2\theta-\omega$ scan and a simulated fit for the (002) reflection plane of the control sample grown along with the patterned sample. Both measurement and simulated fit are realized using a PANalytical X'Pert Pro HR-XRD. From the provided PANalytical simulation package, the average indium incorporation in the InGaN layer was found to be around 12%. The reciprocal space mapping (RSM) of the control sample which is also shown in the latter figure reveals two different InGaN diffraction spots. One is aligned exactly with the GaN peak (InGaN#1) and

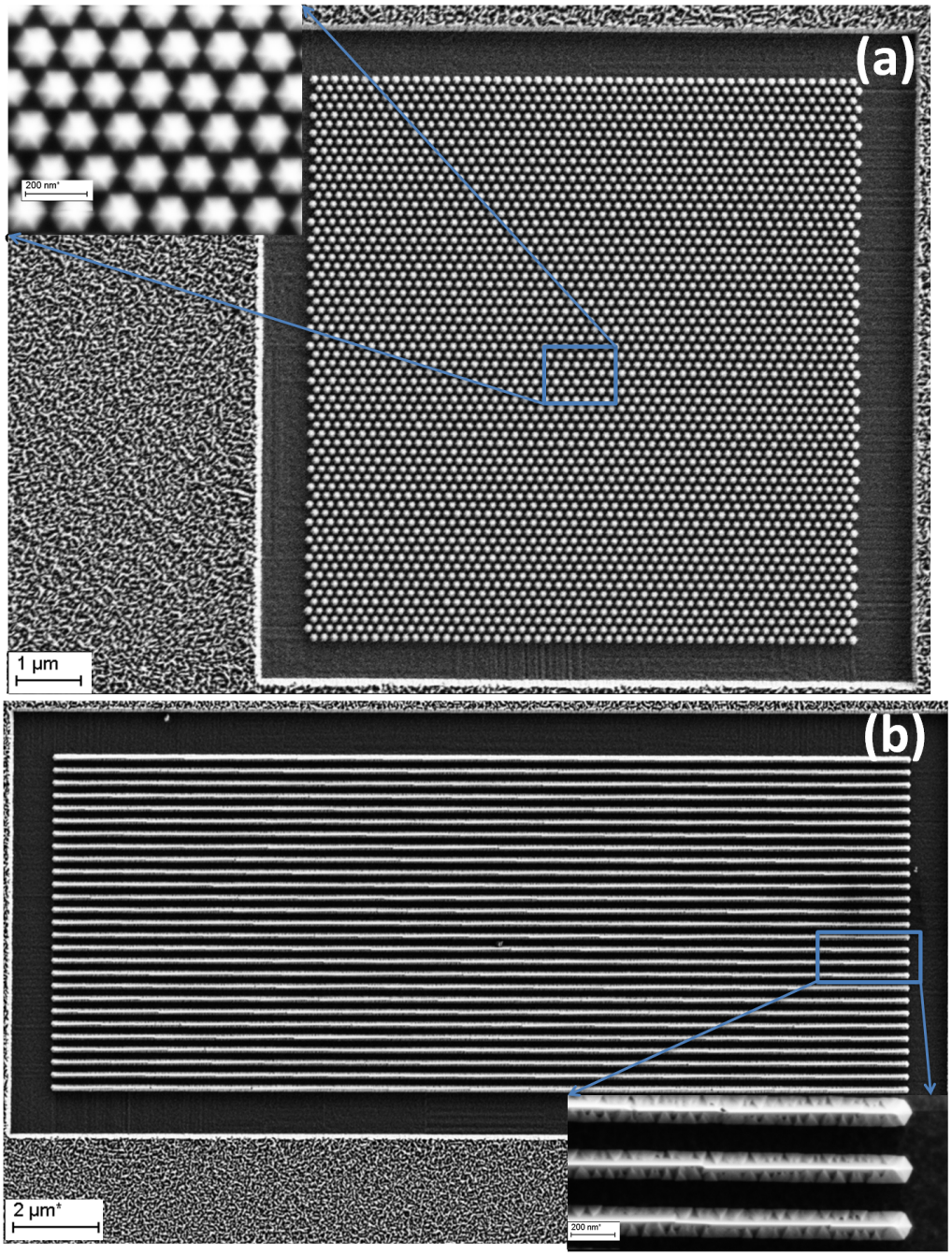

Figure 25. SEM images of perfectly selective thick InGaN nanostructure arrays grown on GaN templates in (a) circular opening and (b) stripe opening

corresponds to the pseudomorphically strained InGaN with 12% In content. Another weak intensity peak (InGaN#2) is completely off aligned from the GaN peak and corresponds to the relaxed InGaN layers with In content averaging around 23%. The appearance of the double diffraction peaks is due to phase separation and is a normal feature of thick InGaN

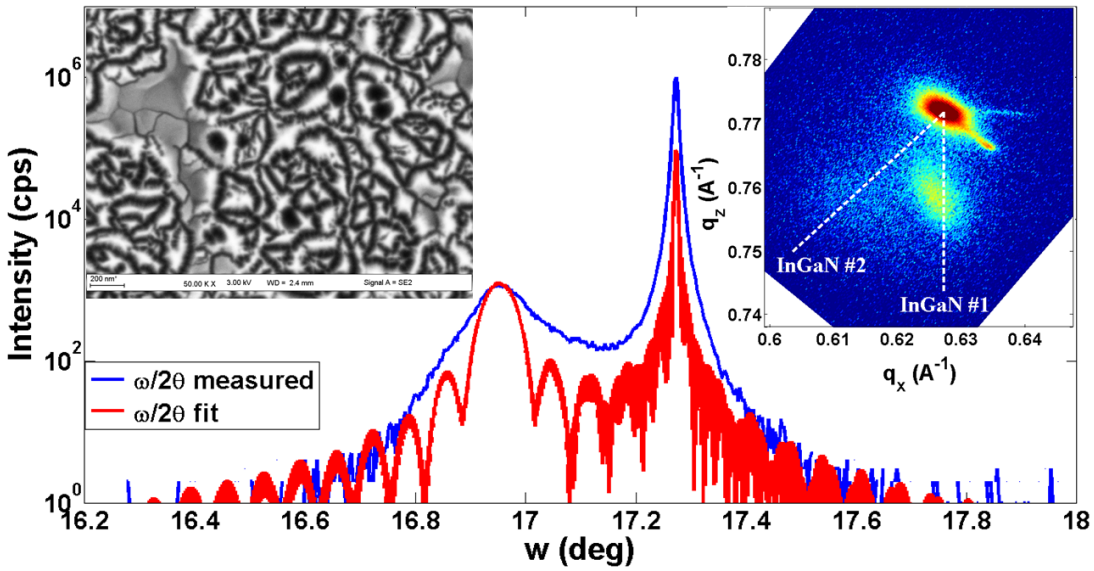

Figure 26. XRD $2\theta - \omega$ scans for 002-reflection planes of planar InGaN. The left and right insets show the SEM image of the surface and reciprocal space mapping (RSM) of planar InGaN, respectively. (courtesy of Xin Li, Georgia Tech Lorraine, abbrev. GTL, Metz, France)

samples as previously reported by several authors [138, 139, 140].

Fig.27 shows different magnifications of STEM images, taken with the high-angle annular dark-field detector (HAADF) of InGaN nanorods. STEM is performed at the Laboratoire de Photonique et de Nanostructures (LPN) of CNRS, Marcoussis, France. They correspond to the (100) plane of the GaN substrate, [100] axis being horizontal on Fig.25; we chose a [100] cut so that it connects two vertices of the base of each hexagonal nanopyramid. The very good uniformity of the hexagonal nanopyramids, the clear contrast between the 20-nanometer GaN regrowth layer and 150-nanometer-thick InGaN, and the absence of threading dislocation emerging from the interfaces in the nanorods are all apparent. Fig.27(e) shows $2\theta - \omega$ map of diffracted intensity collected simultaneously from the nanorods and planar InGaN at the (00.4) reflection using synchrotron-based XRD. Synchrotron-based XRD is performed at the Advanced Photon Source (APS) of Argonne National Laboratory, Illinois, USA. The signal width along the ω axis corresponds to mosaic spread, and the width of the nanorods signal is due to the variety of orientations among the nanorods. These results show clearly that the InGaN nanorod is single crystal with

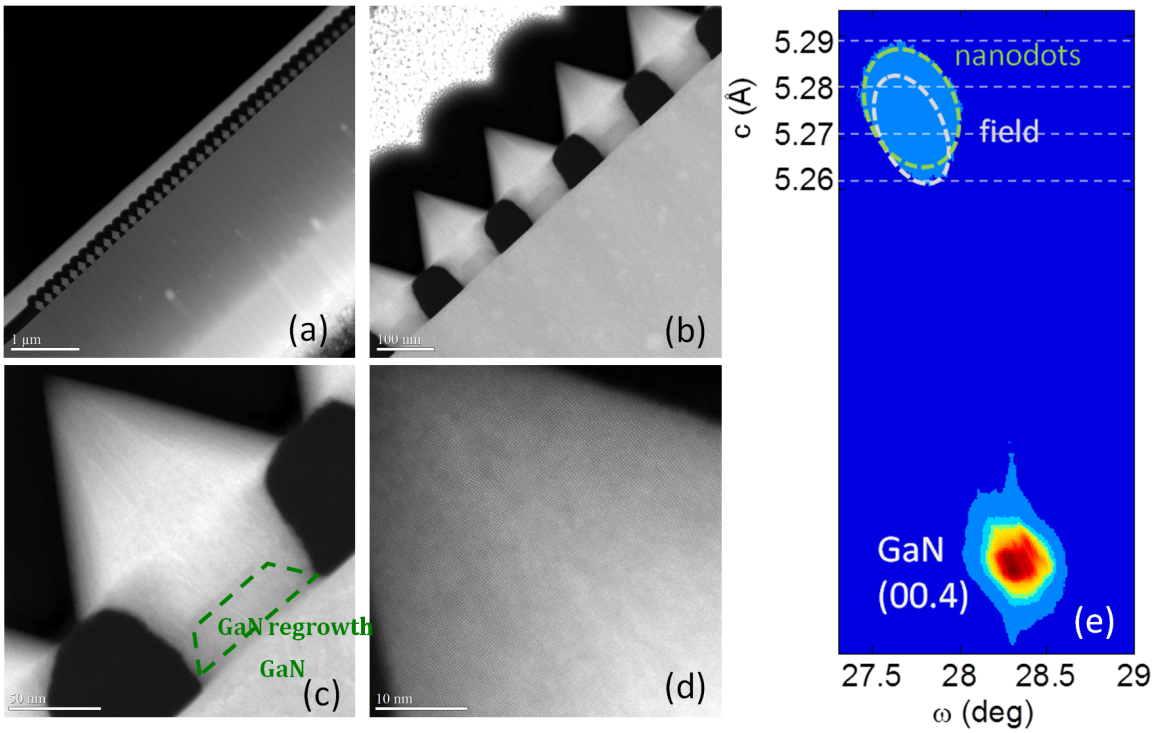

Figure 27. (a)-(d) Different magnifications of HAADF cross-sectional STEM images, (100) plane of GaN substrate, of InGaN nanorods (courtesy of Gilles Patriarche and Konstantinos Pantzas, LPN), (e) $2\theta - \omega$ map of diffracted intensity collected simultaneously from the nanorods and planar InGaN at the (00.4) reflection using synchrotron-based XRD (courtesy of Peter Bonanno, GTL and Zhonghou Cai, Advanced Photon Source, abbrev. APS, Argonne, Illinois, USA).

slightly misoriented grains, one being housed inside the SiO_2 mask and the other emerging out from the mask with hexagonal pyramid shape. According to data of Fig.27(e), the In content is slightly higher in the nanorods (around 22%) than in the field (around 21%), the field being the non-patterned area of the substrate (on top of which the InGaN grows as on a bulk substrate). The high-resolution TEM image of one nanorod shown in Fig.27(d) clearly evidences its defect-free epitaxy.

According to localized EDX measurements (see Fig.28), the nanorod exhibits rather good In content homogeneity along axes perpendicular to the c-axis (LG2 and LG3 lines with around 22% and 18 % of In content, respectively), with a corresponding gradient of In content along the c-axis (LG1 line, along which the In content varies from 16 % (apex of the nanorod) to 25 % (near the InGaN/GaN interface). These EDX profiles are in a very good agreement with data deduced from submicron-beam XRD analysis, and confirm that

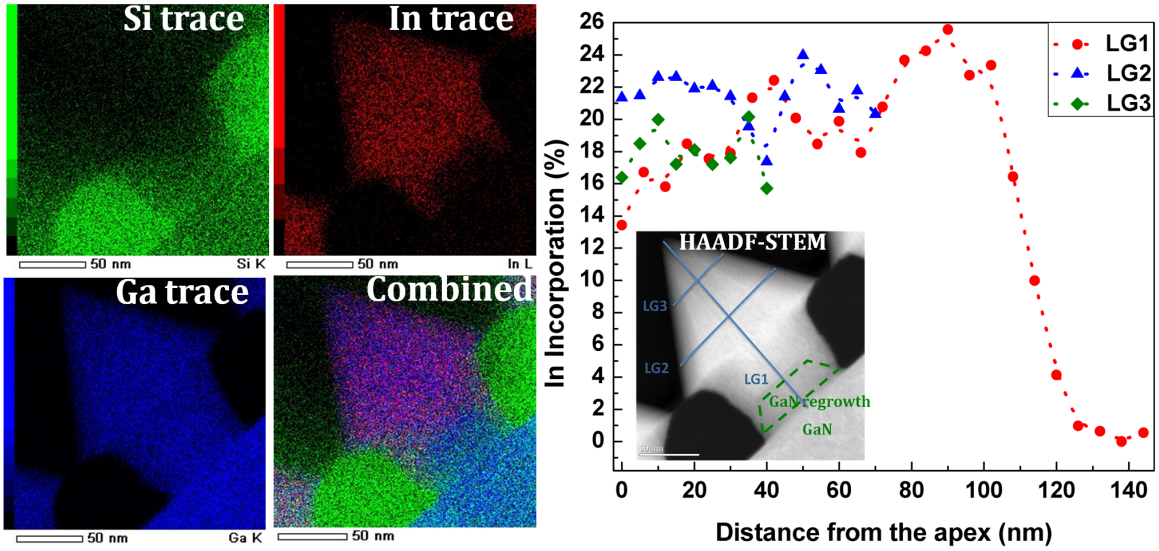

Figure 28. Left side: EDX mappings of Si, Ga, In and combined elemental trace in a single InGaN nanorod. Right side: EDX of In profiles along different directions in a single nanorod.

there is a sharp growth interface between GaN and InGaN layers. The regrowth of GaN and InGaN layers does not emerge from the SiO_2 patterns confirming that the growth is epitaxial with perfect selectivity.

Fig.29 shows both the STEM image of an InGaN nanostripe and CCD image of the diffracted intensity collected at the (00.4) reflection using synchrotron-based submicron-beam XRD. Fig.29(a) clearly shows a contrast difference between the GaN and InGaN layers. Along the c-axis of the InGaN layer, there are two regions with large contrast difference. The first region called InGaN1 has an In incorporation of around 13% and the second one, called InGaN2, an In content around 20% (both evaluated using localized EDX measurements). The InGaN1 sublayer starts to grow along the c-axis with semipolar r-plane facets and forms the core of the nanostripe. Then the InGaN2 sublayer grows on these semipolar r-plane surfaces. The latter growth, on semipolar r-plane surfaces, stops the growth of InGaN along the c-axis and forms an InGaN vein like with an In incorporation of around 6.5%. This figure also shows the boundary region with a slight disorientation between InGaN1 and InGaN2 sublayers. The growth on the semipolar facets is of importance and has advantages over the conventional c-axis growth since it allows reduction of

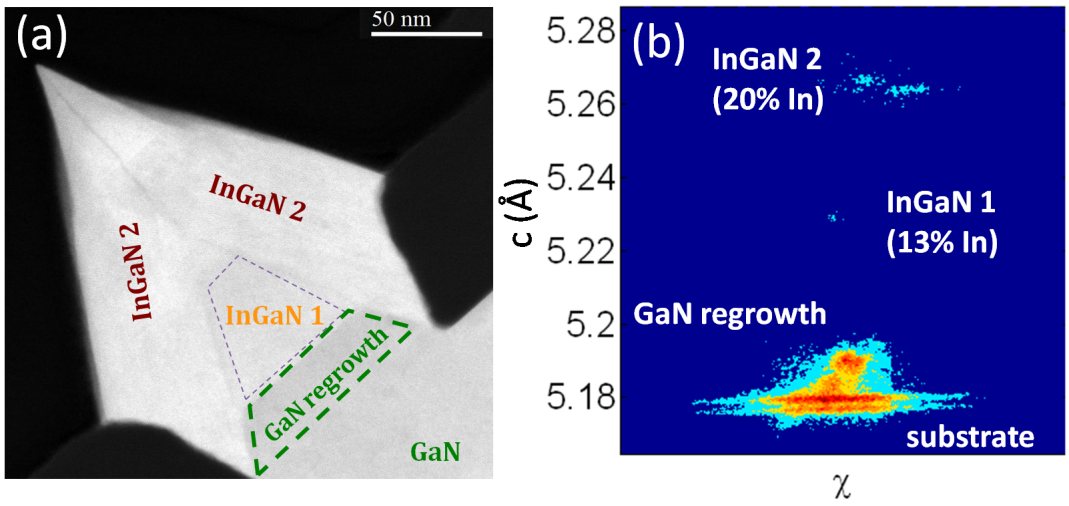

Figure 29. (a) Cross-sectional STEM image (courtesy of G. Patriarche and K. Pantzas, LPN) and (b) diffracted intensity collected at the (00.4) reflection using synchrotron-based submicron-beam XRD [30] of an InGaN nanostripe (courtesy of P. Bonanno, GTL and Z.-H Cai, APS). The angle χ corresponds to the orientation of the (00.1) planes around the length of the nanostripe.

the piezoelectric polarization effects which can play a detrimental role in the performance of solar cells based on InGaN material. The synchrotron submicron-beam XRD analysis on Fig.29(b) confirms the STEM results. The warmer colors correspond to higher intensity. Signals from five distinct grains are present: one from the GaN substrate, one from the GaN regrowth, one from the InGaN1 region, and two from the InGaN2 region. Indium content, calculated from diffraction data, is 13% and 20% for InGaN1 and InGaN2, respectively. These mole fractions are calculated using Schuster et al [141]: this method is based on Vegard's rule, the linear approximation linking the mole fraction (in our case the indium incorporation in the nitride film) and the relaxed lattice parameter of a crystal. These results are in very good agreement with data deduced from EDX measurements. Since the In incorporation rate is higher for growth directions along an axis perpendicular to r-planes than along the c-axis, such a difference of In content between the core (InGaN1) and the sidewalls (InGaN2) of the nanostripe is expected.

3.3 Optical characterizations

Fig.30 shows the low temperature (77K) electron beam energy dependence of cathodoluminescence (CL) spectra in planar InGaN, and single InGaN nanostripe and nanorod, respectively. At low beam energy (3 keV), the electron beam energy corresponds to a depth of maximum energy loss of 30 nm, and thus, the spectra reveal mainly the luminescence of the InGaN layer. In contrast to the single luminescence peak centered around 535

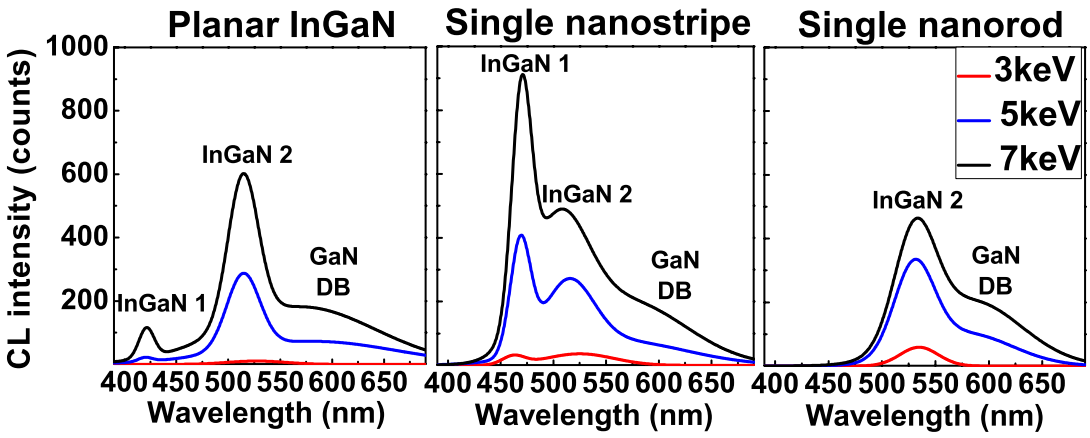

Figure 30. 77K, electron-beam energy dependence of cathodoluminescence (CL) spectra in planar InGaN, and single InGaN nanostripe and nanorod. DB stands for defect band.

nm obtained for the InGaN nanorod, both the InGaN nanostripe and planar InGaN exhibit two luminescence bands, centered at 464 nm and 525 nm for the nanostripe, and 420 nm and 520 nm for the planar InGaN. For the whole set of structures, we can also notice a broad luminescence band centered around 590 nm which is attributed to the GaN defect band. In the planar InGaN, the presence of the two luminescence bands can be attributed to the presence of strained InGaN1 and relaxed InGaN2 sublayers [130, 142], whereas the two luminescence bands observed in the nanostripe might be attributed to the fully relaxed InGaN1 and InGaN2 regions as shown in Fig.29. The determination of indium composition by cathodoluminescence (CL) in the different structures takes into account both the relaxation rate of the layer and the associated bandgap bowing parameter [31]. The experimental conditions of the CL measurements can be found in Refs.[130, 142]. Using data from Fig.30, the In content of the strained and fully relaxed sublayers of planar InGaN are

respectively 12% and 21%. These results are in good agreement with data deduced from high-resolution X-ray diffraction (XRD) $2\theta - \omega$ scan and RSM of the control sample (see Fig.26) discussed in Section 3.2. In the nanostripe, according to Fig.30, the In composition of the two relaxed layers are 14% and 21%, whereas in the nanorod only one relaxed InGaN phase with 22% of In is revealed. This is expected since, as shown in Fig.27, unlike the nanostripe which exhibits a structure with a core (InGaN1) and sidewalls (InGaN2), the nanorod is single crystal (InGaN2) with growth directions along axes perpendicular to r-planes. These results are in very good agreement with data deduced from both EDX and synchrotron submicron-beam XRD measurements. For the same growth condition the In incorporation in the nanorods is a little larger than in the nanostripes and almost twice as high as in planar InGaN. Increasing the electron beam energy leads to luminescence coming from deeper regions of the InGaN layer. In contrast to planar InGaN and nanostripe, the nanorod luminescence intensity tends (see Fig.30) to saturate with increasing electron beam energy. This indicates that the interaction plume becomes larger than the nanostructure.

Fig.31 shows InGaN planar, nanostripe, and nanorod electron beam energy dependence of the intensity and FWHM of the luminescence peak related to the highest In content InGaN2 layer. The nanorod exhibits the highest luminescence intensity, and, at low electron energy, the lowest luminescence peak FWHM. This could indicate that the InGaN alloy in the nanorod possesses a lower structural disorder and defect density, with the highest In incorporation, when compared to planar InGaN and nanostripe.

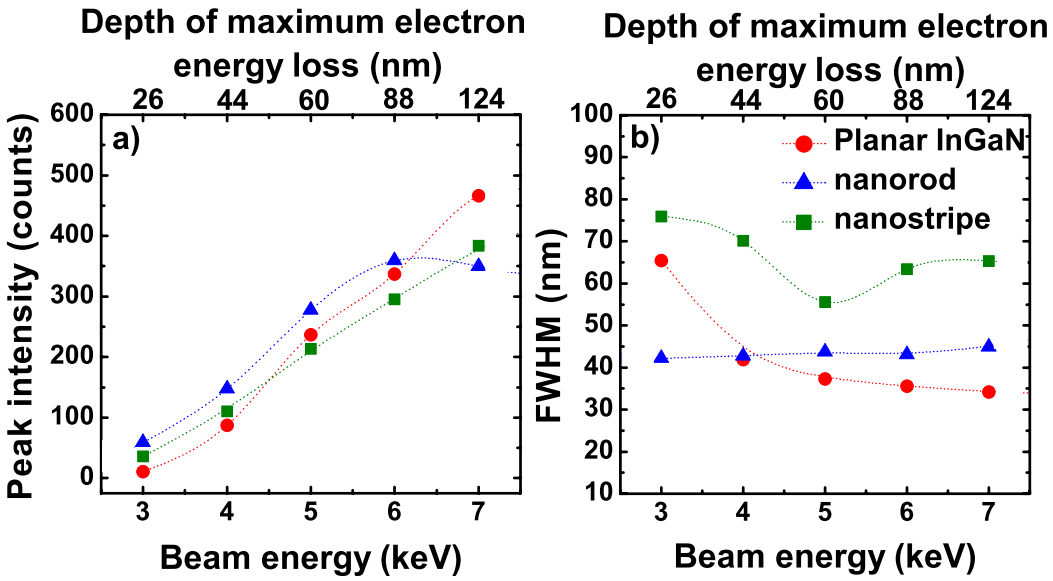

Figure 31. InGaN planar, nanostripe, and nanorod electron-beam energy dependence of the intensity and FWHM of the luminescence peak related to the highest In content InGaN2 layer.

3.4 Electrical behavior assessment

GaN doped with Mg is grown at 1000°C for laterally covering InGaN nanorods on n-GaN templates and study the I-V characteristics of the formed PIN heterojunction. The p-GaN grown under hydrogen ambient and high temperature entirely covers the thick InGaN nanostructures as shown in the inset of Fig.32. The hole concentration of the p-GaN layer is around 2 x 10^{17}cm^{-3}. The p- and n- regions were contacted with tungsten probes. For n-contact the SiO_2 mask in the patterned area was removed with buffered oxide etch (BOE, hydrofluoric acid). The I-V recorded in both planar and nanostructured areas reveal clear rectifying characteristics, as shown on Fig.32. These diodes have ideality factors around 4-5 comparable with others reported for InGaN core shell solar cells [143]. Almost a three-order-of-magnitude larger current is obtained in the case of the nanostructure-based PIN. Furthermore, the ratio of the currents measured at the voltages of +1V and -1V is more than 20 times larger. These results evidence the higher overall quality of the nanostructure-based PIN.

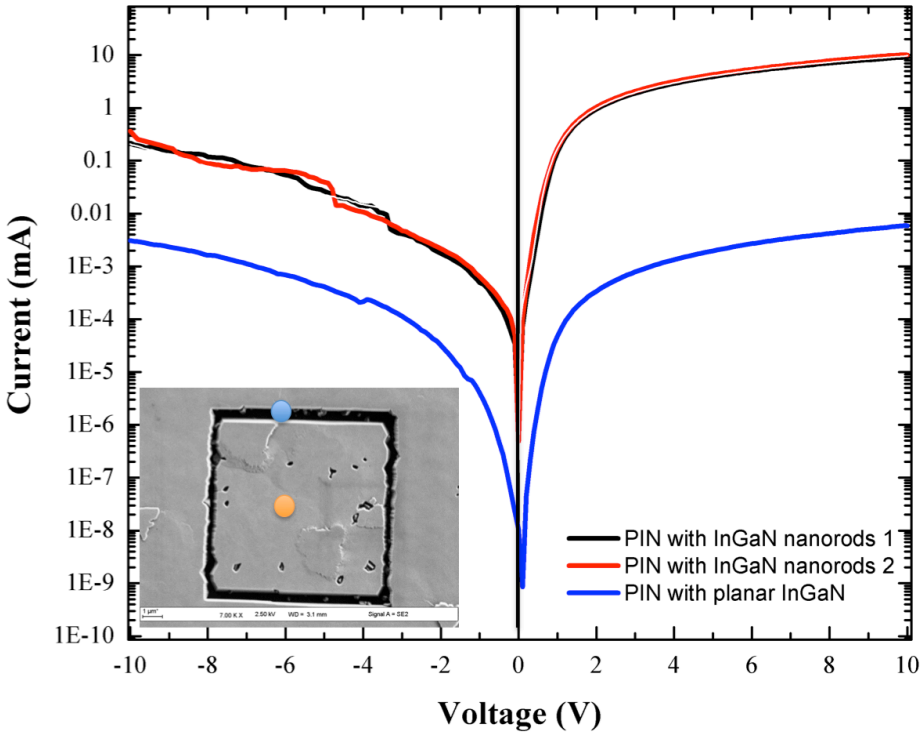

Figure 32. I-V characteristics of the PIN structure with embedded thick InGaN nanostructures on GaN templates, in comparison with planar InGaN PIN structure. Inset shows SEM image of the PIN structure in the patterned area. The blue and orange dots represent the point of contacts with respectively p- and n- areas after etching the sample with BOE.

3.5 Chapter conclusion

In conclusion, we have demonstrated the growth of single-phase, almost dislocation-free,150-nm-thick, and In-rich (up to 22%) InGaN nanorods and nanostripes on SiO_2 patterned c-oriented GaN templates. When compared to other work [133, 134], the patterning process of the substrate used in this study seems to greatly improve the structural quality of the nanostructures by allowing better wafer surface quality for nucleation. These nanostructures mitigate the propagation and generation of dislocations, as well as strain-related degradations and In clustering observed in planar InGaN. The nanoSAG of dense, In rich, and thick InGaN nanostructure arrays is a very promising approach for the realization of complete PIN structures with high-quality thick InGaN nanostructures embedded on it. It allows high In incorporation in thick layer, circumvention of the intrinsic problem

of defects in planar InGaN, and thus may provide significant enhancement on the conversion efficiency of InGaN-based solar cells. Moreover, our new process for production of nanometric-sized patterns of glass is both compatible with industry and environmentally friendly.

However, sapphire is an expensive substrate. Hence, the next chapter focuses on using the very same process to grow III-N crystals of similar quality on cheaper substrates.

CHAPTER 4

USING NANO SELECTIVE AREA GROWTH TO MAKE CHEAP HIGH-QUALITY OPTOELECTRONICS [6, 7]

4.1 NanoSAG of InGaN and GaN on AlN-buffered Si [6]

The tunability of the fundamental band gap of InGaN alloys, covering the whole visible spectrum, has proven to be highly suitable for realizing optoelectronic and photovoltaic devices [142]. However, even though multiple quantum well [128, 144] or multi-layered structures [130] architectures have been used to delay strain relaxation, the growth of thick high-quality InGaN layers (beyond 10% of In content) even on GaN templates remains challenging [142, 128]. Issues such as strong tendency to phase separation and relaxation of the layer due to lattice mismatch lead to In clusters and InGaN layers with large dislocation densities. These issues are of course even more pronounced in the case of the InGaN growth on silicon as shown by several authors who recently demonstrated the growth of InGaN layers (with up to 40% of In content) on AlN-buffered Si (111) substrates by PA-MBE and MOCVD techniques [145, 146, 147, 148]. Although InGaN films have been grown on AlN/Si, their crystalline quality is considerably low with large compositional and morphological non-uniformity. Thus, novel approaches have to be developed to improve the quality of thick and In-rich InGaN epilayers. One solution lies in the growth of InGaN nano-structures to accommodate the entire elastic strain without dislocations [149]. Significant work has been reported on self-assembled InGaN nanostructure over the entire composition range using HVPE; however, this process leads to random distribution of island sizes [132]. Albert et al. reported MBE growth of InGaN nanostructures on GaN-nanocolumns-buffered silicon substrates emitting from the ultraviolet (3.2 eV) to infrared (0.78 eV) and achieved an internal quantum efficiency of 36% for green emitting nanocolumns [150]. Using MOCVD, low indium containing InGaN nanostructures have been selectively grown only on GaN templates by pulsing the precursors [151, 134].

Recently, using continuous flow MOVCD on GaN template with an improved patterning process, the growth of thick, uniform, dense, single phase, $In_{0.22}Ga_{0.78}N$ nanorod arrays were demonstrated [4]. Even if GaN nanoselective area growth has been demonstrated by MOCVD on silicon substrates [136], to our knowledge high-quality thick In-rich InGaN nanostructures on silicon substrates have not been grown by MOCVD. There remains considerable difficulty in making high-quality, uniform, densely distributed, In-rich, and thick InGaN nanostructures with good selectivity using MOCVD.

In this section we report the nano-selective area growth (nanoSAG) by MOCVD, as well as detailed characterizations, of defect-free 100-nm thick InGaN nanopyramids with up to 30% of In content grown on patterned AlN/Si (111) substrate. The InGaN grown on these patterned templates exhibits high selectivity and the InGaN nanopyramids are homogeneously hexagonal in shape. Large indium composition inhomogeneity usually present in thick planar InGaN is absent in InGaN nanostructures due to more uniform elastic strain relaxation mechanism. Their single crystal structure is confirmed by scanning transmission electron microscope (STEM), which also reveals the absence of threading dislocations in the InGaN nanopyramids. Indium incorporation of around 30% is confirmed by cathodoluminescence measurements on a single InGaN nanopyramid. The good structural, morphological and optical quality of the InGaN nanostructures grown on Si indicates that nanoSAG technology is attractive for the realization of site-controlled indium-rich InGaN nanostructures-based devices and can also be transferred to other highly mismatched substrates.

Silicon (111) substrates were pre-coated with 200 nm polycrystalline AlN by physical vapor deposition. Then a 100 nm thick negative-tone resist (hydrogen silsesquioxane, HSQ) has been spin-coated. and patterned using electron-beam lithography, leaving an hydrogenated SiO_2 mask. Tetramethyl ammonium hydroxide (TMAH) has then been used as a developer to open nano-holes with diameter of 70-100 nm. The entire mask patterning process is described in Section 3.1 [4, 5]. 200-nm-thick GaN and InGaN nanostructures

were grown on the patterned templates in a T-shaped MOCVD reactor [115]. Trimethylgallium (TMG), Trimethylindium (TMIn), and ammonia (NH3) were used as the precursors for the growth under nitrogen ambient. The growth temperatures were 1000°C and 800°C for GaN and InGaN respectively. The structural and morphological properties of the nanostructures were studied using scanning electron microscope (SEM) and transmission electron microscopy (TEM). The optical properties of the nanostructures were studied using low temperature and depth resolved cathodoluminescence.

At first, 200 nm thick GaN was grown on patterned AlN/Si to optimize the growth process and have reference samples for comparison. Fig.33(a) shows the SEM image of the GaN nanopyramids grown on circular openings on the patterned AlN/Si substrate. High growth selectivity without any polycrystalline deposits on the masks is obtained. Fig.33(a) also clearly shows that each nanopyramid exhibits six smooth triangular sidewall semipolar facets corresponding to the (1-101) family of planes with good shape uniformity in the whole array. More than 99.6% of the nanopyramids are hexagonal and have six clearly identifiable triangular facets, this is similar to the uniformity of InGaN nanopyramids on GaN templates reported in Section 3 [4, 5]. Fig.33(b) shows the diameter distribution histogram of more than 3000 nanopyramids as extracted from SEM images. The average size of the GaN nanopyramids, corresponding to the length measured between the two opposite m-plane facets, is found to be 110 nm. More than 90% of the nanopyramids have sizes in the 110 ± 10 nm range. The excellent morphological quality of the nanopyramids may result from the soft plasma-free processing of the mask, preserving the quality of nucleation sites. Fig.33(c) shows a bright field scanning transmission electron microscope (STEM) image of a single GaN nanopyramid grown on an AlN/Si template. It clearly shows that the 200-nm thick AlN buffer is polycrystalline with a columnar growth morphology containing dark veins (red arrows) corresponding to grain boundaries. The STEM image displays the monocrystallinity of the 200-nm thick GaN nanopyramid on AlN/Si even though it has grown on multiple AlN nanocolumns with grain boundaries in between them. The GaN

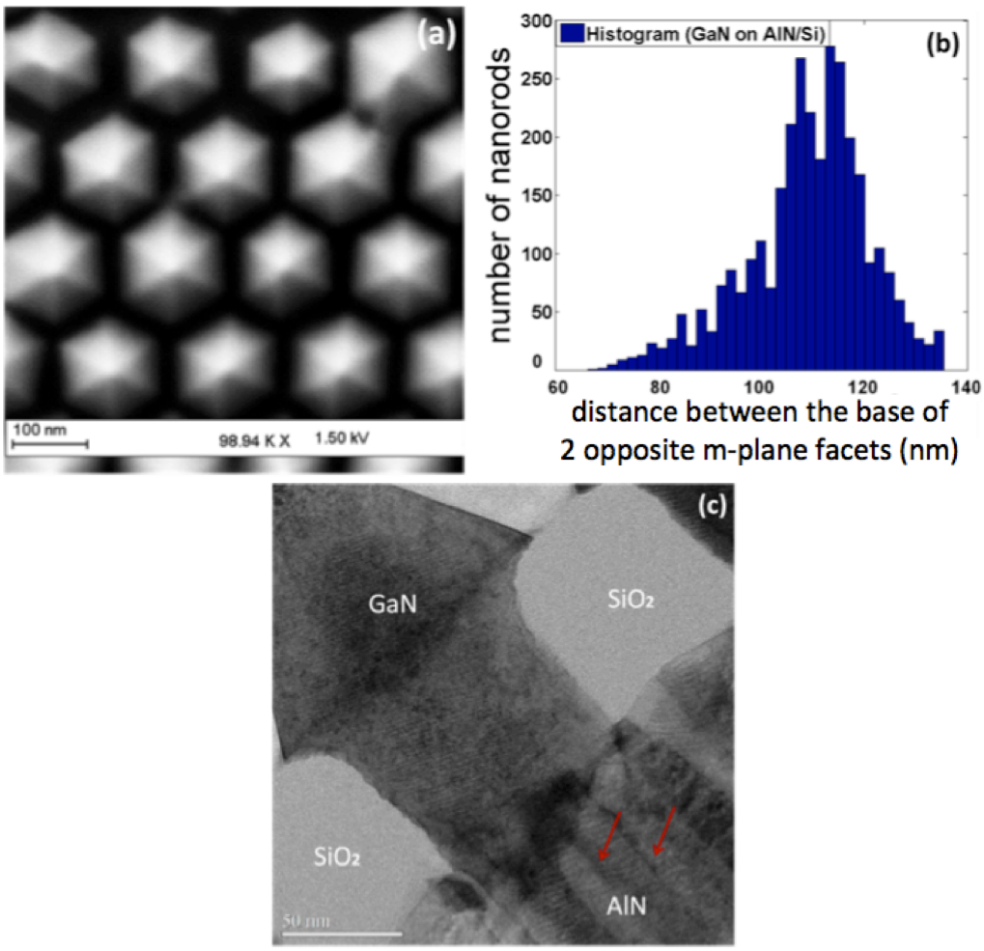

Figure 33. (a) SEM image of the GaN nanopyramids grown on circular openings on the patterned AlN/Si substrate, (b) Size distribution histogram of the GaN nanopyramid arrays as extracted from the SEM images (c) Cross-sectional STEM images of a single GaN nanopyramid grown on patterned AlN/Si templates. (courtesy of G. Patriache and K. Pantzas, LPN)

nanopyramids are also dislocation free. In some of them, the dislocations emerging from the interfaces are bent parallel to the base of the nanopyramid, preventing their propagation. After the successful growth of GaN nanostructures, InGaN nanostructures realization has been studied by growing 100-nm thick InGaN on the same patterned AlN-covered Si.

For later comparison, the structural and morphological characteristics of planar InGaN (outside of the patterned area) have been first studied. Fig.34 shows the corresponding high-resolution XRD 2θ-ω scan with a simulated fit for the (002) reflection plane, reciprocal space map for asymmetric (114) peak, and SEM image of the InGaN surface. The XRD 2θ-ω scan shows three distinct peaks that can be attributed to AlN (002) buffer layer, GaN

(0002) template, and InGaN (002) layer plane reflections. From the simulation, the average indium incorporation in the InGaN layer is found to be around 28%. The reciprocal space map (RSM) of the control sample reveals a bright InGaN diffraction spot and indicates that the InGaN layer is fully relaxed on the AlN seed layer. As expected, the planar InGaN exhibits 3D growth with V-pits and trench defects resulting in rough morphological quality as revealed by the SEM image in left inset of Fig.34.

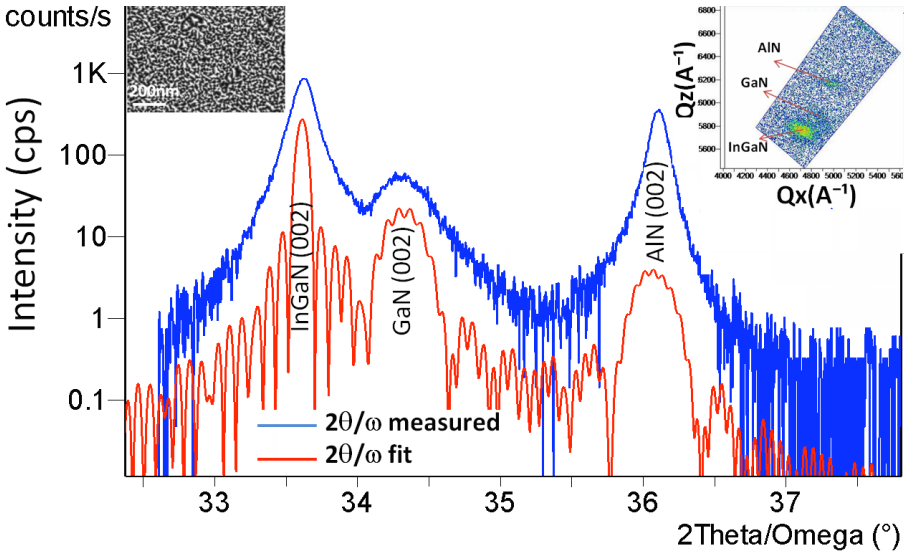

Figure 34. Measured high-resolution XRD 2θ-ω scan with a simulated fit for the (002) reflection plane of planar InGaN grown on AlN/Si template. Insets show the respective reciprocal space map (right side) and the SEM image of the InGaN surface in the field (left side). (courtesy of Xin Li, GTL)

Fig.35(a) and (b) show SEM images, obtained at different magnifications, of InGaN nanostructures grown on the circular openings of the AlN/Si template patterned area. Similar to the GaN nanopyramids grown on AlN/Si, (see Fig.33), InGaN nanopyramids also clearly shows six smooth sidewall semipolar facets with perfect selectivity on the whole 10x10 μm^2 patterned area without any polycrystalline deposits. The results are very similar to the InGaN nanopyramids grown on GaN / c-Sapphire [4, 5]. The statistical analysis of the SEM image of Fig.35(a) shows that 91% of the InGaN nanopyramids grown on the AlN/Si template have a perfectly hexagonal shape with clear facets. It is to be noticed that the GaN and InGaN nanopyramids grown on Si template have almost the same shape uniformity. The size distribution histogram of the InGaN nanopyramids grown on

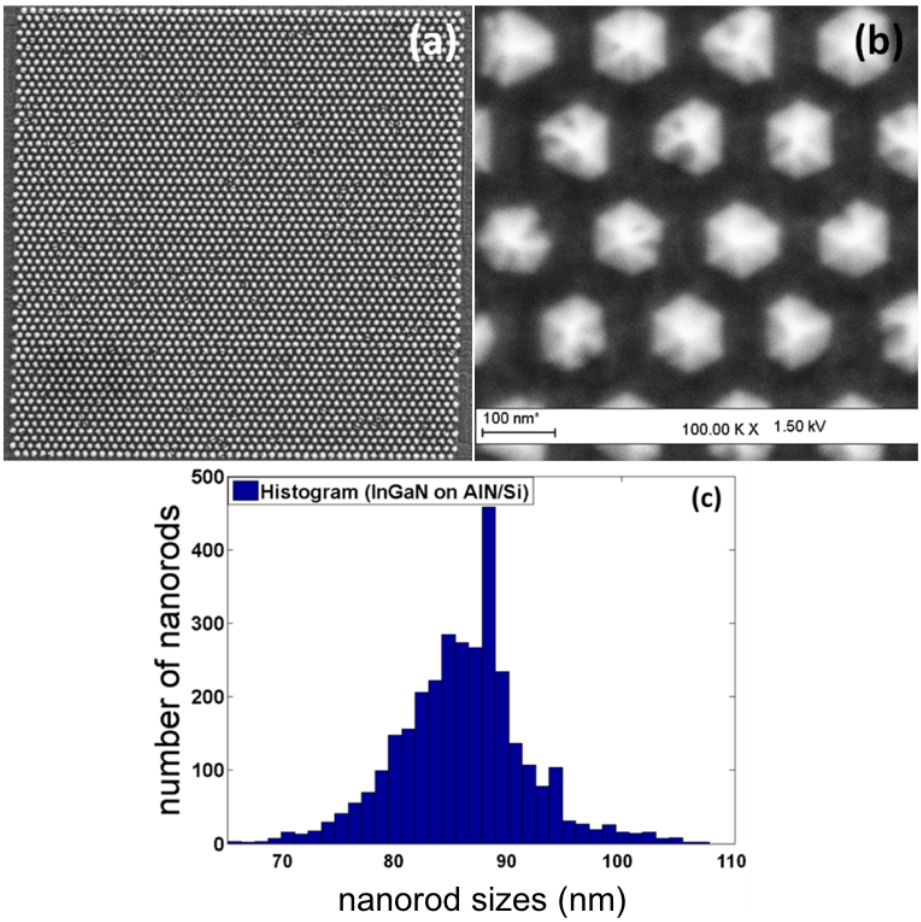

Figure 35. (a) SEM image of the InGaN nanopyramids grown on the patterned AlN/Si template. The patterned area measures 10 x 10 μm^2. (b) Higher magnification SEM image of the InGaN nanopyramids. (c) Size distribution histogram of the InGaN nanopyramid grown on AlN/Si (111).

AlN/Si(111), as deduced from the SEM image of Fig.35(a), is shown in Fig.35(c). The average size of the InGaN nanopyramids, corresponding to the length measured between the bases of two opposite m-plane facets, referred to as their "size" in Fig.35(c), is found to be around 86 nm and more than 90% of the nanopyramids falls in the size 86 ± 7 nm range. There is no considerable difference between the size of the GaN and InGaN nanopyramids grown on Si even though the height of the GaN nanopyramids is almost twice that of the InGaN nanopyramids. This is expected since under these growth conditions, lateral growth rate is low leading to lower size variation with height.

To investigate the structural quality of the InGaN nanopyramids, cross-sectional STEM studies were carried out. Fig.36 displays STEM images of planar InGaN in the field in window (a) in comparison with InGaN nanopyramids grown on SiO_2-masked AlN/Si in

windows (b) to (e). The planar InGaN surface is completely 3D with huge networks of V-

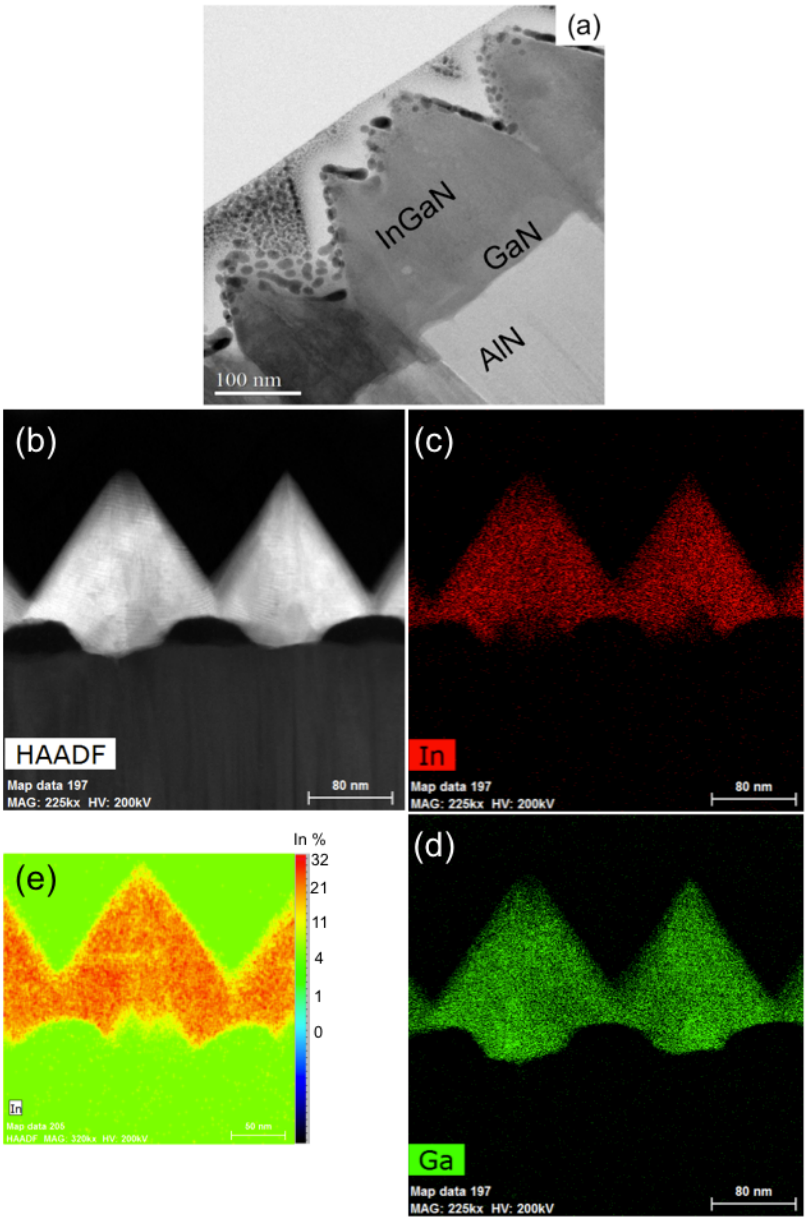

Figure 36. Cross-sectional STEM images of: (a) InGaN field; (b)-(e) InGaN nanopyramids grown on AlN/Si templates, where (b) is the picture through the HAADF detector, (c) energy dispersive X-ray (EDX) spectroscopy trace for indium, (d) for gallium, (e) the quantified EDX indium map. (courtesy of G. Patriache and K. Pantzas, LPN)

pits originating from the threading dislocations propagating from the polycrystalline AlN buffer layer. In comparison with the field, Fig.36 confirms that the InGaN nanopyramids on AlN/Si templates are monocrystalline and dislocation free. The InGaN nanopyramids are uniformly hexagonal. The angle of the semipolar planes in the top portion of both the

GaN and InGaN nanopyramids on AlN/Si templates are tilted when compared to the angles in InGaN nanopyramids in GaN templates reported in Section 3 [4, 5].

Fig.37 complements Fig.36 with EDX line scans parallel and perpendicular to c-axis on a single InGaN nanopyramid, revealing very nice homogeneity of In incorporation. Indium

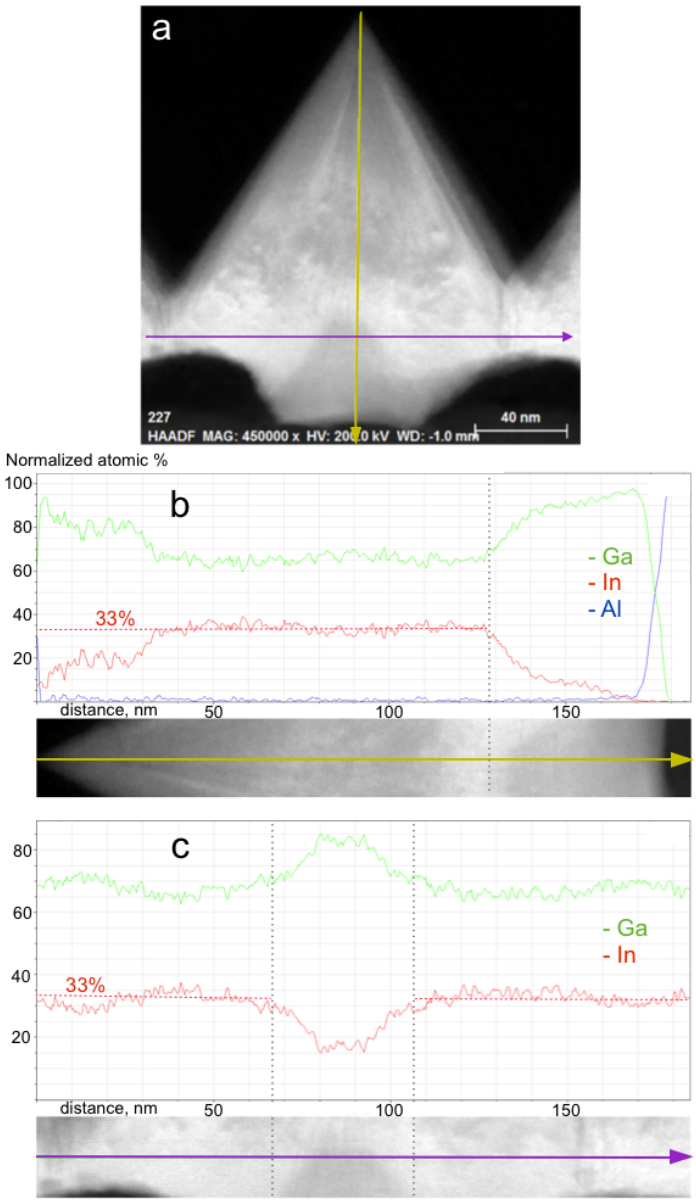

Figure 37. EDX line scans of a single InGaN nanopyramid of with indium content of 33%: (a) High-angle annular dark-field (HAADF) STEM image and definition of the lines for the EDX scan; (b) c-axis scan; (c) in-plane scan. (courtesy of G. Patriache and K. Pantzas, LPN)

of course drops when we penetrate the 20 nanometers of GaN grown at the beginning of the MOVPE, cf Fig.37(b)-(c). However, the gradual drop in Indium content as we approach

the last 30 nm of the apex of the nanopyramids, moving from right to left on Fig.37(b), is not explained as of today and will be subject to further investigation.

Fig.38 shows the EDX line scan for indium and gallium atomic concentrations recorded along the three consecutive nanopyramids which vividly shows that all the three nanopyramids have similar indium incorporation averaging around 33% demonstrating the ability of NSAG to obtain very uniform and homogenous InGaN nanostructures. The quality of

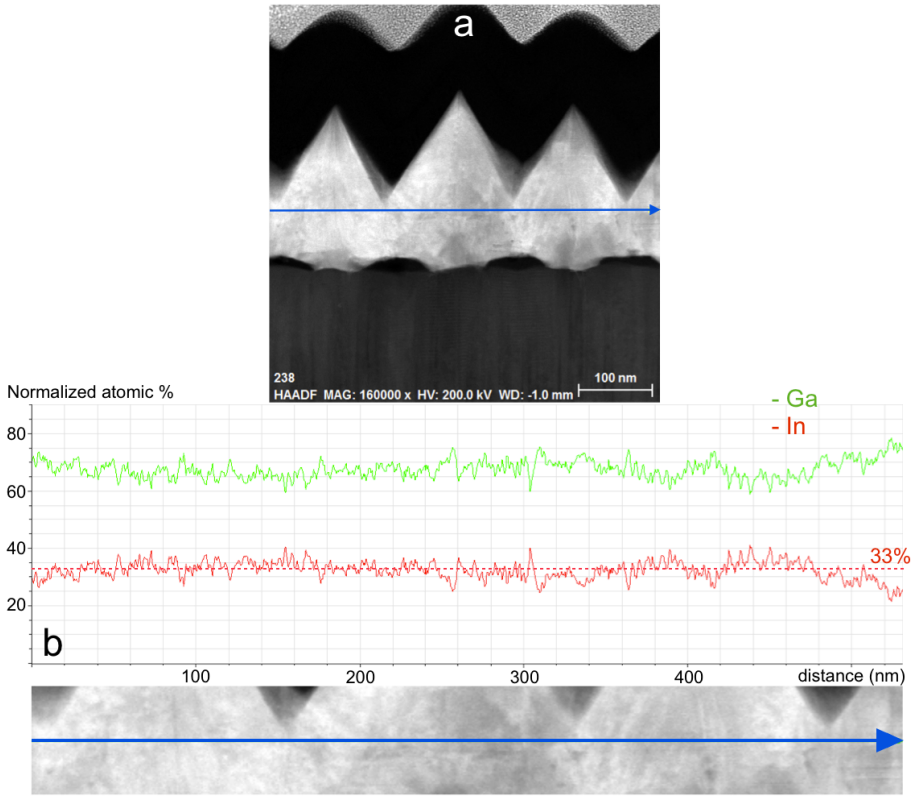

Figure 38. (a) STEM image and (b) EDX line scan for three consecutive coalesced InGaN nanopyramids with uniform indium content averaging around 33% as indicated by the red dashed line. (courtesy of G. Patriache and K. Pantzas, LPN)

the seed layer, which has multiple orientations, grains and grain boundaries with voids in between them, might induce this tilt or twist in the nanostructures. Even though the quality of the AlN-nanocolumns seed layer is low, the InGaN nanopyramids grow with only a small tilt or twist, they neither lose their single crystalline nature nor generate more defects or misfit dislocations. This indicates that thick, uniform and densely distributed single crystalline InGaN nanostructures can be grown on silicon using MOCVD.

Cathodoluminescence (CL) spectroscopy was used to study the emission characteristics of a single InGaN nanopyramid. Fig.39 shows low temperature (77K) CL emission spectra from a single InGaN nanopyramid and the inset shows the CL spectra from planar InGaN in the field. At these low beam energy (3-7 keV), the electron beam energy corresponds to a depth of maximum energy loss varying in the range 25-60 nm, and thus, the spectra reveal mainly the luminescence of the 100-nm-thick InGaN layer. Both the InGaN nanopyramid and planar InGaN exhibit two luminescence bands, centered at 614 nm and 667 nm for the nanopyramid, and 562 nm and 700 nm for the planar InGaN. In the planar InGaN, the

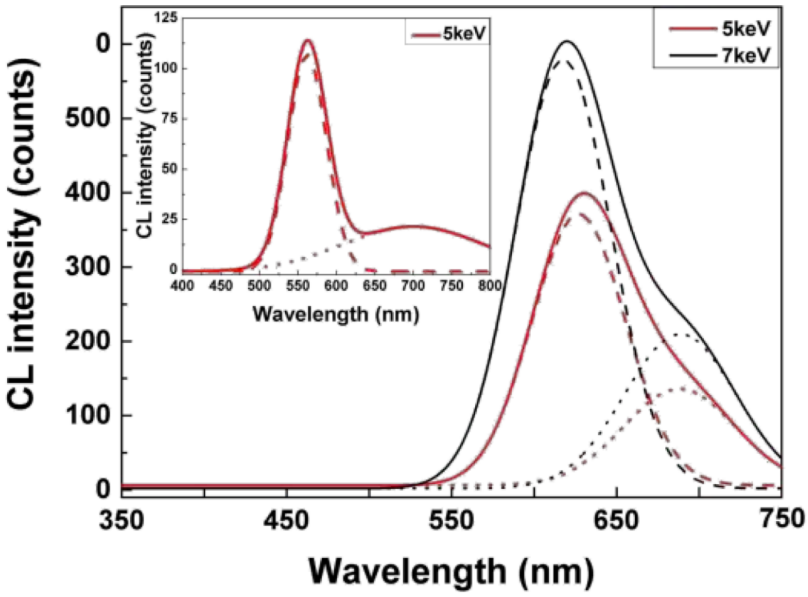

Figure 39. Low temperature (77K) CL emission spectra from a single InGaN nanorod. Inset shows the CL spectra from the InGaN field.

low wavelength peak can be attributed to the near band edge emission of InGaN with an In content equal to 25%. In composition is determined according to the work of Orsal et al. [31] taking into account both the relaxation rate of the layer and the associated bandgap bowing parameter. The other luminescence band spanning from 550 nm to 750 nm originates probably from the localization of excitons at potential minima in the In-rich InGaN areas confirming the expected In content fluctuations in planar InGaN. In the nanopyramid, the peak at 625 nm corresponds to an In content of 30%. A second weaker peak at 680

nm reveals the presence of InGaN at 33.5% of indium. As a remark, when we increase the electron-beam energy (going deeper in the material), the ratio between the low- and high-wavelength peak intensities increases: this is indicative of a nanopyramid structure comprising a core (growth direction along c-axis) with an In content around 30%, and sidewalls with triangular semipolar facets (growth direction perpendicular to the triangular facets) facilitating more indium incorporation, here 33.5%. Thus, using the same growth conditions, more indium is incorporated in the nanopyramids, compared with the InGaN in the field.

In this section, we have demonstrated nano-selective area growth of GaN and InGaN nanopyramids on AlN /Si(111) using MOCVD. This approach yields perfectly selective nanopyramids on silicon substrates. The nanopyramids are single crystalline and dislocation-free. In addition, nanopyramids are highly uniform and comparable to nanostructures grown on GaN templates. CL emission spectra analysis confirms enhancement of indium incorporation in the nanostructures. Up to 33% In-content homogeneously distributed InGaN have been obtained. This proof-of-concept result may help to overcome current limitations in the growth of high quality thick InGaN nanostructured devices on low-cost substrates by MOCVD. Although this research presents the results of nanoSAG growth of high quality GaN and InGaN nanostructures on polycrystalline AlN on silicon, the method that we present is generic and can be used for deposition on any inexpensive and process-compatible substrate.

4.2 NanoSAG of InGaN and GaN on ZnO [7]

The MOCVD growth of high quality indium-rich InGaN selectively on patterned ZnO (typically 100 nm ZnO on c-Sapphire) templates is challenging because of the need for a relatively reduced growth temperature (for higher indium content) which results in a loss in selectivity. In this work, nano selective area growth (nanoSAG) of InGaN, using exposed HSQ masks as designed on Fig.40, was conducted on ZnO/c-Sapphire wafers.

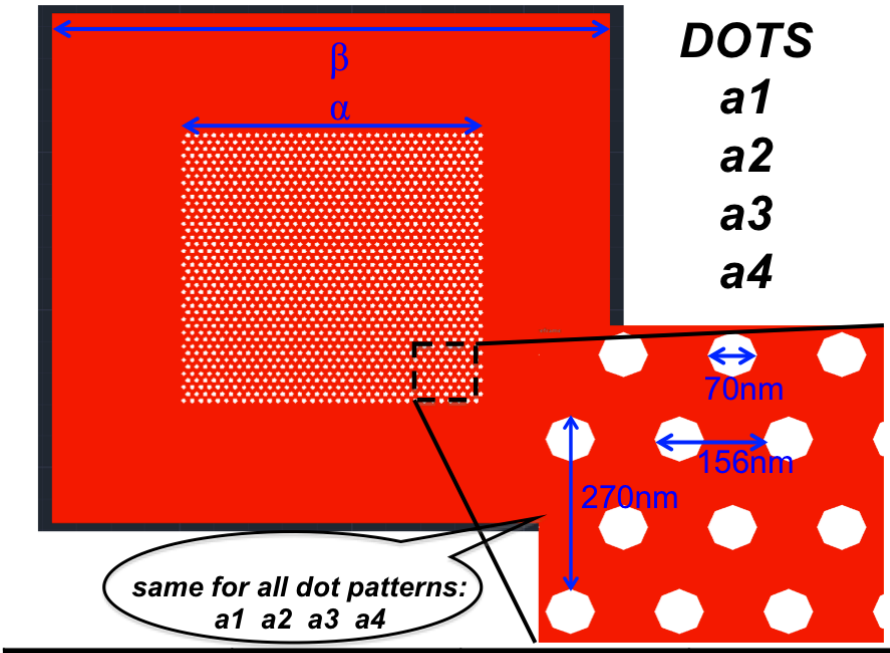

Pattern	α (µm)	β (µm)	mask width (β - α)/2 (µm)
a1	2	10	4
a2	2	34	16
a3	2	66	32
a4	8	10	1

Figure 40. Mask geometry and definition of patterns a1 to a4.

ZnO offers a number of advantages over the typically-used c-sapphire and wurtzite SiC: a lower lattice mismatch with GaN (1.8% vs. resp. 16% and 4%); a lattice match with $In_{.22}Ga_{.78}N$, cf Fig.22; and a better c-axis thermal expansion coefficient. This approach

also has the potential for transfer of the nano InGaN-GaN structures onto alternative substrates (e.g. cheaper or flexible) through chemical liftoff via preferential etching of the ZnO underlayer. [29, 116, 152, 28, 153].

As a first attempt, we have tried to pattern directly the HSQ on top of the ZnO, and then grow the 100 nanometers of InGaN. However it turned out that the maximum allowed temperature is 730°C, apparently too low to maintain selectivity and non-adsorption onto the SiO_2. Indeed nucleation happens all over the mask, as seen on Fig.41. In our MOVPE

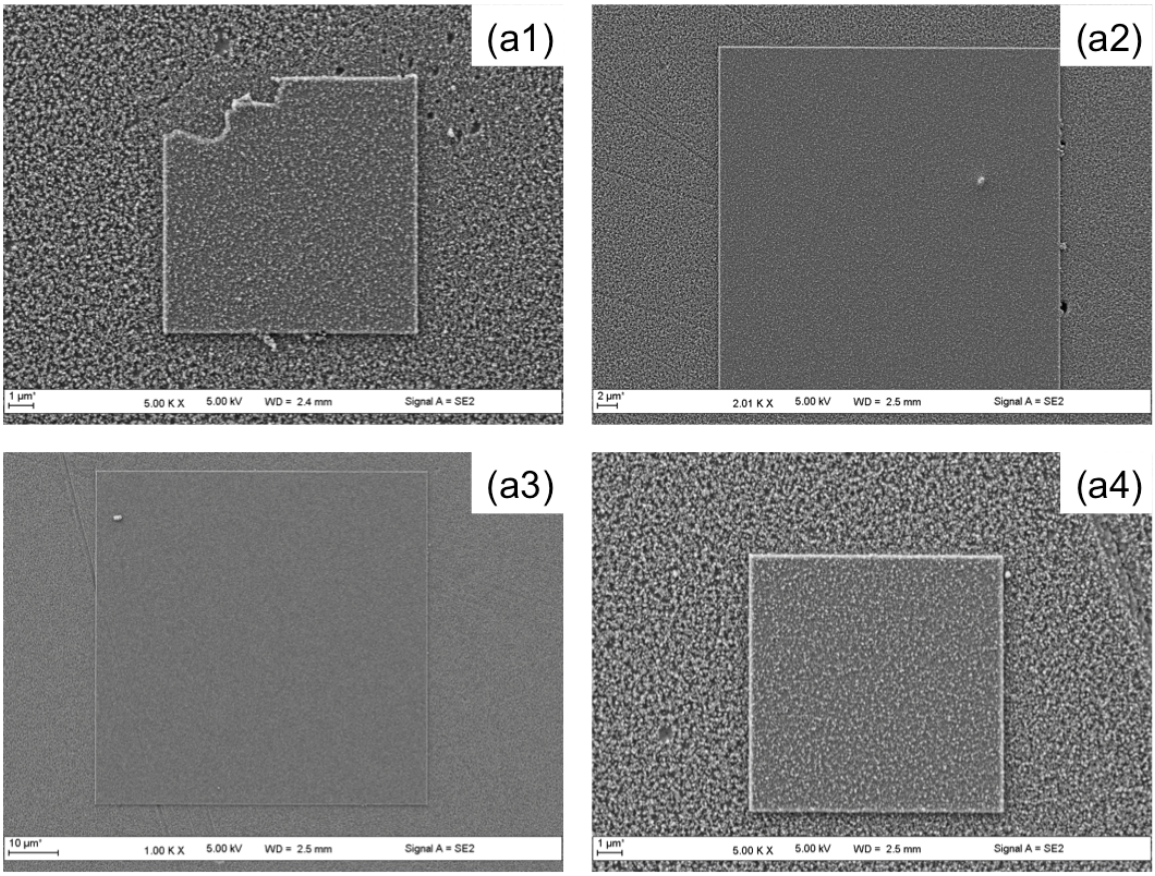

Figure 41. SEM of 100 nm thick InGaN growth directly on patterned ZnO templates. As can be clearly observed, selectivity is lost, due to the low temperature required for ZnO templates

growth conditions (100 Torr of gaseous H_2 or N_2, for growth of GaN and InGaN respectively), any temperature over 730°C leads to dissociation of ZnO [154]. Plus ammonia (NH_3), the typical precursor gas for atomic nitrogen N, and the typical carrier gas dihydrogen H_2, end up in this case damaging the surface of zinc oxide, and even remove the

200-nm-thick ZnO, leading to a delamination of the GaN layer. This happens via a mix of 2 dominant mechanism: the intrinsic thermal instability of ZnO, the back etching of ZnO by H_2(g) and NH_3(g), and the resulting out-diffusion of Zn and O from the ZnO into the GaN [155, 156, 157].

Drs Gautier and Ougazzaden et al. [115, 158] solved this issue in 2008 by growing high quality GaN by MOVPE under N_2 carrier gas (normally H_2) and replacing the ammonia with 1,1dimethylhydrazine. This carcinogen and toxic chemical compound is also known as unsymmetrical dimethylhydrazine, abbreviated UDMH, and is originally famous for its use as a hypergolic rocket fuel. Later on when the acronym DMH is used, we will be referring to its unsymmetrical form UDMH. For gallium nitride growth it allows a diminution of the growth temperature to a range of 550-800°C (typically 1000-1100°C) while maintaining crystal quality and properties.

Hence, in an attempt to restore selectivity, 100 nm of GaN were first grown on the ZnO at low temperature and an SiO_2 overlayer mask was then patterned using e-beam lithography, cf Fig.40. Without GaN, selective growth was hindered and polycrystalline deposits appeared. However, InGaN growth at 800°C was perfectly selective on the GaN/ZnO/Al_2O_3 samples. InGaN nanostructures in the patterned areas show aligned hexagonal faceting, and are homogenous in size, shape, and composition, as can be observed in Figs.42-43. The smooth semipolar facets are free from intrinsic defects within the detection limits of the scanning electron microscope. The aligned facets indicate epitaxial growth. The underlying ZnO still probably tries to dissociate, but is blocked by the GaN, forming micron-sized blisters, as can be seen particularly well on Fig.42(a1) and (a4).

The optical properties of these nanostructures were studied using depth-resolved cathodoluminescence spectroscopy, showing red shift in the emission peaks for patterns (a1), (a2) and (a3), cf. Fig.44, confirming an increase of indium incorporation in these nanostructures compared to the unpatterned area. The incorporation of Indium in the relaxed alloy is calculated using Ref.[31]. Patterns (a1), (a2), (a3), with width of the hole pattern α =

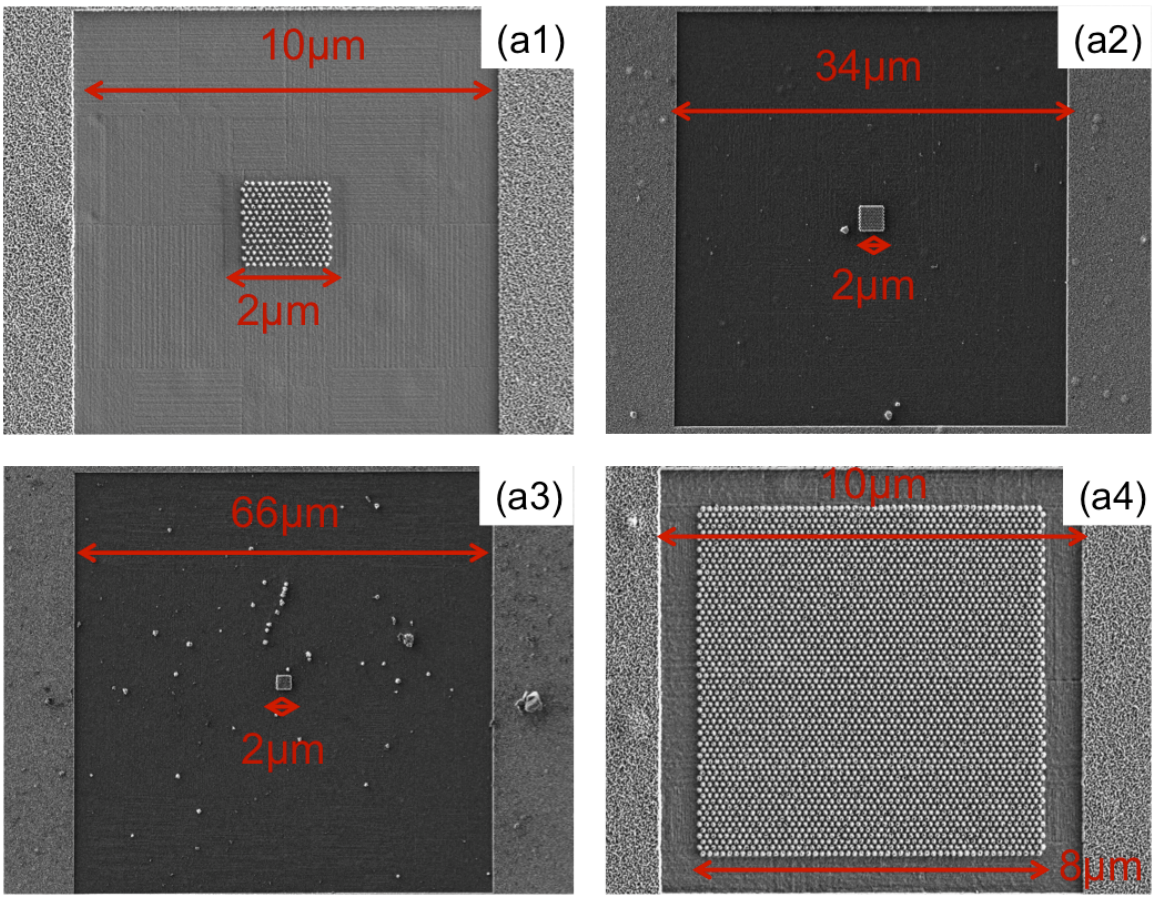

Figure 42. SEM of 100-nm-thick InGaN structures on a GaN (100 nm) / ZnO template. The protective MOVPE-grown 100-nm GaN coating allows growth at higher temperature (800°C), hence restoring selectivity.

2 µm each exhibit a main component at 535 nm (2.32 eV), corresponding to the relaxed high-quality $In_{.22}Ga_{.78}N$. Pattern a4 (α = 8 µm and β = 10 µm) displays a main component at 519 nm (2.39 eV), giving an indium incorporation of 20%. In addition, pattern (a1) exhibits one single and narrow peak at 535 nm (2.32 eV), characteristic of relaxed high-quality $In_{.22}Ga_{.78}N$. Patterns (a2), (a3) and (a4) reveal a second red-shifted shoulder component at around 600-625 nm (resp. 2.07 and 1.98 eV), corresponding to the formation of a second phase with respectively 28% and 30% indium incorporation. Here the dimension of the SiO_2 pattern seems to have an influence on both indium incorporation and InGaN quality.

To conclude, we have demonstrated nano-selective area growth of indium-rich (up to

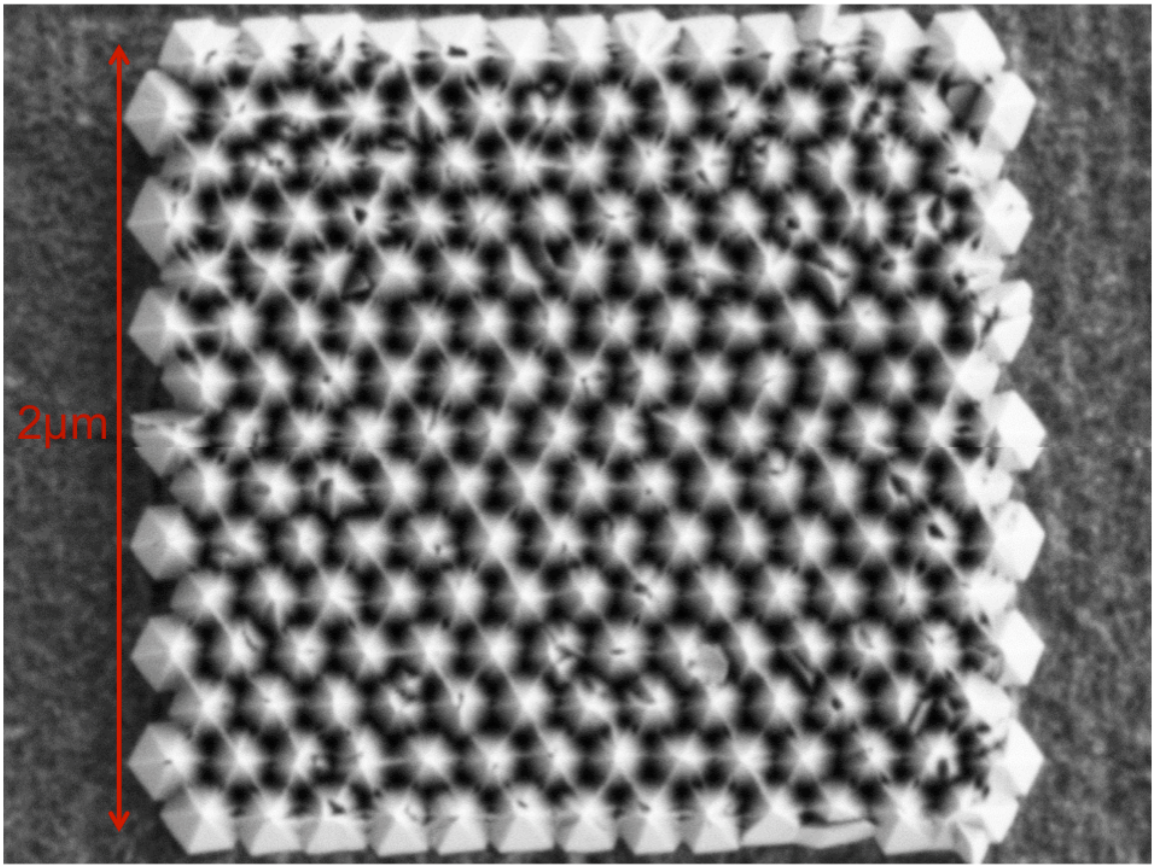

Figure 43. SEM: Zoom on the nanopyramids in pattern (a2).

22%) InGaN nanopyramids on GaN-covered ZnO using MOCVD. This approach yields perfectly selective nanopyramids on zinc oxide substrates. The nanopyramids are single crystalline, dislocation-free, highly uniform, and comparable to nanostructures grown on GaN [4, 5] and AlN/Si [6] templates.

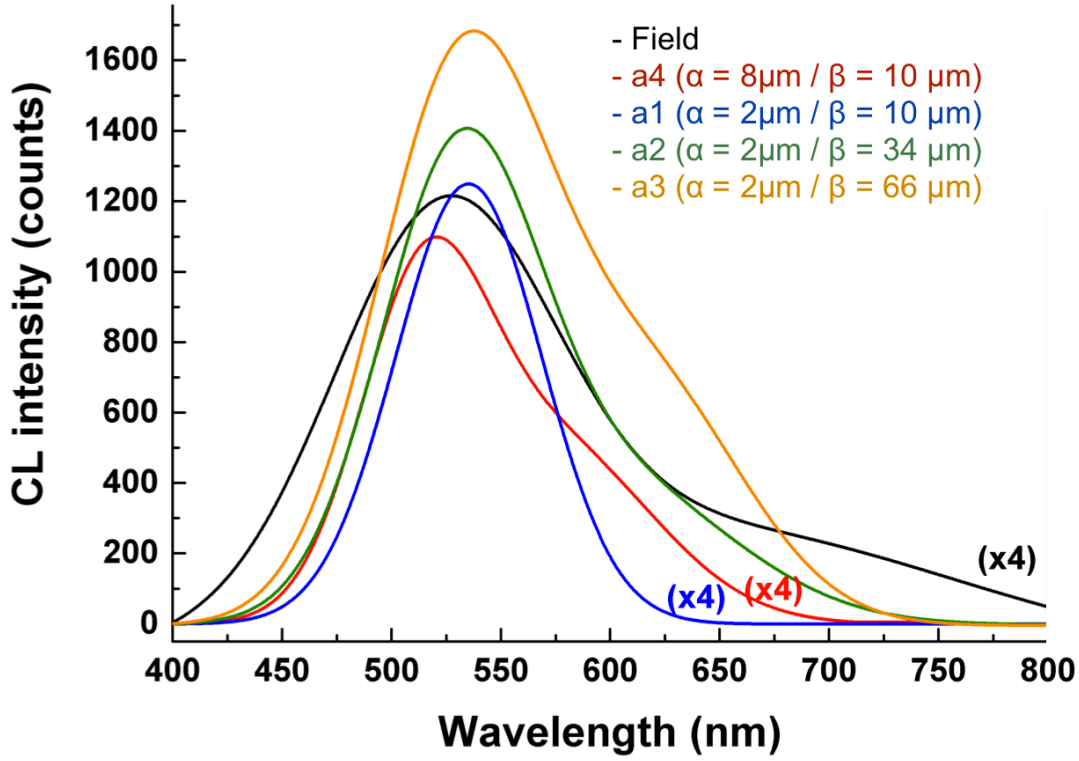

Figure 44. Cathodoluminescence measurement at low temperature (liquid nitrogen at 77K) on nano rods in patterns a1 to a4 coming from one sample, meaning here that all the patterns on this sample have been exposed to the very same growth conditions. A clear trend can be identified on this spectral measurement. On the one hand a1, a2, a3, with width of the hole pattern α= 2 μm all exhibit a main component at 535 nm (2.32 eV), corresponding to corresponding to the relaxed high-quality $In_{.22}Ga_{.78}N$. On the other hand, pattern a4 (α= 8 μm and β= 10 μ) displays a main component at 519 nm (2.39 eV), giving an indium incorporation of 20%. Then pattern a1 exhibits one single and narrow peak at 535 nm (2.32 eV), characteristic of relaxed high-quality $In_{.22}Ga_{.78}N$. Patterns a2, a3 and a4 reveal a second red-shifted shoulder component at around 600-625 nm (resp. 2.07 and 1.98 eV), respectively 28% and 30% indium incorporation. The incorporation of Indium in the relaxed alloy is calculated using Ref.[31]

CHAPTER 5

SELECTIVE AREA GROWTH OF III-NITRIDES USING EPITAXIAL GRAPHENE AS A MASK: TOWARDS FULLY INTEGRATED III-NITRIDE / GRAPHENE / SIC ELECTRONICS AND OPTOELECTRONICS [8, 9]

For the last chapter of what has been a very exciting adventure, we report very encouraging results concerning the growth of high quality gallium nitride (GaN) crystals, 30-nm thick, on the carbon face $(000\bar{1})$ of 4H-silicon carbide (SiC) using nano selective area growth (nanoSAG) with *epitaxial graphene as a mask*. The study of graphene as a potential transparent electrode for III-N optoelectronic devices has been taking off in the past five years [159, 160, 161, 162, 163, 164, 165]. Epitaxial graphene on SiC can also be used as a substrate for van der Waals epitaxy of GaN, and even InGaN-GaN multi-quantum well (MQWs) LEDs [166].

In our approach, graphene is first grown by confinement-controlled sublimation (CCS) of SiC [16]. Then the graphene is patterned using conventional lithography and etched using oxygen plasma. After chemical treatment in hydrofluoric acid (to remove the exposed resist and possible oxide of SiC due to O_2 plasma etch), the sample is loaded in a T-shaped metal organic vapor phase epitaxy (MOVPE) reactor [115] for nanoSAG. We observe that GaN grows exclusively on SiC in the holes patterned through the graphene, with no nucleation on the graphene. Nucleation does not even occur on the pleats of epitaxial graphene.

5.1 First step: controllable growth of C-face epitaxial graphene of consistent high quality using confinement controlled sublimation of silicon carbide

In this technology, we use a single bake anneal-growth process in the same CCS furnace [16] and crucible as in Section 2.1, where an intermediate annealing at 1250°C for 20 minutes atomically flattens the surface of a chemically-and-mechanically polished (CMP) C-face silicon carbide die (the CMP polish is realized by our SiC supplier Cree Inc). All the steps occur under a chamber vacuum of approximately 4×10^{-6} mbar = 4×10^{-4} Pa, but let's not forget that this pressure is outside the crucible: inside the Knudsen graphite cell, the Si sublimating from the sample and the Si coming from the "loaded" crucible impose a vapor pressure right below equilibrium [167, 16], as tabulated by Lilov [26] and illustrated in the Clausius-Clapeyron diagrams on Fig.17 in Section 2.4. For example, during SiC sublimation and graphene formation at 1425°C, Lilov predicts a silicon vapor pressure of 2×10^{-2} Pa, almost two orders of magnitude higher than what we impose outside of the crucible. And this is ideal for the SiC crystal, because this way it can impose its own equilibirum Si vapor pressure for a given temperature and graphene grows close to equilibirum in an optimal and self-controlled manner. Also this has the advantage of growing high quality epitaxial graphene without the need to unload the sample and reload in a different machine between atomic-flatten and sublimation, while providing atomic flatness on par with a H_2-treated surface [168].

On Fig.45 can be observed and measured the effect of the 1250°C - 20 mn annealing step: a sample has been taken out of the CCS furnace right after the 1250°C annealing, before the graphitization step at 1425°C. Our $(000\bar{1})$ surface becomes atomically flat, revealing regular atomic terraces, and measures a typical half-nanometer in root mean square (RMS) roughness.

However, usually the sample stays inside the CCS furnace for graphene growth. For the series of samples used in this chapter, we started by "initializing" the very same crucible

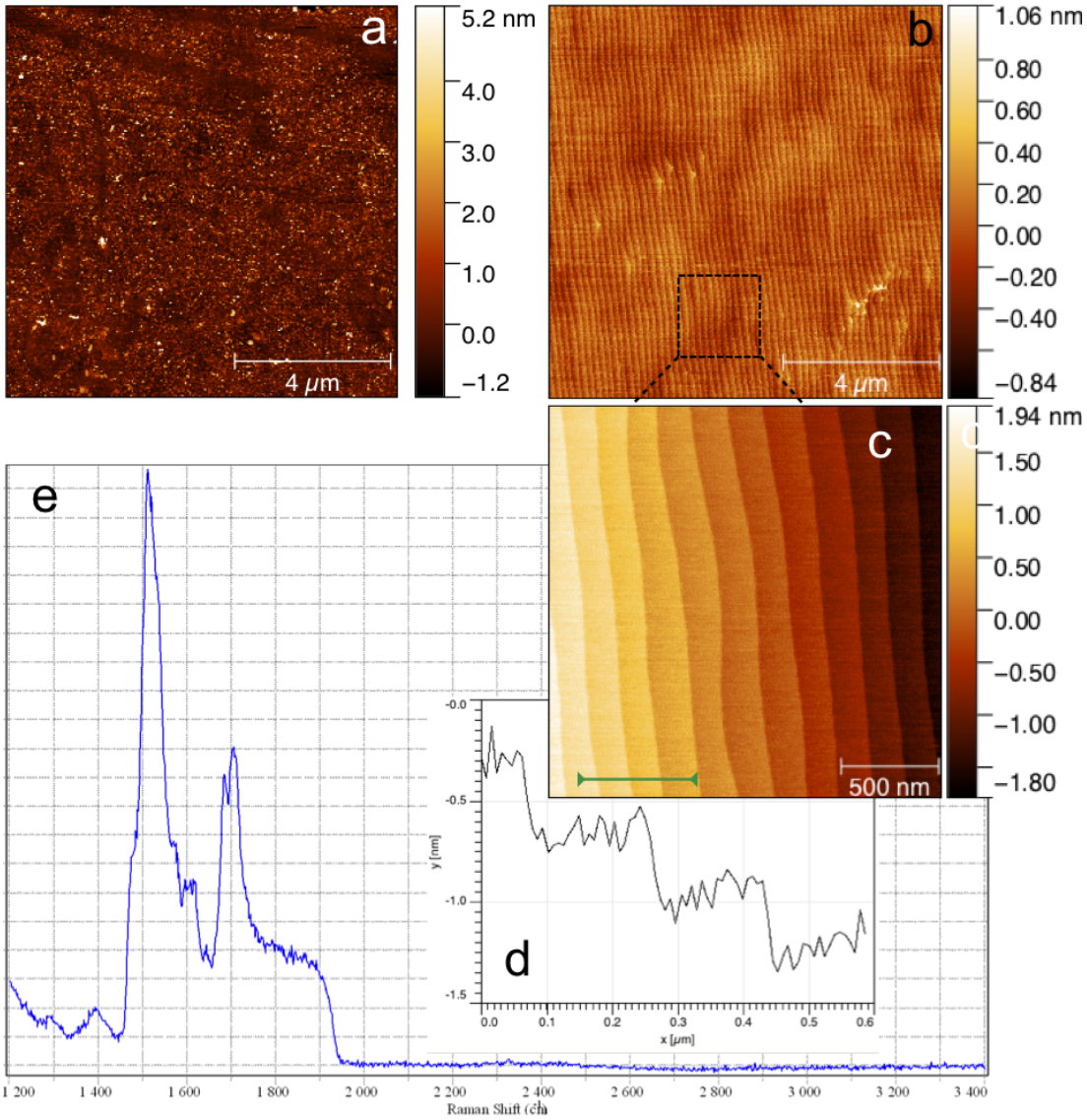

Figure 45. AFM, profilometry and Raman spectrum of a sample before and after annealing. (a) AFM of a CMP-polished SiC C-face from Cree Inc. (b) AFM after annealing 810°C for 10 minutes and 1250°C for 20 minutes. The atomic terraces form at 1250°C (the first thermal annealing at 810°C has not impact on SiC surface morphology and is used as a warm-up / cleaning step). (c) AFM, zoom on the atomic terraces. (d) Profilometry of the green segment. (e) Raman measurement from 1200 to 3400 cm^{-1} showing the typical SiC spectrum.

used for the SiN-on-SiC samples from Chapter 2, cf Fig.9 in Section 2.1. Initialization is achieved by loading the crucible with a dummy SiC sample (usually an edge piece of the 2-inch wafer), and heating up at 1600°C for one hour (compared with 1420-1500°C for 8-20 mn for regular C-face growth). The crucible becomes "loaded" with SiC and/or Si, cf Fig.9 in Section 2.1, and we can obtain high-quality graphene from the very first sample after this maneuver. Then the temperature was optimized to 1425°C, high enough for graphene to form, and low enough to give us single-layer control of thickness with the duration of the step, between 9 and 15 minutes, respectively for 1 to 4 layers. This temperature also maximizes domain size ($\simeq$ 2-5 μm), minimizes the Raman D peak (even undetectable sometimes) and sharpens and maximizes the Raman 2D peak. Figure 46 gives AFM images and Raman spectra of 4 samples.

The AFM images of Fig.46 and Appendix A confirm the presence of graphene, as shown by the MEG characteristic pleats (also known as folds, ridges, ripples, rumples, creases, and puckers) [16]. They have comparable characteristics in terms of pleat structure, including pleat height (1.5-2.4 nm), pleat surface density, and semi-hexagonal orientation. All the Raman spectra in Fig.46 and Appendix A reveal the characteristic graphene peaks. The graphene 2D and G Raman peaks are clearly identified (the SiC Raman contribution was kept in red, subtracted in blue). The 2D peaks can be fitted by a single Cauchy-Lorentz distribution [97] centered between 2694 and 2700 cm^{-1} and with FWHM comprised between 23 and 41 cm^{-1} (see Appendix A for all the measurements). The D peak at 1350 cm^{-1} is very small, or unnoticeable, in all cases. This indicates low defect density in the graphene lattice. Specifically, we do not observe the characteristic shouldered 2D peak of highly ordered pyrolitic graphite (HOPG), as already reported for multilayered epitaxial graphene on the C-face [97].

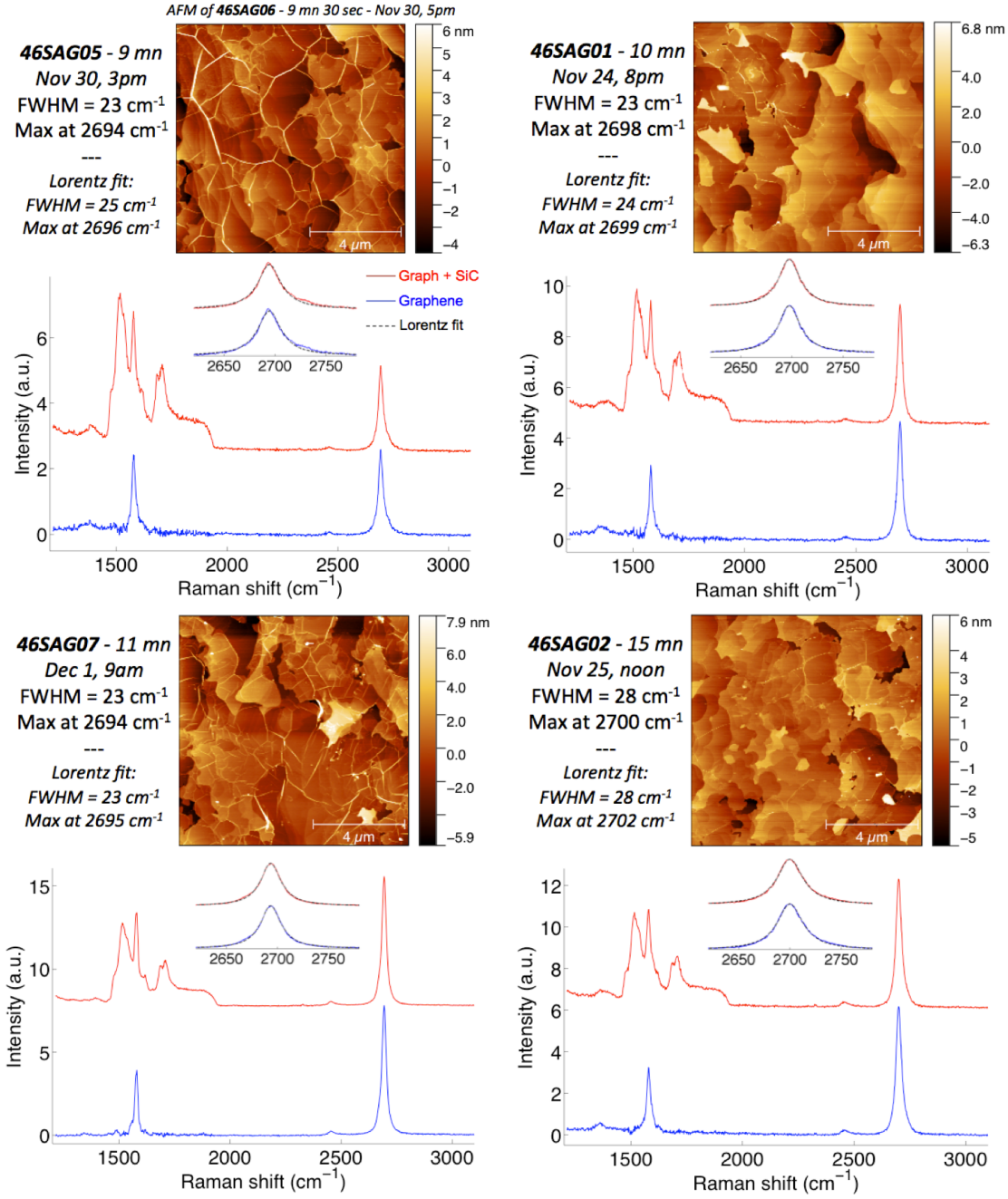

Figure 46. CCS graphitization of C-face $(000\bar{1})$ SiC from 9 to 15 mn, AFM and Raman spectrum.

5.2 Preliminary result: graphene can be used as a mask for selective area growth [9]

Graphene, thanks to its good transparency (97.7% per layer), its thickness tunable down to a single layer of sp^2 carbon atom ($\simeq$ 3.3 Å per layer), and high mobility ($\approx 10^4$ cm^2/V.s.), could become the ideal successor to indium tin oxide (ITO) for transparent conducting electrodes. Interest for such a use in optoelectronic devices has started to grow at the beginning of the decade, in particular concerning gallium-nitride-based light-emitting diodes (LEDs) [160, 159]. However the lack of a native substrate for GaN requires heteroepitaxy in order to prepare templates or devices. It would be desirable to have more options for III-N materials growth on the micro- and nano-scale. It turns out that SiC is a substrate of choice for such devices. Indeed wurtzite GaN has a small lattice mismatch (3.5%) with 4H- or 6H-SiC and grows selectively on SiO_2-masked SiC [135]. Moreover graphene and SiC are compatible with high temperature MOVPE growth processes. At last a selective area growth (SAG) of GaN on graphene-masked SiC would give a direct electronic connection between an active optoelectronic alloy and a high-mobility electrode, potentially improving the performance of GaN-based optoelectronic devices.

We report successful SAG by metal organic vapor phase epitaxy (MOVPE) of GaN on 4H-SiC ($000\bar{1}$, C-face) using patterned multi-layer epitaxial graphene (MEG, 5 layers thick) as a mask. GaN exhibits very good selectivity by not growing on graphene bands even 60 μm wide. First Fig.47 presents the design of the graphene / SiC sample. Then the sample is loaded into the MOVPE reactor for growth of 30 nm of GaN. For reference, the typical value of the diffusion length D/k for selective area growth of GaN using standard lithography PECVD SiO_2 as a mask is 11 μm [169, 135]. We have achieved longer non-nucleation distances with our single-step process involving e-beam exposed HSQ as a mask for SAG, in the order of 20-30 μm, cf Fig.42 in Section 4.2. Fig.48 displays SEM images of the resulting growth, showing absolutely no nucleation of GaN on the graphene in gaps even 60 μm wide.

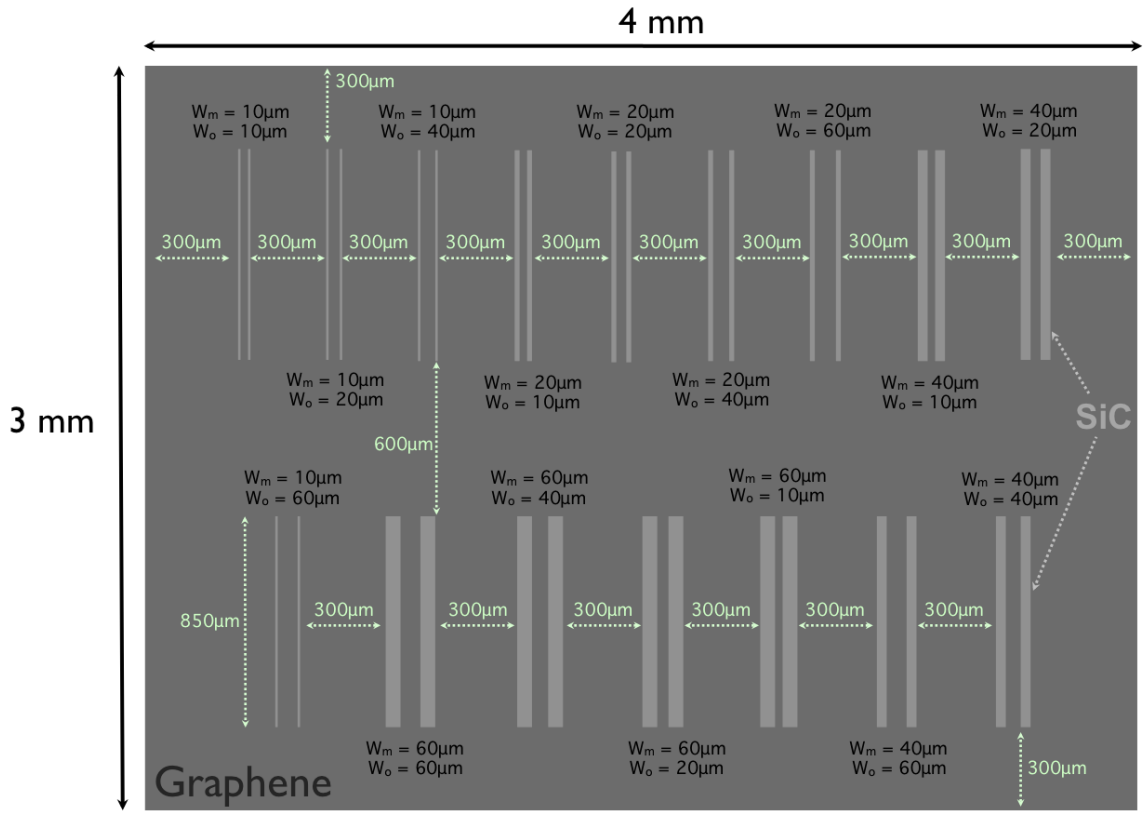

Figure 47. Design of the sample to be obtained after microelectronics processing, achieved by photolithography and oxygen plasma etching of the graphene. W_m (width of the mask, refers to the width of the SiC stripe carved into the graphene. W_o (width of the opening), refers to the width of the graphene in between the corresponding pair of SiC stripes.

We have shown that epitaxial graphene makes for a better mask for selective area growth of GaN on SiC, with diffusion length exceeding the typically used glass by at least a factor of five for PECVD SiO_2, and a factor of 2-3 better than the glass obtained by cross-linking of HSQ e-beam resist. However, with micron-sized openings, nanoSAG could not occur, and the resulting GaN is polycrystalline, and overall of very poor quality, cf Fig.48. Nanoscale holes could solve this issue and allow clean relaxation of the GaN crystal like we already did on various substrates in Chapters 3 and 4 using exposed HSQ as a mask.

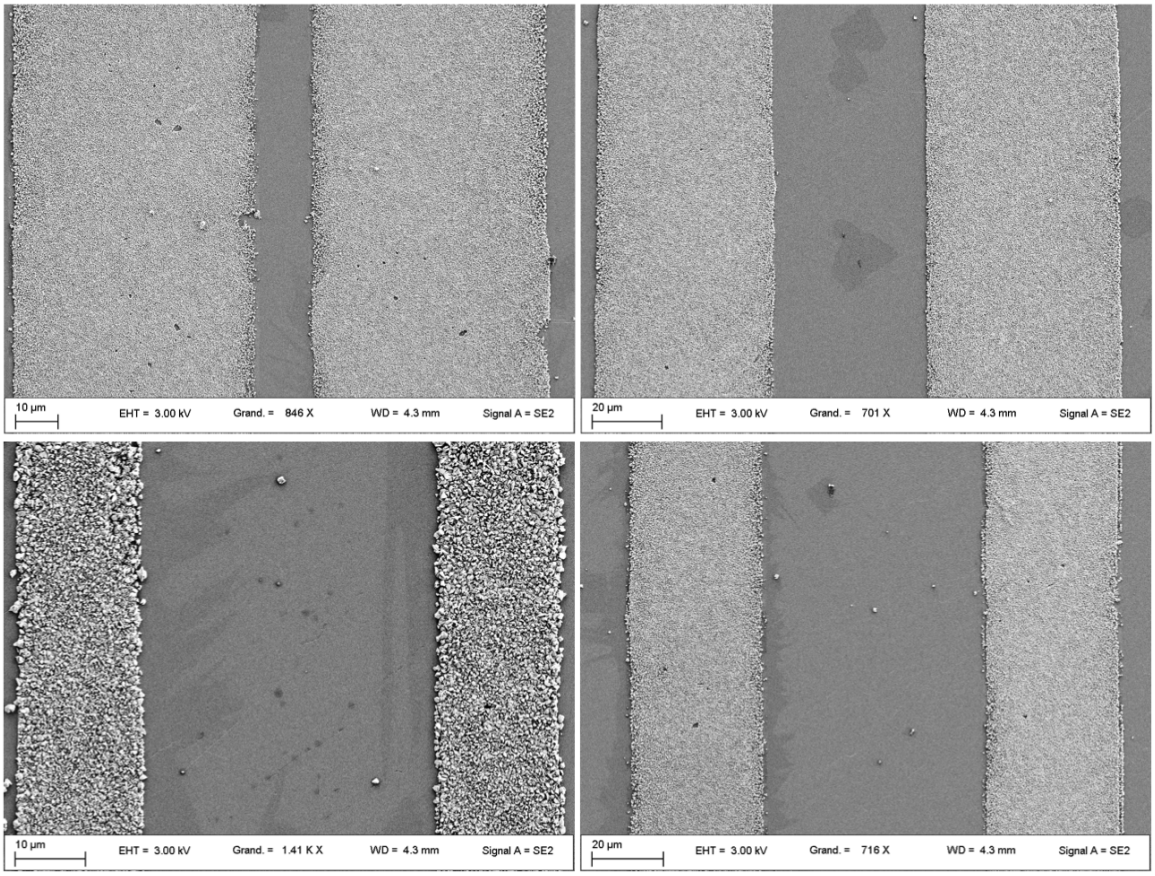

Figure 48. SEM pictures of SAG of 30 nm thick GaN on 4H-SiC, C-face, 5-layer (≃ 1.6 nm) MEG as the mask. *(top left)* GaN 60 µm, graphene 10 µm. *(top right)* GaN 60 µm, graphene 40 µm. *(bottom left)* GaN 20 µm, graphene 40 µm. *(bottom right)* GaN 40 µm, graphene 60 µm.

5.3 NanoSAG of GaN on SiC using epitaxial graphene as a mask

We observe that the GaN grows preferentially from the SiC holes, typically 75 nm in diameter, cf Fig.49, in the shape of equilateral-triangle-base pyramids, while not nucleating at all on the epitaxial graphene. Their (0001) plane (top triangles on Fig.49b-c) point

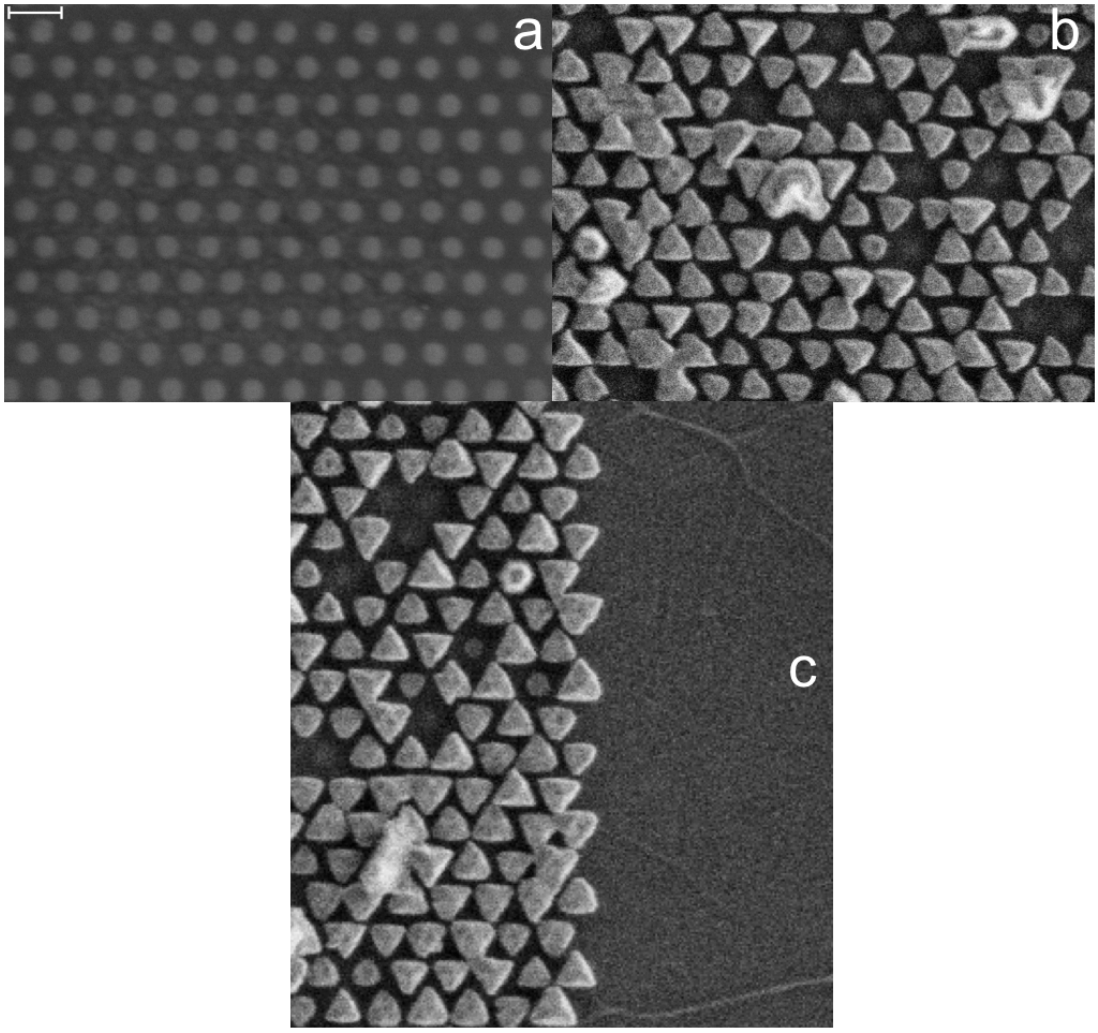

Figure 49. SEM images of nanoSAG of 30nm-thick GaN on 4H-SiC C-face using epitaxial graphene as a mask. *Scale bar is 200 nm.* (a) before GaN growth, pattern of graphene (dark) on SiC (clear). (b) after MOVPE of 30 nm of GaN, GaN triangle-based nanopyramids (clear) grow selectively from the holes revealing the SiC, not on the graphene (dark); (c) after MOVPE of 30 nm of GaN, zoom on the edge of the mask, where we can see that GaN nucleates only on the SiC (holes), and does not nucleate at all on the graphene, not even on the pleats.

exclusively towards the [1-100] direction (up on Fig.49b-c), or the [-1100] direction (down on Fig.49b-c) from common (-1100) planes (horizontal facets on Fig.49b-c). This growth

is different from the typical hexagonal pyramids and their six (1-101) or (1-102) triangular r-plane facets [135, 4, 5].

This process is repeatable and is compatible with industry, using electronics fabrication equipment from the Epitaxial Graphene Lab (School of Physics, Georgia Tech) and Georgia Tech's IEN. This is, to our knowledge, the first time graphene is used as a mask for nanoSAG. In this case we show that a high-quality nitride material can be grown directly in contact of a potential back electrode, graphene, on industry-grade SiC (supplied by Cree Inc.).

CHAPTER 6

CONCLUSION

During this memorable transatlantic adventure, it has been first shown that by using a $Si_{3+x}N_4$ vanishing mask evaporated onto SiC prior to graphitization a modified graphene thickness is achieved between masked and non-masked areas. Depending on its chemical composition (Si-rich or N-rich) the $Si_{3+x}N_4$ mask acts as an enhancer or inhibitor of graphene growth (+/- 3 graphene layers with the present growth conditions). For few layer samples, areas with and without graphene can therefore be produced side by side during the heating process. The mask evaporates during graphene growth so that patterned, mask-free graphene layers are obtained directly in a single heating step. We believe this is a very simple yet potentially quite powerful method to obtain clean patterned graphene structures without the need for post-growth etching. Should this research be continued, two main axes study seem judicious. The first direction is the understanding of the full process by validating (or not) the theories described in this chapter. The second is to determine the limits of this technology, meaning how small and precise these direct patterns of graphene can be grown, and see if we can push from submicron to sub-100-nanometer or even sub-10-nanometer critical dimensions.

Then, on what started as a separate project, we have demonstrated nano-selective area growth (nanoSAG) of InGaN on GaN / c-sapphire by MOCVD using an innovative single-step, industry-friendly, and environmentally friendly patterning process. This approach yields perfectly selective and defect free InGaN nanostructures by avoiding strain related degradation and In clustering observed in bulk planar InGaN. Also PIN structures with InGaN nanorod demonstrate rectifying behavior. These results are very encouraging as the technique may overcome current limitations in the growth of high quality thick InGaN nanostructures and may be important for the realization of InGaN-based high efficiency solar cells.

Also, using the very same process, we have demonstrated that we can grow the very same quality and thickness of InGaN on other substrates, like silicon or zinc oxide. As sapphire is expensive, these two cheap options open the door to a potential commercial success of such a process, which does not seem to depend on the substrate it is executed on.

And last but certainly not least, we have discovered that epitaxial graphene on silicon carbide can be used as a mask for nanoSAG of III-nitrides. We believe this work will open many doors towards the direct integration of high-quality III-nitride materials with graphene-on-SiC electronics, e.g. in terms of optoelectronic and high-frequency electronic applications. The work which has been presented here opens up the possibility of fully pre-patterning and pre-growing a silicon carbide chip using silicon nitride [1], etched SiC terraces [63, 17], and amorphous carbon for the contacts [114, 107]. Then such a chip, in a single heating step, using a single furnace, would grow high-quality graphene in these pre-determined locations; this step could marry ballistic devices (sidewall nanoribbons) with 2D semi metal (graphene) and semiconductor (SiC). At last, III-nitrides can be grown by selective area MOVPE on SiC in between pre-grown graphene structures [8] which could be used as electrodes, to produce optoelectronic and high-frequency devices; and could the appropriate precursors be injected in the same furnace, we would not even need to unload the sample. A fully-integrated multi-functional chip could then be obtained from the pre-patterned SiC.

For future work, I am starting a postdoctoral contract at Georgia Tech Lorraine with Dr Abdallah Ougazzaden, during which two main axes will be explored. First, nanoscale selective area growth of InGaN on GaN-on-sapphire, ZnO-on-sapphire and silicon will be further investigated, the objective being the production of cheap and high-quality opto-electronic prototypes, starting with LEDs and solar cells. According to the crystal quality obtained so far, we should be able to build LEDs and/or photovoltaic cells on ZnO and

Si having the same performances than the ones built on sapphire. On this matter I have already trained Matthew Jordan, a PhD student at School of Electrical and Computer Engineering of the Georgia Institute of Technology, advised by Dr Abdallah Ougazzaden and Dr Paul L Voss. As part of his doctorate he is and will continue producing nanoscale exposed HSQ masks on various substrates, as well as full processing (etching, metallization, ...) for device fabrication and characterization.

Then we will further study the growth of III-N crystals on SiC using epitaxial graphene as a mask, starting with GaN. This part will be performed in full collaboration with Dr Walt A de Heer and Dr Claire Berger from the School of Physics of the Georgia Institute of Technology. In the immediate future, scanning transmission electron microscopy, cathodoluminescence, and electrical measurements will be carried out to clearly identify the structure and quality of the crystals, as well as their electronic properties when using graphene as a back electrode (typically n-contact). Then proof-of-principle optoelectronic devices will be built, in the form of p-GaN / i-InGaN / n-GaN and multiple-quantum-well light-emitting diodes. Furthermore heat conduction studies can also be performed, to quantify the impact that the graphene electrode can have as a thermal sink for optoelectronic prototypes, and the consequences on performance. At last it would be interesting to explore nanoSAG using the sidewall nanoribbons as a mask, in order to exploit the ballistic transport properties of these ribbons. The major unknown here is whether the buffer layer, which grows on the (0001) facets, will allow nucleation of III-N crystals.

APPENDIX A

GROWTH OF SINGLE- AND MULTI-LAYER C-FACE EPITAXIAL GRAPHENE

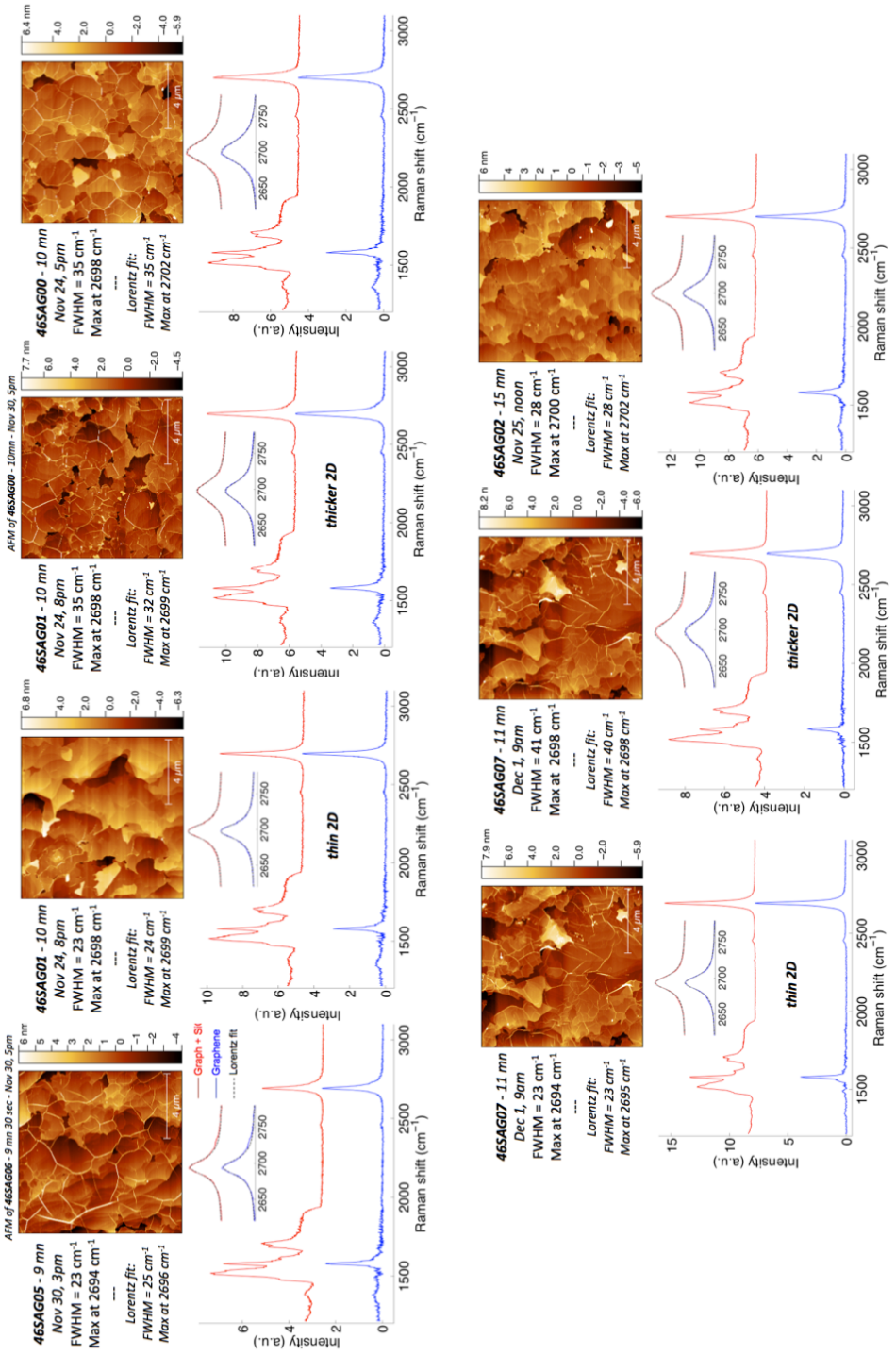

Figure 50. Single- and multi-layer epitaxial graphene, AFM and Raman spectrum.

APPENDIX B

CROSS-SECTIONAL INELASTIC MEAN FREE PATH OF MULTI-LAYER EPITAXIAL GRAPHENE: AN ELLIPSOMETRY AND X-RAY PHOTOELECTRON SPECTROSCOPY STUDY.

As a addendum, we have determined the cross-sectional inelastic mean free path of MEG, referred here as C-IMFP, the distance over which X-ray-freed electrons travel *through* graphene sheets before scattering. The mean free path of the conductive π electrons along the graphene plane has already been extensively studied in the past eight years[15, 49, 59]. Values for the IMPF in SiC vary from 3 nm [170], to 4 nm [171, 172], and 2 to 4 nm for graphite [171]. This literature review concerns Al K-alpha radiation at $h\nu = 1486.6eV$, as used in our case. In XPS, the probability to detect a photo-excited electron decays exponentially as we go deeper in the material. The IMPF λ is defined as the depth from which the probability of detection P(x) is $1/e \simeq 37\%$:

$$P(x) = \frac{I(x)}{I_0} = e^{-x/\lambda} \tag{14}$$

XPS measurements reveal clear atomic percentages, giving C and Si content in the material. Then, for a MEG-on-SiC sample, the probability of a photo-emitted electron to come from the SiC is equal to twice the Si probability. Indeed $P_{Si} = 1 - P_C - P_{oxygen}$, 4H-SiC being at a 1:1 ratio of silicon and carbon atoms (cf. witness sample on Table 1), leading to a good approximation:

$$\lambda \simeq -\frac{t}{ln(2.P_{Si})} = 13.4 \pm 1.7\text{Å} \tag{15}$$

Then from various samples listed in Table 1 we calculate the average C-IMPF for graphene, and the standard deviation as shown in (3).

As a remark on the table, we can observe that that except the levels of oxidation vary from one sample to another, with consistently $P_O = 1 - P_C - P_{Si}$, probably due to differences in exposure to air from graphitization to the XPS measurement. The oxygen content P_O remains at a few percents at the most, justifying its negligible nature in (3). Hence XPS can be used to determine the thickness of a MEG film.

Table 1. XPS and ellipsometry measurements used for graphene C-IMPF calculation.

t (ellipso)	$P_{C(1s)}$ (XPS)	$P_{Si(2p)}$ (XPS)	C-IMPF
0	49.7 %	47.1%	n/a
6.5 Å	70.8 %	29.0 %	12.7 Å
6.9 Å	72.0 %	27.7 %	11.0 Å
15 Å	77.8 %	17.2 %	14.1 Å
18 Å	82.9 %	13.1 %	13.4 Å
27 Å	85.8 %	8.9 %	15.6 Å

REFERENCES

[1] R. Puybaret, J. Hankinson, J. Palmer, C. Bouvier, A. Ougazzaden, P. L. Voss, C. Berger, and W. A. de Heer, "Scalable control of graphene growth on 4H-SiC C-face using decomposing silicon nitride masks," *Journal of Physics D - Applied Physics*, vol. 48, p. 152001, April 2015 (arXiv:1307.6197 since July 2013).

[2] R. Puybaret, P. L. Voss, A. Ougazzaden, J. Hankinson, W. A. de Heer, and C. Berger, "Local control of C-face 4H-SiC graphene thickness using decomposing silicon nitride masks," *EMRS Spring Meeting - Strasbourg, France - Oral presentation*, May 2013.

[3] R. Puybaret, P. L. Voss, A. Ougazzaden, J. Hankinson, J. Palmer, W. A. de Heer, and C. Berger, "Scalable control of graphene growth on 4H-SiC C-face using decomposing silicon nitride masks," *European Physical Society, Graphene 2014 - Toulouse, France - Oral presentation*, May 2014.

[4] S. Sundaram, R. Puybaret, Y. El Gmili, X. Li, P. L. Bonanno, K. Pantzas, G. Orsal, D. Troadec, Z. H. Cai, G. Patriarche, P. L. Voss, J. P. Salvestrini, and A. Ougazzaden, "Nanoscale selective area growth of thick, dense, uniform, In-rich, InGaN nanostructure arrays on GaN/sapphire template," *Journal of Applied Physics*, vol. 116, Oct 28 2014.

[5] S. Sundaram, R. Puybaret, X. Li, Y. El Gmili, J. Streque, K. Pantzas, G. Orsal, G. Patriarche, P. L. Voss, J. P. Salvestrini, and A. Ougazzaden, "High quality thick InGaN nanostructures grown by nanoselective area growth for new generation photovoltaic devices," *Physica Status Solidi A*, Feb 2015.

[6] S. Sundaram, Y. El Gmili, R. Puybaret, X. Li, K. Pantzas, G. Patriarche, P. L. Voss, J. P. Salvestrini, and A. Ougazzaden, "Nanoselective area growth and in-depth characterization of dislocation-free InGaN nanopyramids on AlN buffered Si(111) templates," *submitted to Applied Physics Letters*, March 27 2015.

[7] R. Puybaret, S. Sundaram, X. Li, Y. El Gmili, K. Pantzas, D. Troadec, G. Patriarche, D. J. Rogers, F. H. Teherani, V. E. Sandana, P. Bove, P. L. Voss, J. P. Salvestrini, and A. Ougazzaden, "Nanoselective area growth of high quality thick InGaN/GaN on sacrificial ZnO templates," *EMRS Spring Meeting, Lille, France, Oral presentation - submitted to Phys Stat Sol A*, May 2015.

[8] R. Puybaret, Y. El Gmili, S. Sundaram, M. B. Jordan, J. P. Salvestrini, P. L. Voss, W. A. de Heer, C. Berger, and A. Ougazzaden, "Nano selective area growth of GaN on the C-face of 4H-SiC using epitaxial graphene as a mask: towards fully integrated III-nitride/graphene/SiC electronics and optoelectronics," *International Conference*

on Nitride Semiconductors, accepted for Oral Presentation - Beijing, China, Aug 2015.

[9] R. Puybaret, P. L. Voss, A. Ougazzaden, B. Zhang, J. Hankinson, C. Berger, and W. A. de Heer, "Selective Area Growth of GaN on SiC using Graphene as a Mask for Optoelectronics Applications," *3rd International Symposium on the Science and Technology of Epitaxial Graphene STEG3 - St Augustine, FL, USA - Poster*, Oct 24-27 2011.

[10] P. Wallace, "The Band Theory of Graphite," *Physical Review*, vol. 71, no. 9, pp. 622–634, 1947.

[11] H. Boehm, A. Clauss, U. Hofmann, and G. Fisher, "Dünnste Kohlenstoff-Folien," *Zeitschrift Fur Naturforschung Part B*, vol. B 17, no. 3, pp. 150–&, 1962.

[12] A. Van Bommel, J. Crombeen, and A. Van Tooren, "LEED and Auger electron observations of SiC (0001) surface," *Surface Science*, vol. 48, no. 2, pp. 463–472, 1975.

[13] W. A. de Heer, "Early development of graphene electronics," *http://smartech.gatech.edu/xmlui/handle/1853/31270*, 2001-2009.

[14] W. A. de Heer, C. Berger, and P. N. First, "Patterned thin film graphite devices and method for making same," *U.S. Patent 7015142 (prov. filed Jan 12, 2003 - issued Mar. 21, 2006)*, 2003.

[15] C. Berger, Z. Song, T. Li, X. Li, A. Ogbazghi, R. Feng, Z. Dai, A. Marchenkov, E. Conrad, P. First, and W. de Heer, "Ultrathin epitaxial graphite: 2D electron gas properties and a route toward graphene-based nanoelectronics," *Journal of Physical Chemistry B*, vol. 108, no. 52, pp. 19912–19916, 2004.

[16] W. de Heer, C. Berger, M. Ruan, M. Sprinkle, X. Li, Y. Hu, B. Zhang, J. Hankinson, and E. Conrad, "Large area and structured epitaxial graphene produced by confinement controlled sublimation of silicon carbide," *Proceedings of the National Academy of Sciences*, vol. 108, no. 41, pp. 16900–16905, 2011.

[17] J. Baringhaus, M. Ruan, F. Edler, A. Tejeda, M. Sicot, A. Taleb-Ibrahimi, A.-P. Li, Z. Jiang, E. H. Conrad, C. Berger, C. Tegenkamp, and W. A. de Heer, "Exceptional ballistic transport in epitaxial graphene nanoribbons," *Nature*, vol. 506, no. 7488, pp. 349–354, 2014.

[18] H. P. Maruska, "A brief history of gan blue light-emitting diodes," *http://www.sslighting.net/news/features/maruska_blue_led_history.pdf*, Nov 2011.

[19] J. Hass, F. Varchon, J. E. Millán-Otoya, M. Sprinkle, N. Sharma, W. A. de Heer, C. Berger, P. N. First, L. Magaud, and E. H. Conrad, "Why multilayer graphene on 4h-sic(000-1) behaves like a single sheet of graphene," *Physical Review Letters*, vol. 100, p. 125504, Mar 2008.

[20] W. Hincke and L. Brantley, "The high-temperature equilibrium between silicon nitride, silicon and nitrogen," *Journal of the American Chemical Society*, vol. 52, pp. 48–52, Jan 1930.

[21] S. Singhal, "Thermodynamic analysis of the high-temperature stability of silicon nitride and silicon carbide," *Ceramurgia International*, vol. 2, June 1976.

[22] M. Herrmann, C. Schuber, A. Rendtel, and H. Hubner, "Silicon nitride/silicon carbide nanocomposite materials: I, fabrication and mechanical properties at room temperature," *Journal of the American Ceramic Society*, vol. 81, pp. 1095–1108, May 1998.

[23] T. Tomooka, Y. Shoji, and T. Matsui, "High temperature vapor pressure of si," *J. Mass. Spectrom. Soc. Jpn.*, vol. 47, no. 1, pp. 49–53, 1999.

[24] H. Seifert, J. Peng, H. Lukas, and F. Aldinger, "Phase equilibria and thermal analysis of Si-C-N ceramics," *Journal of Alloys and Compounds*, vol. 320, pp. 251–261, May 24 2001.

[25] S. I. Lopatin, V. L. Stolyarova, V. G. Sevast'yanov, P. Y. Nosatenko, V. V. Gorskii, D. V. Sevast'yanov, and N. T. Kuznetsov, "Determination of the saturation vapor pressure of silicon by Knudsen cell mass spectrometry," *Russian Journal of Inorganic Chemistry*, vol. 57, pp. 219–225, Feb 2012.

[26] S. Lilov, "Study of the equilibirum process in the gas phase during silicon carbide sublimation," *Materials Science and Engineering B*, vol. 21, pp. 65–69, Sep 20 1993.

[27] J. Drowart, G. De Maria, and M. G. Inghram, "Thermodynamic study of sic utilizing a mass spectrometer," *Journal of Chemical Physics*, vol. 29, no. 5, pp. 1015–1021, 1958.

[28] S. W. Kaun, M. H. Wong, U. K. Mishra, and J. S. Speck, "Molecular beam epitaxy for high-performance Ga-face GaN electron devices," *Semiconductor Science and Technology*, vol. 28, Jul 2013.

[29] S. Pearton, D. Norton, K. Ip, Y. Heo, and T. Steiner, "Recent progress in processing and properties of zno," *Progress in Materials Science*, vol. 50, no. 3, pp. 293 – 340, 2005.

[30] P. L. Bonanno, S. Gautier, A. A. Sirenko, A. Kazimirov, Z. H. Cai, W. H. Goh, J. Martin, A. Martinez, T. Moudakir, N. Maloufi, M. B. Assouar, A. Ramdane, L. Le Gratiet, and A. Ougazzaden, "Submicron beam X-ray diffraction of nanoheteroepitaxily grown GaN: Experimental challenges and calibration procedures," *Nuclear Instruments and Methods in Physics Research B*, vol. 268, pp. 320–324, Feb 2010. Spring Meeting of the European-Materials-Research-Society, Strasbourg, France, Jun 08-12, 2009.

[31] G. Orsal, Y. El Gmili, N. Fressengeas, J. Streque, R. Djerboub, T. Moudakir, S. Sundaram, A. Ougazzaden, and J. P. Salvestrini, "Bandgap energy bowing parameter of strained and relaxed InGaN layers," *Optical Materials Express*, vol. 4, pp. 1030–1041, May 2014.

[32] J. Bardeen and W. H. Brattain, "The Transistor, a semi-conductor diode," *Physical Review*, vol. 74, no. 2, pp. 230–231, 1948.

[33] W. H. Brattain and J. Bardeen, "Nature of the forward current in germanium point contacts," *Physical Review*, vol. 74, no. 2, pp. 231–232, 1948.

[34] M. Fujita, K. Wakabayashi, K. Nakada, and K. Kusakabe, "Peculiar localized state at zigzag graphite edge," *Journal of the Physical Society of Japan*, vol. 65, pp. 1920–1923, Jul 1996.

[35] K. Nakada, M. Fujita, G. Dresselhaus, and M. Dresselhaus, "Edge state in graphene ribbons: Nanometer size effect and edge shape dependence," *Physical Review B*, vol. 54, pp. 17954–17961, DEC 15 1996.

[36] K. Wakabayashi, M. Fujita, H. Ajiki, and M. Sigrist, "Electronic and magnetic properties of nanographite ribbons," *Physical Review B*, vol. 59, pp. 8271–8282, Mar 15 1999.

[37] J. A. Hoerni, "Method of manufacturing semiconductor devices," *U. S. Patent 3,025,589 (Filed May 1st, 1959. Issued March 20, 1962)*, 1959.

[38] R. N. Noyce, "Semiconductor device-and-lead structure," *U. S. Patent 2981877 (Filed July 30, 1959. Issued April 25, 1961)*, 1959.

[39] D. Kahng, "Electric field controlled semiconductor device," *U. S. Patent No. 3,102,230 (filed 31 May 31, 1960 - issued August 27, 1963)*, 1960.

[40] F. M. Wanlass, "Low stand-by power complementary field effect circuitry," *U.S. patent 3356858 (Filed June 18 1963, Patented Dec. 5, 1967)*, 1963.

[41] G. Moore, "Cramming more components onto integrated circuits (Reprinted from Electronics, pg 114-117, April 19, 1965)," *Electronics*, pp. 114–117, April 19 1965.

[42] K. Novoselov, D. Jiang, F. Schedin, T. Booth, V. Khotkevich, S. Morozov, and A. Geim, "Two-dimensional atomic crystals," *Proceedings of the National Academy of Sciences*, vol. 102, pp. 10451–10453, Jul 26 2005.

[43] K. Novoselov, A. Geim, S. Morozov, D. Jiang, M. Katsnelson, I. Grigorieva, S. Dubonos, and A. Firsov, "Two-dimensional gas of massless Dirac fermions in graphene," *Nature*, vol. 438, pp. 197–200, Nov 10 2005.

[44] Y. Zhang, Y. Tan, H. Stormer, and P. Kim, "Experimental observation of the quantum Hall effect and Berry's phase in graphene," *Nature*, vol. 438, pp. 201–204, Nov 10 2005.

[45] C. Berger, Z. Song, T. Li, P. First, J. Bellisard, and W. de Heer, "Evidence for 2d electron gas behavior in ultrathin epitaxial graphite on a sic substrate," *Bull. Amer. Phys. Soc.*, March 2004.

[46] E. S. Reich, "Nobel document triggers debate," *Nature*, vol. 468, p. 486, Nov 25 2010.

[47] E. Rollings, G. H. Gweon, S. Y. Zhou, B. S. Mun, J. L. McChesney, B. S. Hussain, A. Fedorov, P. N. First, W. A. de Heer, and A. Lanzara, "Synthesis and characterization of atomically thin graphite films on a silicon carbide substrate," *Journal of Physics and Chemistry of Solids*, vol. 67, pp. 2172–2177, Sep-Oct 2006. Conference on Study of Matter at Extreme Conditions (SMEC2005), Miami Beach, FL, Apr 17-21, 2005.

[48] K. Novoselov, A. Geim, S. Morozov, D. Jiang, Y. Zhang, S. Dubonos, I. Grigorieva, and A. Firsov, "Electric field effect in atomically thin carbon films," *Science*, vol. 306, pp. 666–669, Oct 22 2004.

[49] C. Berger, Z. Song, X. Li, X. Wu, N. Brown, C. Naud, D. Mayou, T. Li, J. Hass, A. Marchenkov, E. Conrad, P. First, and W. de Heer, "Electronic confinement and coherence in patterned epitaxial graphene," *Science*, vol. 312, pp. 1191–1196, May 26 2006.

[50] X. Wu, M. Sprinkle, X. Li, F. Ming, C. Berger, and W. A. de Heer, "Epitaxial-graphene/graphene-oxide junction: An essential step towards epitaxial graphene electronics," *Physical Review Letters*, vol. 101, Jul 11 2008.

[51] E. Acheson, "Carborundum: its history, manufacture and uses," *Journal of the Franklin Institute*, vol. 136, no. 3, pp. 194 – 203, 1893.

[52] H. C. Dunwoody, "Wireless telegraph system," 1906.

[53] H. J. Round, "A note on carborundum," *Electrical World*, vol. 19, p. 309, 1907.

[54] P. Ivanov and V. Chelkonov, "Recent developements in SiC single-crystal electronics," *Semiconductor Science and Technology*, vol. 7, pp. 863–880, Jul 1992.

[55] D. Larkin, P. Neudeck, J. Powell, and L. Matus, "Site-competition epitaxy for superior silicon-carbide electronics," *Applied Physics Letters*, vol. 65, pp. 1659–1661, Sep 26 1994.

[56] H. Matsunami and T. Kimoto, "Step-controlled epitaxial growth of SiC: high quality homoepitaxy," *Materials Science and Engineering R-Reports*, vol. 20, pp. 125–166, Aug 1997.

[57] M. Mehregany, C. Zorman, N. Rajan, and C. Wu, "Silicon carbide MEMS for harsh environments," *Proceesings of the IEEE*, vol. 86, pp. 1594–1610, Aug 1998.

[58] M. Han, B. Oezyilmaz, Y. Zhang, and P. Kim, "Energy band-gap engineering of graphene nanoribbons," *Physical Review Letters*, vol. 98, May 18 2007.

[59] X. Wang, Y. Ouyang, X. Li, H. Wang, J. Guo, and H. Dai, "Room-temperature all-semiconducting sub-10-nm graphene nanoribbon field-effect transistors," *Physical Review Letters*, vol. 100, May 23 2008.

[60] J. Kedzierski, P.-L. Hsu, P. Healey, P. W. Wyatt, C. L. Keast, M. Sprinkle, C. Berger, and W. A. de Heer, "Epitaxial graphene transistors on SiC substrates," *IEEE Transactions on Electron Devices*, vol. 55, pp. 2078–2085, Aug 2008.

[61] B. Dlubak, M.-B. Martin, C. Deranlot, B. Servet, S. Xavier, R. Mattana, M. Sprinkle, C. Berger, W. A. De Heer, F. Petroff, A. Anane, P. Seneor, and A. Fert, "Highly efficient spin transport in epitaxial graphene on SiC," *Nature Physics*, vol. 8, no. 7, pp. 557–561, 2012.

[62] J. Hicks, A. Tejeda, A. Taleb-Ibrahimi, M. S. Nevius, F. Wang, K. Shepperd, J. Palmer, F. Bertran, P. Le Fevre, J. Kunc, W. A. de Heer, C. Berger, and E. H. Conrad, "A wide-bandgap metal-semiconductor-metal nanostructure made entirely from graphene," *Nature Physics*, vol. 9, no. 1, pp. 49–54, 2013.

[63] M. Sprinkle, M. Ruan, Y. Hu, J. Hankinson, M. Rubio-Roy, B. Zhang, X. Wu, C. Berger, and W. A. de Heer, "Scalable templated growth of graphene nanoribbons on SiC," *Nature Nanotechnology*, vol. 5, no. 10, pp. 727–731, 2010.

[64] E. H. Hwang and S. Das Sarma, "Acoustic phonon scattering limited carrier mobility in two-dimensional extrinsic graphene," *Physical Review B*, vol. 77, Mar 2008.

[65] Y.-M. Lin, A. Valdes-Garcia, S.-J. Han, D. B. Farmer, I. Meric, Y. Sun, Y. Wu, C. Dimitrakopoulos, A. Grill, P. Avouris, and K. A. Jenkins, "Wafer-Scale Graphene Integrated Circuit," *Science*, vol. 332, no. 6035, pp. 1294–1297, 2011.

[66] Y. M. Lin, C. Dimitrakopoulos, K. A. Jenkins, D. B. Farmer, H. Y. Chiu, A. Grill, and P. Avouris, "100-GHz Transistors from Wafer-Scale Epitaxial Graphene," *Science*, vol. 327, no. 5966, p. 662, 2010.

[67] Z. Guo, R. Dong, P. S. Chakraborty, N. Lourenco, J. Palmer, Y. Hu, M. Ruan, J. Hankinson, J. Kunc, J. D. Cressler, C. Berger, and W. A. de Heer, "Record Maximum Oscillation Frequency in C-Face Epitaxial Graphene Transistors," *Nano Letters*, vol. 13, no. 3, pp. 942–947, 2013.

[68] K. S. Novoselov, V. I. Fal'ko, L. Colombo, P. R. Gellert, M. G. Schwab, and K. Kim, "A roadmap for graphene," *Nature*, vol. 490, pp. 192–200, Oct 11 2012.

[69] O. V. Losev, "Luminous carborundum [silicon carbide] detector and detection with crystals," *Telegrafiya i Telefoniya bez Provodov*, vol. 44, pp. 485–494, 1927.

[70] O. V. Losev, "Luminous carborundum detector and detection effect and oscillations with crystals," *Philosophical Magazine*, vol. 6, pp. 1024–1044, 19238.

[71] J. Lely, "Darstellung von Einkristallen von Siliziumcarbid und Beherrrshing von Art und Menge der im Gitter eingebauten Verunreininungen," *Angewandte Chemie*, vol. 66, no. 22, p. 713, 1954.

[72] M. Cooke, "Semiconductor hardnut - Technical Feature, Silicon Carbide," *III-Vs Review - The Advanced Semiconductor Magazine*, vol. 18, Dec 2005.

[73] N. Zheludev, "The life and times of the LED - a 100-year history," *Nature Photonics*, vol. 1, pp. 189–192, Apr 2007.

[74] J. R. Biard and G. E. Pittman, "Semiconductor radiant diode," *U.S. Patent US3293513 (filed Aug. 8, 1962)*, Dec. 20 1966.

[75] N. Holonyak and S. F. Bevacqua, "Coherent (visible) light emission from Ga(As1-xPx) junctions," *Applied Physics Letters*, vol. 1, no. 4, pp. 82–83, 1962.

[76] M. Craford, R. Shaw, A. Herzog, and W. Groves, "Radiative recombination mechanisms in GaAsP diodes with and without nitrogen doping," *Journal of Applied Physics*, vol. 43, no. 10, pp. 4075–&, 1972.

[77] H. P. Maruska and J. J. Tietjen, "The preparation and properties of vapor-deposited single-crystalline GaN," *Applied Physics Letters*, vol. 15, no. 10, pp. 327–&, 1969.

[78] N. V. Patel, "Nobel Shocker: RCA Had the First Blue LED in 1972," *IEEE Spectrum*, Oct. 9 2014.

[79] J. I. Pankove, J. E. Berkeyhe, H. P. Maruska, and J. Wittke, "Luminescent properties of GaN," *Solid State Communications*, vol. 8, no. 13, pp. 1051–&, 1970.

[80] H. P. Maruska, D. A. Stevenson, and J. I. Pankove, "Violet luminescence of Mg-doped GaN," *Applied Physics Letters*, vol. 22, no. 6, pp. 303–305, 1973.

[81] H. P. Maruska, D. A. Stevenson, and W. C. Rhines, "Preparation of Mg-doped GaN diodes exhibiting violet electroluminescence," *Materials research Bulletin*, vol. 7, no. 8, pp. 777–&, 1972.

[82] D. A. Stevenson, W. C. Rhines, and H. P. Maruska, "Gallium nitride metal-semiconductor junction light emitting diode," *U.S. Patent 3819974*, filed Mar 12, 1973 - issued Jun 25,1974.

[83] H. Amano, M. Kito, K. Hiramatsu, and I. Akasaki, "P-type conduction in Mg-doped GaN treated with low-energy electron beam irradiation (LEEBI)," *Japanese Journal of Applied Physics Part 2 - Letters*, vol. 28, pp. L2112–L2114, Dec 1989.

[84] S. Nakamura, T. Mukai, and M. Senoh, "Candela-class high-brightness InGaN/AlGaN double-heterostructure blue-light-emitting diodes," *Applied Physics Letters*, vol. 64, pp. 1687–1689, Mar 28 1994.

[85] S. Nakamura, M. Senoh, N. Iwasa, and S. I. Nagahama, "High-brightness InGaN blue, green and yellow light-emitting diodes with quantum well structures," *Japanese Journal of Applied Physics Part 2 - Letters*, vol. 34, pp. L797–L799, Jul 1 1995.

[86] S. Nakamura, S. Pearton, and G. Fasol, "The Blue Laser Diode: The Complete Story," *Springer*, 2000.

[87] H. Morkoc, S. Strite, G. B. Gao, M. E. Lin, B. Sverdlov, and M. Burns, "Large-band-gap SiC, III-V nitride, and II-VI ZnSe-based semiconductor device technologies," *Journal of Applied Physics*, vol. 76, pp. 1363–1398, Aug 1st 1994.

[88] A. Tzalenchuk, S. Lara-Avila, A. Kalaboukhov, S. Paolillo, M. Syvajarvi, R. Yakimova, O. Kazakova, T. J. B. M. Janssen, V. Fal'ko, and S. Kubatkin, "Towards a quantum resistance standard based on epitaxial graphene," *Nature Nanotechnology*, vol. 5, no. 3, pp. 186–189, 2010.

[89] Y. Hu, M. Ruan, Z. Guo, R. Dong, J. Palmer, J. Hankinson, C. Berger, and W. A. de Heer, "Structured epitaxial graphene: growth and properties," *Journal of Physics D - Applied Physics*, vol. 45, no. 15, SI, 2012.

[90] M. Orlita, C. Faugeras, R. Grill, A. Wysmolek, W. Strupinski, C. Berger, W. A. de Heer, G. Martinez, and M. Potemski, "Carrier Scattering from Dynamical Magnetoconductivity in Quasineutral Epitaxial Graphene," *Physical Review Letters*, vol. 107, Nov 18 2011.

[91] M. Rubio-Roy, F. Zaman, Y. Hu, C. Berger, M. W. Moseley, J. D. Meindl, and W. A. de Heer, "Structured epitaxial graphene growth on SiC by selective graphitization using a patterned AlN cap," *Applied Physics Letters*, vol. 96, no. 8, 2010.

[92] S. Tongay, M. Lemaitre, J. Fridmann, A. F. Hebard, B. P. Gila, and B. R. Appleton, "Drawing graphene nanoribbons on SiC by ion implantation," *Applied Physics Letters*, vol. 100, no. 7, 2012.

[93] N. Piggins, E. Davis, and S. Bayliss, "Optical properties and spin densities of SiNx(-H) films," *Journal of Non-Crystalline Solids*, vol. 97-8, no. Part 2, pp. 1047–1050, 1987.

[94] W. Claassen, W. Valkenburg, F. Habraken, and Y. Tamminga, "Characterization of plasma silicon-nitride layers," *Journal of the Electrochemical Society*, vol. 130, no. 12, pp. 2419–2423, 1983.

[95] J. Bandet, B. Despax, and M. Caumont, "Nitrogen bonding environments and local order in hydrogenated amorphous silicon nitride films studied by Raman spectroscopy," *Journal of Applied Physics*, vol. 85, pp. 7899–7904, June 1 1999.

[96] *Average thicknesses obtained by ellipsometer match other thickness measurements, notably light absorption. To be published.*

[97] C. Faugeras, A. Nerriere, M. Potemski, A. Mahmood, E. Dujardin, C. Berger, and W. A. de Heer, "Few-layer graphene on SiC, pyrolitic graphite, and graphene: A Raman scattering study," *Applied Physics Letters*, vol. 92, no. 1, 2008.

[98] J. Roehrl, M. Hundhausen, K. V. Emtsev, T. Seyller, R. Graupner, and L. Ley, "Raman spectra of epitaxial graphene on SiC(0001)," *Applied Physics Letters*, vol. 92, no. 20, 2008.

[99] N. Sharma, D. Oh, H. Abernathy, M. Liu, P. N. First, and T. M. Orlando, "Signatures of epitaxial graphene grown on Si-terminated 6H-SiC (0001)," *Surface Science*, vol. 604, no. 2, pp. 84–88, 2010.

[100] J. K. Hite, M. E. Twigg, J. L. Tedesco, A. L. Friedman, R. L. Myers-Ward, C. R. Eddy, Jr., and D. K. Gaskill, "Epitaxial Graphene Nucleation on C-Face Silicon Carbide," *Nano Letters*, vol. 11, no. 3, pp. 1190–1194, 2011.

[101] A. Tiberj, N. Camara, P. Godignon, and J. Camassel, "Micro-Raman and micro-transmission imaging of epitaxial graphene grown on the Si and C faces of 6H-SiC," *Nanoscale Research Letters*, vol. 6, no. 478, 2011.

[102] J. Robertson, "Defect and inpurity states in silicon nitride," *Journal of Applied Physics*, vol. 54, no. 8, pp. 4490–4493, 1983.

[103] J. Robertson and M. Powell, "Gap states in silicon nitride," *Applied Physics Letters*, vol. 44, no. 4, pp. 415–417, 1984.

[104] W. Lau, S. Fonash, and J. Kanicki, "Stability of electrical properties of nitrogen-rich, silicon-rich, and stoichiometric silicon nitride films," *Journal of Applied Physics*, vol. 66, no. 6, pp. 2765–2767, 1989.

[105] W. Warren, J. Robertson, and J. Kanicki, "Si and N dangling bond creation in silicon nitride thin films," *Applied Physics Letters*, vol. 63, no. 19, pp. 2685–2687, 1993.

[106] D. Jousse, J. Kanicki, D. Krick, and P. Lenahan, "Electron spin resonance study of defects in plasma-enhanced chemical vapor-deposited silicon-nitride," *Applied Physics Letters*, vol. 52, no. 6, pp. 445–447, 1988.

[107] J. Palmer, "Pre-growth structures for high quality epitaxial graphene nanoelectronics grown on silicon carbide," *PhD Thesis, Georgia Institute of Technology, School of Physics*, December 2014.

[108] H. D. Batha and E. D. Whitney, "Kinetics and mechanism of the thermal decomposition of Si3N4," *Journal of the American Ceramic Society*, vol. 56, no. 7, pp. 365–369, 1973.

[109] A. Dogan, *The reliability of the silicon nitride dielectric in capaciative MEMS switches*. Master's thesis, Pennsylvania State University, School of Materials Science and Engineering, 2005.

[110] T. Shimada, T. Sugai, C. Fantini, M. Souza, L. Cancado, A. Jorio, M. Pimenta, R. Salto, A. Gruneis, G. Dresselhaus, M. Dresselhaus, Y. Ohno, T. Mizutani, and H. Shinohara, "Origin of the 2450 cm(-1) Raman bands in HOPG, single-wall and double-wall carbon nanotubes," *Carbon*, vol. 43, no. 5, pp. 1049–1054, 2005.

[111] C. Uslu, D. Lee, Y. Berta, B. Park, D. Poker, and L. Riester, "Enhanced surface hardness in nitrogen-implanted silicon carbide," *Nuclear Instruments and Methods in Physics Research B*, vol. 118, pp. 693–697, Sep 1996.

[112] S. Rodil, A. Ferrari, J. Robertson, and W. Milne, "Raman and infrared modes of hydrogenated amorphous carbon nitride," *Journal of Applied Physics*, vol. 89, pp. 5425–5430, May 15 2001.

[113] A. Ferrari, S. Rodil, and J. Robertson, "Interpretation of infrared and Raman spectra of amorphous carbon nitrides," *Physical Review B*, vol. 67, Apr 15 2003.

[114] J. Palmer, J. Kunc, Y. Hu, J. Hankinson, Z. Guo, C. Berger, and W. A. de Heer, "Controlled epitaxial graphene growth within removable amorphous carbon corrals," *Applied Physics Letters*, vol. 105, no. 2, 2014.

[115] S. Gautier, C. Sartel, S. Ould-Saad, J. Martin, A. Sirenko, and A. Ougazzaden, "GaN materials growth by MOVPE in a new-design reactor using DMHy and NH3," *Journal of Crystal Growth*, vol. 298, pp. 428–432, Jan 2007. 13th International Conference on Metal Organic Vapor Phase Epitaxy, Miyazaki, Japan, May 22-26, 2006.

[116] D. J. Rogers, F. H. Teherani, A. Ougazzaden, S. Gautier, L. Divay, A. Lusson, O. Durand, F. Wyczisk, G. Garry, T. Monteiro, M. R. Correira, M. Peres, A. Neves, D. McGrouther, J. N. Chapman, and M. Razeghi, "Use of ZnO thin films as sacrificial templates for metal organic vapor phase epitaxy and chemical lift-off of GaN," *Applied Physics Letters*, vol. 91, Aug 13 2007.

[117] D. Brown, "JEOL JBX-9300FS Electron Beam Lithography System Training," *Georgia Tech IEN (formerly MiRC) - www.nanolithography.gatech.edu/JEOL_JBX-9300FS_Training.pdf*, June 2009.

[118] O. Jani, I. Ferguson, C. Honsberg, and S. Kurtz, "Design and characterization of GaN/InGaN solar cells," *Applied Physics Letters*, vol. 91, Sep 24 2007.

[119] C. J. Neufeld, N. G. Toledo, S. C. Cruz, M. Iza, S. P. DenBaars, and U. K. Mishra, "High quantum efficiency InGaN/GaN solar cells with 2.95 eV band gap," *Applied Physics Letters*, vol. 93, Oct 6 2008.

[120] R. Dahal, B. Pantha, J. Li, J. Y. Lin, and H. X. Jiang, "InGaN/GaN multiple quantum well solar cells with long operating wavelengths," *Applied Physics Letters*, vol. 94, Feb 9 2009.

[121] R. Dahal, J. Li, K. Aryal, J. Y. Lin, and H. X. Jiang, "InGaN/GaN multiple quantum well concentrator solar cells," *Applied Physics Letters*, vol. 97, Aug 16 2010.

[122] E. Matioli, C. Neufeld, M. Iza, S. C. Cruz, A. A. Al-Heji, X. Chen, R. M. Farrell, S. Keller, S. DenBaars, U. Mishra, S. Nakamura, J. Speck, and C. Weisbuch, "High internal and external quantum efficiency InGaN/GaN solar cells," *Applied Physics Letters*, vol. 98, Jan 10 2011.

[123] X. Chen, K. D. Matthews, D. Hao, W. J. Schaff, and L. F. Eastman, "Growth, fabrication, and characterization of InGaN solar cells," *Physica Status Solidi A*, vol. 205, pp. 1103–1105, May 2008. 7th International Conference on Nitride Semiconductors (ICNS-7), Las Vegas, NV, SEP 16-21, 2007.

[124] R. M. Farrell, C. J. Neufeld, S. C. Cruz, J. R. Lang, M. Iza, S. Keller, S. Nakamura, S. P. DenBaars, U. K. Mishra, and J. S. Speck, "High quantum efficiency InGaN/GaN multiple quantum well solar cells with spectral response extending out to 520 nm," *Applied Physics Letters*, vol. 98, May 16 2011.

[125] M. Rao, D. Kim, and S. Mahajan, "Compositional dependence of phase separation in InGaN layers," *Applied Physics Letters*, vol. 85, pp. 1961–1963, Sep 13 2004.

[126] S. Pereira, M. Correia, E. Pereira, K. O'Donnell, C. Trager-Cowan, F. Sweeney, and E. Alves, "Compositional pulling effects in InxGa1-x/GaN layers: A combined depth-resolved cathodoluminescence and Rutherford backscattering/channeling study," *Physical Review B*, vol. 64, Nov 15 2001.

[127] D. Fuhrmann, C. Netzel, U. Rossow, A. Hangleiter, G. Ade, and P. Hinze, "Optimization scheme for the quantum efficiency of GaInN-based green-light-emitting diodes," *Applied Physics Letters*, vol. 88, Feb 13 2006.

[128] N. G. Young, R. M. Farrell, Y. L. Hu, Y. Terao, M. Iza, S. Keller, S. P. DenBaars, S. Nakamura, and J. S. Speck, "High performance thin quantum barrier InGaN/GaN solar cells on sapphire and bulk (0001) GaN substrates," *Applied Physics Letters*, vol. 103, Oct 21 2013.

[129] K. Pantzas, Y. El Gmili, J. Dickerson, S. Gautier, L. Largeau, O. Mauguin, G. Patriarche, S. Suresh, T. Moudakir, C. Bishop, A. Ahaitouf, T. Rivera, C. Tanguy, P. L. Voss, and A. Ougazzaden, "Semibulk InGaN: A novel approach for thick, single phase, epitaxial InGaN layers grown by MOVPE," *Journal of Crystal Growth*, vol. 370, pp. 57–62, May 1st 2013.

[130] Y. El Gmili, G. Orsal, K. Pantzas, T. Moudakir, S. Sundaram, G. Patriarche, J. Hester, A. Ahaitouf, J. P. Salvestrini, and A. Ougazzaden, "Multilayered InGaN/GaN structure vs. single InGaN layer for solar cell applications: A comparative study," *Acta Materialia*, vol. 61, pp. 6587–6596, Oct 2013.

[131] W. H. Goh, G. Patriarche, P. L. Bonanno, S. Gautier, T. Moudakir, M. Abid, G. Orsal, A. A. Sirenko, Z. H. Cai, A. Martinez, A. Ramdane, L. Le Gratiet, D. Troadec, A. Soltani, and A. Ougazzaden, "Structural and optical properties of nanodots, nanowires, and multi-quantum wells of III-nitride grown by MOVPE nano-selective area growth," *Journal of Crystal Growth*, vol. 315, pp. 160–163, Jan 15 2011. 15th

International Conference on Metalorganic Vapor Phase Epitaxy (ICMOVPE-XV), Incline Village, NV, May 23-28, 2010.

[132] T. Kuykendall, P. Ulrich, S. Aloni, and P. Yang, "Complete composition tunability of InGaN nanowires using a combinatorial approach," *Nature Materials*, vol. 6, pp. 951–956, Dec 2007.

[133] Y. Wang, K. Zang, S. Chua, M. S. Sander, S. Tripathy, and C. G. Fonstad, "High-density arrays of InGaN nanorings, nanodots, and nanoarrows fabricated by a template-assisted approach," *Journal of Physical Chemistry B*, vol. 110, pp. 11081–11087, Jun 15 2006.

[134] J. Song, B. Leung, Y. Zhang, and J. Han, "Growth, structural and optical properties of ternary InGaN nanorods prepared by selective-area metalorganic chemical vapor deposition," *Nanotechnology*, vol. 25, Jun 6 2014.

[135] W. H. Goh, J. Martin, S. Ould-Saad, S. Gautier, A. A. Sirenko, A. Martinez, L. Le Gratiet, A. Ramdane, N. Maloufi, and A. Ougazzaden, "Selective growth of GaN nanodots and nanostripes on 6H-SiC substrates by metal organic vapor phase epitaxy," in *Physica Status Solidi C* (Butte, R, ed.), Physica Status Solidi C-Current Topics in Solid State Physics, pp. S510–S513, 2009. International Workshop on Nitride Semiconductors, Montreux, Switzerland, Oct 06-10, 2008.

[136] D. Zubia, S. Zaidi, S. Brueck, and S. Hersee, "Nanoheteroepitaxial growth of GaN on Si by organometallic vapor phase epitaxy," *Applied Physics Letters*, vol. 76, pp. 858–860, Feb 14 2000.

[137] K. Pantzas, G. Patriarche, D. Troadec, S. Gautier, T. Moudakir, S. Suresh, L. Largeau, O. Mauguin, P. L. Voss, and A. Ougazzaden, "Nanometer-scale, quantitative composition mappings of InGaN layers from a combination of scanning transmission electron microscopy and energy dispersive x-ray spectroscopy," *Nanotechnology*, vol. 23, Nov 16 2012.

[138] Z. Liliental-Weber, K. M. Yu, M. Hawkridge, S. Bedair, A. E. Berman, A. Emara, J. Domagala, and J. Bak-Misiuk, "Spontaneous stratification of InGaN layers and its influence on optical properties," in *Physica Status Solidi C-Current Topics in Solid State Physics* (Butte, R, ed.), vol. 6, pp. S433–S436, 2009. International Workshop on Nitride Semiconductors, Montreux, Switzerland, Oct 06-10, 2008.

[139] H. Wang, D. S. Jiang, U. Jahn, J. J. Zhu, D. G. Zhao, Z. S. Liu, S. M. Zhang, and H. Yang, "Cathodoluminescence study on in composition inhomogeneity of thick InGaN layer," *Thin Solid Films*, vol. 518, pp. 5028–5031, Jun 30 2010.

[140] K. Pantzas, G. Patriarche, G. Orsal, S. Gautier, T. Moudakir, M. Abid, V. Gorge, Z. Djebbour, P. L. Voss, and A. Ougazzaden, "Investigation of a relaxation mechanism specific to InGaN for improved MOVPE growth of nitride solar cell materials," *Physica Status Solidi A*, vol. 209, pp. 25–28, Jan 2012.

[141] M. Schuster, P. Gervais, B. Jobst, W. Hosler, R. Averbeck, H. Riechert, A. Iberl, and R. Stommer, "Determination of the chemical composition of distorted InGaN GaN heterostructures from x-ray diffraction data," *Journal of Physics D - Applied Physics*, vol. 32, pp. A56–A60, May 21 1999. 4th Biennial Conference on High Resolution X-ray Diffraction and Topography (XTOP 98), Univ. Durham, Durham, England, Sep 09-11, 1998.

[142] Y. El Gmili, G. Orsal, K. Pantzas, A. Ahaitouf, T. Moudakir, S. Gautier, G. Patriarche, D. Troadec, J. P. Salvestrini, and A. Ougazzaden, "Characteristics of the surface microstructures in thick InGaN layers on GaN," *Optical Materials Express*, vol. 3, pp. 1111–1118, Aug 1 2013.

[143] Y. Dong, B. Tian, T. J. Kempa, and C. M. Lieber, "Coaxial Group III-Nitride Nanowire Photovoltaics," *Nano Letters*, vol. 9, pp. 2183–2187, May 2009.

[144] L. Redaelli, A. Mukhtarova, S. Valdueza-Felip, A. Ajay, C. Bougerol, C. Himwas, J. Faure-Vincent, C. Durand, J. Eymery, and E. Monroy, "Effect of the quantum well thickness on the performance of InGaN photovoltaic cells," *Applied Physics Letters*, vol. 105, Sep 29 2014.

[145] I. Gherasoiu, K. M. Yu, L. A. Reichertz, V. M. Kao, M. Hawkridge, J. W. Ager, and W. Walukiewicz, "High quality InxGa1-xN thin films with x > 0.2 grown on silicon," *Physica Status Solidi B*, vol. 247, pp. 1747–1749, Jul 2010. E-MRS Fall Meeting on Wide Band Gap II-VI and III-V Semiconductors, Warsaw, Poland, Sep 14-18, 2009.

[146] A. G. Bhuiyan, A. Mihara, T. Esaki, K. Sugita, A. Hashimoto, A. Yamamoto, N. Watanabe, H. Yokoyama, and N. Shigekawa, "MOVPE growth of InGaN on Si(111) substrates with an intermediate range of In content," in *Physica Status Solidi C* (Parbrook, PJ and Martin, RW and Halsall, MP, ed.), vol. 9 of *Physica Status Solidi C-Current Topics in Solid State Physics*, pp. 670–672, AIXTRON; AkzoNobel; LG Elect; OSRAM Opto Semicond; CREE; LAYTEC In-situ Sensors; Philips Lumileds; Veeco; Glengoyne, 2012. 9th International Conference on Nitride Semiconductors (ICNS), Glasgow, Scotland, Jul 10-15, 2011.

[147] A. Yamamoto, A. Mihara, Y. Zheng, and N. Shigekawa, "A Comparative Study on Metalorganic Vapor Phase Epitaxial InGaN with Intermediate In Compositions Grown on GaN/Sapphire Template and AlN/Si(111) Substrate," *Japanese Journal of Applied Physics*, vol. 52, AUG 2013.

[148] J.-W. Ho, R. J. Tan, M. Heuken, A. A. Tay, and S.-J. Chua, "Growth of ingan nanopyramid arrays on si for potential photovoltaic applications," *Journal of Crystal Growth*, no. 0, pp. –, 2015.

[149] S. Luryi and E. Suhir, "New approach to the high quality epitaxial growth of lattice-mismatched materials," *Applied Physics Letters*, vol. 49, pp. 140–142, Jul 21 1986.

[150] S. Albert, A. Bengoechea-Encabo, M. A. Sanchez-Garcia, X. Kong, A. Trampert, and E. Calleja, "Selective area growth of In(Ga)N/GaN nanocolumns by molecular beam epitaxy on GaN-buffered Si(111): from ultraviolet to infrared emission," *Nanotechnology*, vol. 24, May 3 2013.

[151] V. Jindal, N. Tripathi, M. Tungare, O. Paschos, P. Haldar, and F. Shahedipour-Sandvik, "Selective area heteroepitaxy of low dimensional a-plane and c-plane InGaN nanostructures using pulsed MOCVD," in *Physica Status Solidi C* (Palacios, T and Jena, D, ed.), vol. 5, pp. 1709–1711, 2008. 7th International Conference on Nitride Semiconductors (ICNS-7), Las Vegas, NV, Sep 16-21, 2007.

[152] D. J. Rogers, F. H. Teherani, T. Moudakir, S. Gautier, F. Jomard, M. Molinari, M. Troyon, D. McGrouther, J. N. Chapman, M. Razeghi, and A. Ougazzaden, "Microstructural compositional, and optical characterization of GaN grown by metal organic vapor phase epitaxy on ZnO epilayers," *Journal of Vacuum Science & Technology B*, vol. 27, pp. 1655–1657, May 2009. 1st International Conference on Nanomanufacturing/4th International Conference on Technological Advances of Thin Films and Surface Coatings, Singapore, Singapore, JUL 13-17, 2008.

[153] D. J. Rogers, "Accelerating adoption of GaN substrates for LED manufacture," *Compound Semiconductor Magazine*, June 2014.

[154] J. Nause and B. Nemeth *The 3rd International Workshop on ZnO and Related Materials, Sendai, Japan*, 2004.

[155] N. Li, E.-H. Park, Y. Huang, S. Wang, A. Valencia, B. Nemeth, J. Nause, and I. Ferguson, "Growth of GaN on ZnO for solid state lighting applications," in *Sixth International Conference on Solid State Lighting* (Ferguson, IT and Narendran, N and Taguchi, T and Ashdown, IE, ed.), vol. 6337 of *Proceedings of the Society of Photo-Optical Instrumentation Engineers (SPIE)*, p. Z3370, SPIE, 2006. 6th International Conference on Solid State Lighting, San Diego, CA, Aug 14-17, 2006.

[156] L. Romano, B. Krusor, and R. Molnar, "Structure of GaN films grown by hydride vapor phase epitaxy," *Applied Physics Letters*, vol. 71, pp. 2283–2285, Oct 20 1997.

[157] A. Strittmatter, A. Krost, V. Turck, M. Strassburg, D. Bimberg, J. Blasing, T. Hempel, J. Christen, B. Neubauer, D. Gerthsen, T. Christmann, and B. Meyer, "LP-MOCVD growth of GaN on silicon substrates - comparison between AlAs and ZnO nucleation layers," *Materials Science and Engineering B*, vol. 59, pp. 29–32, May 6 1999.

[158] A. Ougazzaden, D. J. Rogers, F. H. Teherani, T. Moudakir, S. Gautier, T. Aggerstam, S. O. Saad, J. Martin, Z. Djebbour, O. Durand, G. Garry, A. Lusson, D. McGrouther, and J. N. Chapman, "Growth of GaN by metal organic vapor phase epitaxy on ZnO-buffered c-sapphire substrates," *Journal of Crystal Growth*, vol. 310, pp. 944–947, Mar 1st 2008. Symposium on Substrates of Wide Bandgap Materials held at the 2007 E-MRS Conference, Strasbourg, France, May 29-30, 2007.

[159] G. Jo, M. Choe, C.-Y. Cho, J. H. Kim, W. Park, S. Lee, W.-K. Hong, T.-W. Kim, S.-J. Park, B. H. Hong, Y. H. Kahng, and T. Lee, "Large-scale patterned multi-layer graphene films as transparent conducting electrodes for GaN light-emitting diodes," *Nanotechnology*, vol. 21, Apr 30 2010.

[160] K. Chung, C.-H. Lee, and G.-C. Yi, "Transferable GaN Layers Grown on ZnO-Coated Graphene Layers for Optoelectronic Devices," *Science*, vol. 330, pp. 655–657, Oct 29 2010.

[161] D.-W. Jeon, W. M. Choi, H.-J. Shin, S.-M. Yoon, J.-Y. Choi, L.-W. Jang, and I.-H. Lee, "Nanopillar ingan/gan light emitting diodes integrated with homogeneous multilayer graphene electrodes," *Journal of Materials Chemistry*, vol. 21, pp. 17688–17692, 2011.

[162] S. Tongay, M. Lemaitre, T. Schumann, K. Berke, B. R. Appleton, B. Gila, and A. F. Hebard, "Graphene/gan schottky diodes: Stability at elevated temperatures," *Applied Physics Letters*, vol. 99, no. 10, pp. –, 2011.

[163] R. Decker, Y. Wang, V. W. Brar, W. Regan, H.-Z. Tsai, Q. Wu, W. Gannett, A. Zettl, and M. F. Crommie, "Local Electronic Properties of Graphene on a BN Substrate via Scanning Tunneling Microscopy," *Nano Letters*, vol. 11, pp. 2291–2295, Jun 2011.

[164] B.-J. Kim, C. Lee, Y. Jung, K. H. Baik, M. A. Mastro, J. K. Hite, C. R. Eddy, Jr., and J. Kim, "Large-area transparent conductive few-layer graphene electrode in GaN-based ultra-violet light-emitting diodes," *Applied Physics Letters*, vol. 99, Oct 3 2011.

[165] J. Kang, Z. Li, H. Li, Z. Liu, X. Li, X. Yi, P. Ma, H. Zhu, and G. Wang, "Pyramid array ingan/gan core–shell light emitting diodes with homogeneous multilayer graphene electrodes," *Applied Physics Express*, vol. 6, no. 7, p. 072102, 2013.

[166] J. Kim, C. Bayram, H. Park, C.-W. Cheng, C. Dimitrakopoulos, J. A. Ott, K. B. Reuter, S. W. Bedell, and D. K. Sadana, "Principle of direct van der Waals epitaxy of single-crystalline films on epitaxial graphene," *Nature Communications*, vol. 5, 09 2014.

[167] C. Chatillon, P. Rocabois, and C. Bernard, "High-temperature analysis of the thermal degradation of silicon-based materials. I: Binary Si-O, Si-C, and Si-N compounds," *High Temperatures - High Pressures*, vol. 31, no. 4, pp. 413–432, 1999.

[168] J. Hass, R. Feng, T. Li, X. Li, Z. Zong, W. A. de Heer, P. N. First, E. H. Conrad, C. A. Jeffrey, and C. Berger, "Highly ordered graphene for two dimensional electronics," *Applied Physics Letters*, vol. 89, Oct 2 2006.

[169] M. E. Coltrin and C. C. Mitchell, "Mass transport and kinetic limitations in MOCVD selective-area growth," *Journal of Crystal Growth*, vol. 254, pp. 35–45, 6 2003.

[170] M. Krawczyk, L. Zommer, A. Kosinski, J. Sobczak, and A. Jablonski, "Measured electron IMFPs for SiC," *Surface and Interface Analysis*, vol. 38, pp. 644–647, Sep 2006.

[171] P. Cadman, S. Evans, J. Scott, and J. Thomas, "Determination of relative electron inelastic mean free paths (escape depths) and photoionisation cross-sections by x-ray photoelectron-spectroscopy," *Journal of the Chemical Society - Faraday Transactions II*, vol. 71, pp. 1777–1784, 1975.

[172] K. Miyoshi and D. H. Buckley, "Surface Chemistry and Wear Behavior of Single-Crystal Silicon Carbide Sliding Against Iron at Temperatures to 1500C in Vacuum," *NASA Technical Paper*, February 1982.

VITA

by Catherine Ruiz (mother), Philippe Puybaret (father) and Florent Puybaret (brother)

Born in Bayonne, Euskal Herri, France, in March 1986, Renaud started his life by the ocean in Biarritz where he happily grew up with his family and friends. He was a nature-loving kid, and did his first of many travels to USA at 5 years old in Florida. Traveling each summer became a family tradition, whether with car and hotels (Scotland, Canada and Maine, California, Croatia), or adventurous backpacking (Thailand, Ecuador, Madagascar, Sulawesi). He even first set foot in Atlanta, GA, USA, when he was 15, 10 years before his coming to Georgia Tech. At age 10, he was eating for the first time at the adults table while the Windels family (very close friends to our family) was invited for diner, among which Pascal is a satellite engineer at EADS Astrium. Answering to Renaud's inquiry, Pascal described his profession to him for the first time: Renaud then opened large eyes and swore "I want to do like Pascal". Since then he has always dreamed about satellites and how the universe was defined, a sparkling fascination for space which quickly spread over science and technology in general. He has always been considerate of his loved-ones, curious about everything, and of course a very bright and hardworking pupil and student, who's always made his family very proud. Renaud has also always been a very structured and rigorous young man: he is persevering, passionate about science, and uncompromising when it comes whether to the quality of his work or his performance in sports competitions. He always aspired to develop, discover and go beyond what he was taught. Today, at the crossroad of a new life, he's a good and responsible man, so may the world be his oyster.